An Efficacious and Safe Multichannel Neurostimulator Powered by an Ultrasonic Wireless Link

Pedro Gaizka Zufiria Gerbolés

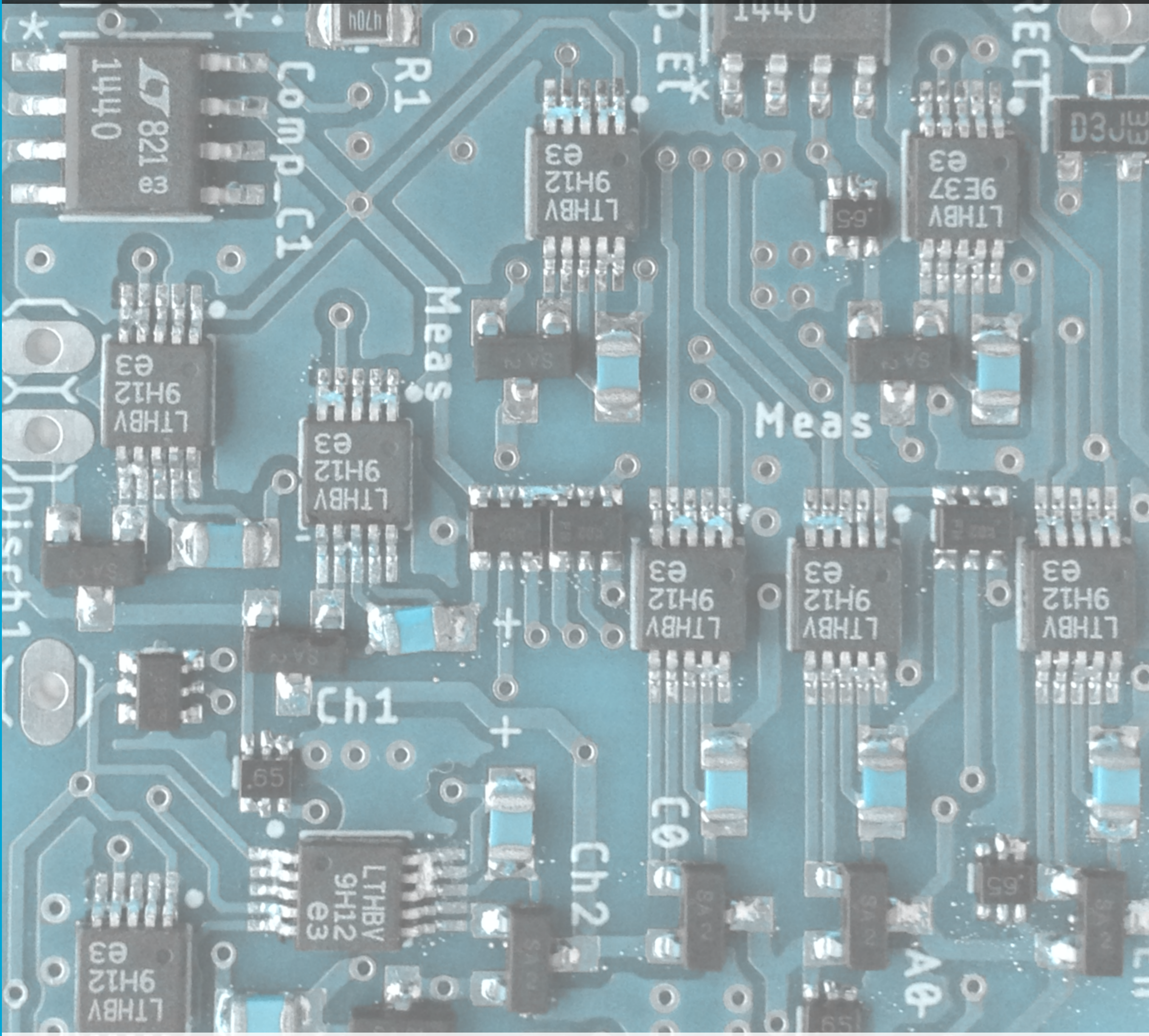

TU Delft
Delft
University of
Technology

An Efficacious and Safe Multichannel Neurostimulator Powered by an Ultrasonic Wireless Link

MSc Thesis

by

Pedro G. Zufiria Gerbolés

in partial fulfillment of the requirements for the degree of

Master of Science
in **Electrical Engineering**

at Delft University of Technology,
to be defended publicly on April 27, 2020 at 14:00.

Student number:	4747682	
Project duration:	September, 2018 – April, 2020	
Thesis supervisors:	Dr. V. Giagka,	TU Delft, Assistant Professor
	Prof. dr. ir. W.A. Serdijn,	TU Delft, Professor, Chairman
Thesis committee:	Dr. ir. C.J.M. Verhoeven,	TU Delft, Associate Professor

This thesis is confidential and cannot be made public until April, 2022.

Abstract

Neurostimulation is a common medical treatment modality used to treat neurological disorders. It applies electrical pulses to revert and prevent undesired neural behavior or to create desired neural behavior. The required specificity of said stimulation treatments is oftentimes achieved by implanting the neurostimulator close to the target area. Implantation of active medical device poses a series of challenges and requirements in size and power consumption. Wireless power transfer (WPT) technologies have been used to reduce the size or eliminate the use of batteries, which are the main limiting component in terms of size and longevity of the implants. In conventional WPT systems, the energy must be focused from an external transmitter to a receiver in the implanted neurostimulator. This one-to-one link cannot be used in some applications in which a network of neurostimulators is required to deliver treatment in multiple locations distant from each other. This is the case for some chronic headache treatments in which both the supraorbital and occipital nerves must be stimulated.

This thesis proposes a new system level topology for a neurostimulator network for the treatment of chronic headaches, in which all implants are powered through a single WPT link. It was theorized that the bone tissue in the skull can be used as an acoustic conductor for ultrasonic waves, similarly to bone-anchored hearing aid systems that already use bone conduction to conduct acoustic waves in the audible range. Finite element simulations showed that the skull can conduct ultrasonic energy in two frequency bands, which are 0.1-0.6 MHz and 1-2 MHz. A 2 MHz operating frequency was chosen for safety reasons, since the 1-2 MHz band does not leak unwanted energy into neighbouring soft tissues like the brain. At this frequency, the WPT link undergoes an attenuation of about 20 dB.

Each individual neurostimulator employs the ultra high frequency (UHF) stimulation technique to improve in power efficiency. Both the UHF stimulation and ultrasonic wireless power transfer work in the MHz frequency range, so the ultrasound signal can be “directly” used for the electrical stimulation of the tissue by means of a simple ultrasound transducer and some power conditioning. Previous designs using this concept are not easily scalable and cannot perform charge balancing to ensure safe stimulation of tissue. In addition, the use of a WPT powering method cannot guarantee a stable and uniform supply for the implanted neurostimulator. As a result, there is a need for a multichannel system that can deliver UHF stimulation pulses in a safe manner, while ensuring efficacy of the stimulation regardless of the power levels received through the WPT link.

This thesis proposes a novel output stage for implantable neurostimulators that ensures the efficacy and safety of the stimulation. Since the efficacy is directly related to the total charge delivered to the tissue, a novel charge metering circuitry is designed to control said amount of charge. Safety is obtained by minimizing the residual voltage after a stimulation cycle, which can otherwise damage the tissue and the electrodes. This is done by means of a novel charge balancing scheme that monitors the voltage across the electrodes and stops the stimulation when it crosses 0 V. Circuit simulations successfully validate the design. The proposed neurostimulator was also implemented on a PCB board and tested. The charge delivery resolution of the charge metering circuit is 510 pC. A residual voltage of 0.5 mV to 29.5 mV was achieved with the charge balancing circuitry, using an electrical model of the tissue. *In vitro* measurements in a phosphate buffered saline solution show a 80 mV residual voltage. Hence, this work successfully presents a new neurostimulator output stage topology that ensures efficacy and safety in the presence of an unreliable WPT link, while being compatible with multichannel operation and an IC implementation.

Acknowledgment

I would like to thank everyone who helped me during the course of this project, and everyone else who supported me unconditionally during this wonderful experience in Delft.

First, I would like to thank Wouter for his endless support and availability. Thank you for seeing potential in me, for supporting and challenging my ideas, and of course, for your warm and welcoming attitude towards me inside and outside of the office.

A special thank you to Vasso, for always being so passionate and driven towards my project. Thank you for the great discussions that we've had; you really made me feel like an expert in the field. And thank you for always brightening the day with your contagious smile.

Thank you to everyone in the Bioelectronics group for all the wonderful moments, drinks, movies, and zooms that we've spent together. I will miss this wonderful working environment that we have all created. Truly unforgettable.

A warm thank you to my office mates, Alberto and Andra, for the laughs, the roasts, the coffee breaks, but also for all the help with my project and your infinite words of encouragement.

I would like to thank Rui, for showing her enthusiasm towards my project since day one, and for collaborating with me towards the publication of our paper. It has been a pleasure working with you.

Thank you to Nasim for your help with the in vitro experiments, and to Konstantina for your help with the report.

Thank you to all my friends in Delft. A special mention to my classmates, my IP besties, my sisters from Outsite, and of course my Spanish friends who adopted me into their home every single Sunday.

Also a gigantic thank you to my friends in Madrid. Fede, Lourdes and all the others, I know you will always be there for me, just like you have for the past twenty one years of my life.

And last, but definitely not least, I would like to thank my entire family for their limitless love and support during all these years that I have been abroad. A thank you to Blanca, Luis, Nicolás, and Marta, my siblings, who always welcome me as if I had never gone abroad. Finally, as we say in Spain, a thousand millions of thank yous to my parents, for always showing interest in my studies and my passions. Gracias.

Contents

List of Figures

List of Tables

1

Introduction

Medical implants for neural stimulation, also know as neurostimulators, have been used for the past decades in the form of familiar devices like pacemakers, cochlear implants, deep brain stimulators, etc. There are many more neurological disorders that can be treated by means of neural stimulation and, as a result, the development of neurostimulators has grown significantly until the present. Nowadays, active implantable biomedical microsystems (AIBMs), which employ electrical stimulation as a means of treatment, are being used not only for heart arrhythmia, hearing loss, or Parkinson's disease but also for bladder incontinence, chronic pain, vision loss, etc [1]. The advantages of these "electroceuticals" as compared to pharmaceuticals are the reduction in treatment cost, a higher specificity, and the reduction of side effects. In other words, if the disease is originated in a neurological malfunction, the most straightforward solution should be to stimulate or suppress the affected area directly [2].

The implantability of said neurostimulators is crucial to ensure specificity of treatment. Thus, the size and lifetime of the AIBMs become two of the most critical parameters to consider while designing. There are many approaches to optimize the size, lifetime and implantability of a neurostimulator, but the design of such a neurostimulator will depend on the application and the stimulation requirements. In order to correctly interpret said requirements, it is crucial to understand the underlying mechanism behind the electrical stimulation of tissue.

1.1. Background

1.1.1. Electrical Stimulation

Electrical stimulation takes advantage of the properties of excitable cells, which are able to conduct electric impulses. These cells are categorized into two groups: muscle cells and nerve cells [3]. In this thesis project, the main focus of study relates to the excitation of nerve cells.

1.1.1.1. Bioelectric Mechanisms of Nerve Cells

Nerve cells are able to transmit an electric pulse along their axons. The impulse can then be transfer to an adjacent nerve cell through the synapse. The working principle of the electrical conduction along axons is mostly related to changes in the voltage across the membrane (V_m) [3]. This voltage is usually at a constant resting voltage level (V_R). Different stimuli can change said voltage to excite the cell (by reducing the membrane voltage in magnitude, depolarization) or inhibit the cell (by increasing the membrane voltage in magnitude, hyperpolarization). In the case of excitation, the membrane voltage is reduced in magnitude and, when it crosses a certain threshold (V_{th}), an Action Potential (AP) fires. This AP is just due to an opening and closing of different ion channels located in the cell membrane. The resulting ion flow changes the membrane voltage V_m, and this mechanism allows the adjacent regions of the membrane to surpass their V_{th}. Thus, the AP propagates along the axon.

1.1.1.2. Effect of External Stimuli on Cell Activation

The membrane voltage can be varied using external stimuli of different natures. Light and ultrasound have been shown to elicit AP in certain quantities; but electrical stimulation is the most common method to stimulate or inhibit cells. The main reason to use electrical stimulation is that the applied charge during stimulation can be easily controlled, and the membrane voltage can be modified with high precision. In addition, this modality also requires significantly less energy to elicit the activation. For example, if electrical stimulation is compared to ultrasonic stimulation, the power requirements might be around three orders of magnitude smaller [4].

Electrical stimulation generates electrical fields in the cell vicinity, which in turn, can depolarize or hyperpolarize the cell membrane. The intensity of such an electric field can be achieved by means of controlling the charge accumulated at the stimulation electrodes. The role of a neurostimulator is, for the most part, to generate the desired voltage or current to deliver the required amount of charge to the excitable neural cells. The effectiveness of the stimulus is determined by the strength-duration curve shown in Figure 1.1, where I_{rh} is the rheobase current, which indicates the smallest current required for activation assuming that the current is delivered for and infinitely long period of time. It is sometimes referred as the sensitivity of the cell. t_c is the chronaxy, which corresponds to the time required to excite at intensity $2I_{rh}$ [3].

Alternatively, the effectiveness of stimulation can be associated to the charge density (charge over a specific period of time) delivered to the tissue. This relation is explained in the right plot in Figure 1.1.

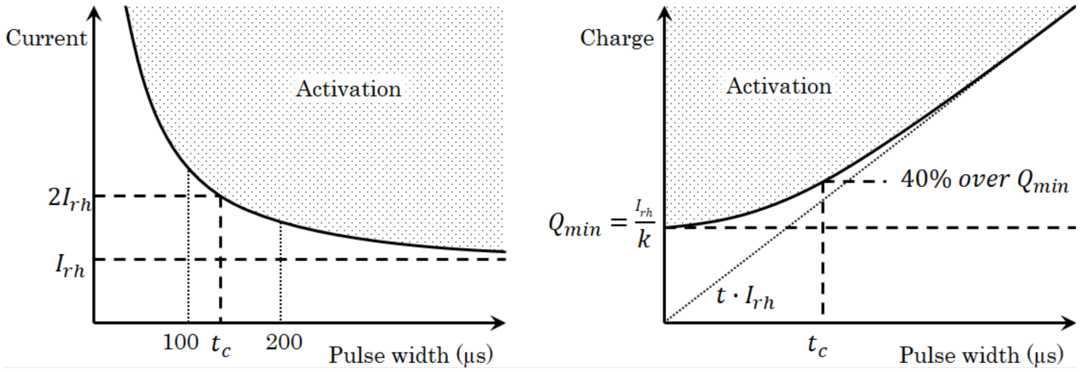

a) b)

Figure 1.1: Cell activation curves. **a)** Strength-duration curve. **b** Charge-duration curve.

1.1.2. Implants

Devices that generate the required current or voltage pulses for electrical stimulation are referred as neurostimulators. Over the past decades, neurostimulators have been designed to treat various diseases: pacemakers for heart arrhythmias, cochlear implants for hearing diseases, spinal cord stimulators for chronic pain, deep brain stimulators for tremors, headache diseases, Parkinson's disease, epilepsy, or dystonia, vagus nerve stimulation for epilepsy, migraine or depression, retinal implants for vision restorage, sacral nerve stimulators for urinary incontinence, etc. [5]. Neurostimulators can be adjusted by a doctor or technician to deliver different treatments to the patient. The complexity of the therapy is limited by the topology of the stimulator and its capabilities (number of channels, wave form, etc). The different types of electrical stimulation and their characteristics will be explained in more detail in Chapter 2.

Based on the application, neurostimulators can be placed in different locations, depending on the required level of invasiveness to reach the target. According to this categorization, neurostimulators can be wearables if they are placed on the surface of the skin, swallables if they are ingested by the patient, or implants if they are surgically inserted somewhere inside the body.

The development of integrated circuits over the past decades has been crucial to the development of implants. These circuits can be monolithically fabricated alongside other micromechanical structures, like membranes or channels, to increase the functionalities of the devices. These are know as microelectormechanical systems (MEMS). The miniaturization of these systems allows their implantation inside the body, without the need for complex or invasive surgical procedures. The newest generation of neurostimulators has been miniaturized to the extent that a new category of implants has emerged, where they can be injected inside the body. This category is referred as injectables [5].

Traditionally, implants have been powered by batteries due to their high reliability. Regardless of their reliability, batteries are very bulky and they end up taking the majority of the implant's available size. As a result, implant miniaturization requires alternative powering techniques. Wireless power transfer proves to be one of the most popular solutions for the new generation of implantable neurostimulators.

1.2. Problem Statement

Modern AIBMs must be small in size and durable over long periods of implantation lifetime. Integrated circuits have allowed for the miniaturization of said devices, along with wireless powering techniques that permit the removal of bulky batteries. Nevertheless, there is a need for a system that guarantees efficacious activation of the tissue, regardless of the reliability of the wireless power link. Furthermore, with standard stimulation patterns, there is residual charge remaining in the electrode tissue interface. This residual charge results in reduction-oxidation reactions, which can damage the tissue and corrode the electrodes. Consequently, there is a need to guarantee stimulation safety by minimizing the amount of residual charge after each stimulation cycle. This ensuring of stimulation safety is what is traditionally referred to as charge balancing. Along with efficacy and safety, the ideal system should be scalable and able to operate in a multichannel configuration.

1.3. Goal and Approach

The goal of this project is to develop a neurostimulation system for the treatment of chronic headache diseases. The proposed design will utilize a wireless ultrasonic power link through bone to deliver energy to each of the neurostimulation implants, thus eliminating the need of a battery and ensuring miniaturization. That energy will be "directly" delivered to the tissue for stimulation by means of a simple ultrasonic transducer and rectification of the AC incoming signal. Finally the efficacy and safety of stimulation will be guaranteed with a novel charge metering and charge balancing topology. The proposed topology and stimulation scheme will guarantee the scalability of the system, as well as its capability to operate in a multichannel configuration. In addition to this, the proposed topology will be easy to integrate into an integrated circuit (IC) and it will also be CMOS compatible. To achieve the design objectives, each of the system requirements will be addressed in an orthogonal manner one by one. Nevertheless, the preexisting circuitry will be taken into consideration in each step of the design.

1.4. Outline

This thesis report is structured as follows. First, the state of the art regarding wireless power transfer, charge metering and charge balancing will be discussed in Chapter 2. Following the state of the art, the proposed overall system will be presented in Chapter 3, while the design of the neurostimulator and its output stage will presented in Chapter 4. Initial simulations, along with the measurements of a prototype circuit and discussion on the results are explained in Chapter 5 followed by the conclusion in Chapter 6. Chapter 6 also summarizes the contributions of this work and recommendations for future work.

2

Literature Review

2.1. Application

The application to be targeted for this project is the treatment of chronic headache disorders. Conventionally, many of these headache disorders are treated by means of chemical pharmaceuticals, but electrical stimulation has also been proven effective. The limitations of existing electrical neurostimulators for headache disorders are explained below.

2.1.1. Electrical Stimulation for Headache Disorders

Electrical neural simulators have been use for a wide range of applications for the past decades. One possible application for them is the treatment of headache disorders. Headache disorders are classified into two different types: episodic and chronic [6]. Episodic headaches occur less than 15 days a month and for a periods of time shorter than 3 months. On the other hand, chronic headaches affect the patient more than 15 days per month for periods of time longer than 3 months [6]. Depending on the specific disease and its characteristics, different nerve tissues can be stimulated for their treatment. The most commonly stimulated areas are: the posterior hypothalamus (HT) region, the ventral tegmental area (VTA), the vagus nerve (VN), the sphenopalatine ganglion (SPG), the lesser and greater occipital nerves (ON), the supraorbital nerve (SN), and the cortex [6].

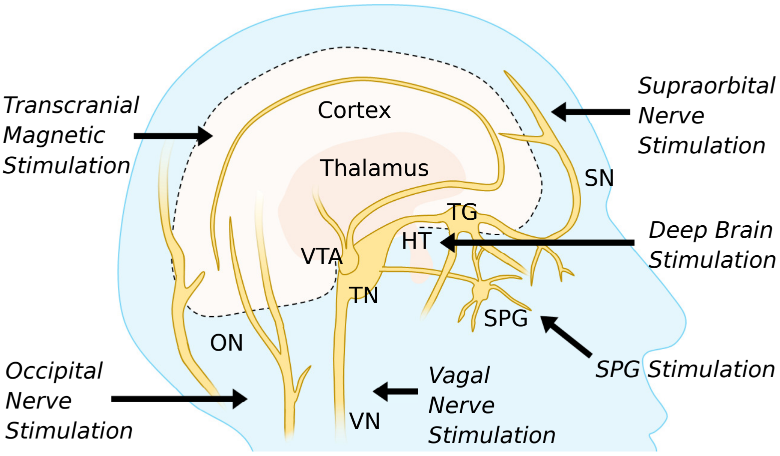

Figure 2.1: Different stimulation sites and stimulation types for headache disease treatments. *Occipital Nerve Stimulation* targets the lesser and greater Occipital Nerves (ON) in the back area of the head. *Transcranial Magnetic Stimulation* targets the Occipital Nerves as well as the Cortex. *Vagal Nerve Stimulation* targets the Vagus Nerve (VN). *SPG* Stimulation targets the Sphenopalatine Ganglion (SPG). *Deep Brain Stimulation* targets the posterior Hypothalamus (HT) region, the Ventral Tegmental Area (VTA) close to the Trigeminal Nerve (TN), which connects to the Trigenimal Ganglion (TG).

Electrical stimulation has been proven efficient when treating these types of chronic headache diseases. Multiple devices are already available in the market and small controlled trial studies have been performed to validate their efficacy [6]. These devices can be divided into non-invasive and invasive categories. The level of invasiveness of the devices is related to the location of the nerves to be stimulated, as different headache disorders may require different nerves to be stimulated.

2.1.1.1. Non-invasive Procedures

The most common non-invasive stimulation procedures include supraorbital nerve stimulation, vagus nerve stimulation, and single-pulse transcranial magnetic stimulation [6]. All of these are achieved via devices that are put in close proximity to the areas to be targeted. This implies that no implantation of any kind is required, thus giving them the non-invasive classification.

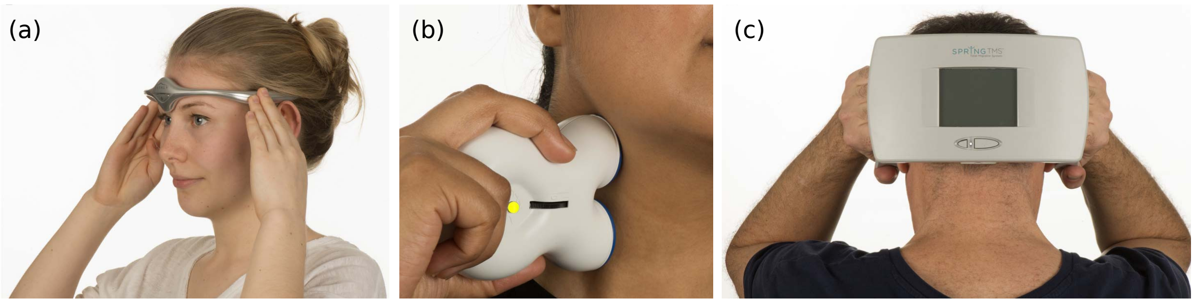

Figure 2.2: Different non-invasive stimulation devices. **a)** *Cefaly* device for supraorbital stimulation to suppress episodic migraines. **b)** *gammaCore* device for vagus nerve stimulation, used to prevent cluster headache attacks. **c)** *SpringTMS* device for transcranial magnetic stimulation of the occipital region for the prevention of migraine attacks. Modified images taken from [6]

The already available devices (like *Cefaly*) for supraorbital nerve stimulation, take advantage of the location of the target nerve to deliver the stimulus transcutaneously [6]. Figure 2.1 shows the location of this nerves right over the skull in the frontal area of the head. This means that, by placing the device over the skin on that area, one can get as close as a few millimeters to the nerves (Figure 2.2.a).

The devices used for vagus nerve stimulation (like *gammaCore*, Figure 2.2.b) are similar in principle to the ones for occipital nerve stimulation. The details associated with this type of stimulation are not very relevant to the target of our proposed system, so they won't be further explored here. It is only important to note that they also use electrical stimulation to deliver the treatment.

The previous two examples made use of electrical stimulation to target the desired nerves. In the case of transcranial magnetic stimulation, existing devices (like *SpringTMS*) deliver a magnetic pulse that induces currents in the cortex in the occipital regions of the head [6]. In this case the device is also held in place by the patient, as seen in Figure 2.2.c.

All the above-mentioned devices present some advantages and disadvantages. The main advantage of these devices is that they do not require implantation, so they are not invasive. The size of the devices and the energy storage do not present a problem in the design. They have to be "wearable" or "holdable" by the patient; but given the current technological advances, creating such a device does not impose a challenge.

Still, there are a few disadvantages associated with the devices presented above. The first disadvantage is that they require the collaboration of the patient to put the device over their head and hold it in place for the duration of the session, see Figure 2.2. In the case of the *Cefaly* device, the duration is of 20 min; but it can be as long as 2 h for other devices like the *SpringTMS* [6]. These long sessions create some additional inconveniences. A better device should be fixed in place, so that the patient's input is not required. The second disadvantage is that these devices do not allow for recording or prediction of migraine (headache) attacks, which means that the only way to know when to stimulate is by means of waiting for an attack to happen. In an ideal scenario, the stimulation device should be able to predict this event and stimulate accordingly. Finally, the last disadvantage is that the stimulus cannot be delivered precisely to the nerves. The level of precision is low. This might compromise the power consumption of the system as a whole, as more power has to be delivered to ensure enough intensity at the exact location of the nerves. Additionally, side effects might affect the nearby tissue close to the supraorbital nerves, vagus nerve, or occipital region.

2.1.1.2. Invasive Procedures

Invasive devices are defined as those systems that require some or all of their parts to be implanted somewhere inside the patient. Different targets require different levels of invasiveness for their implantation procedure.

Occipital nerve stimulation is the least invasive procedure as it does not require any destructive surgical procedure [6]. In this case the arrays of electrodes, used to deliver the charge to the tissue, are implanted subcutaneously in the occipital region right above the occipital nerves, as shown in Figure 2.3.a. These electrodes are connected to a battery pack somewhere in the chest or the abdomen [6]. The device is easier to implant because it does not require any craniotomy. The advantages of this type of device include full implantability and minimally invasive surgery. The main disadvantage of this device is that it requires a secondary implant with the battery and controls. This limits the life span of the implant to the one of the battery. In addition, the use of wire to connect the battery to the electrodes introduces some unreliability on the system. Wires are sources of failure, losses, and potentially induce parasitic electromagnetic fields along the path of the wire. Thus, in an ideal system, it would be desirable to eliminate this second component.

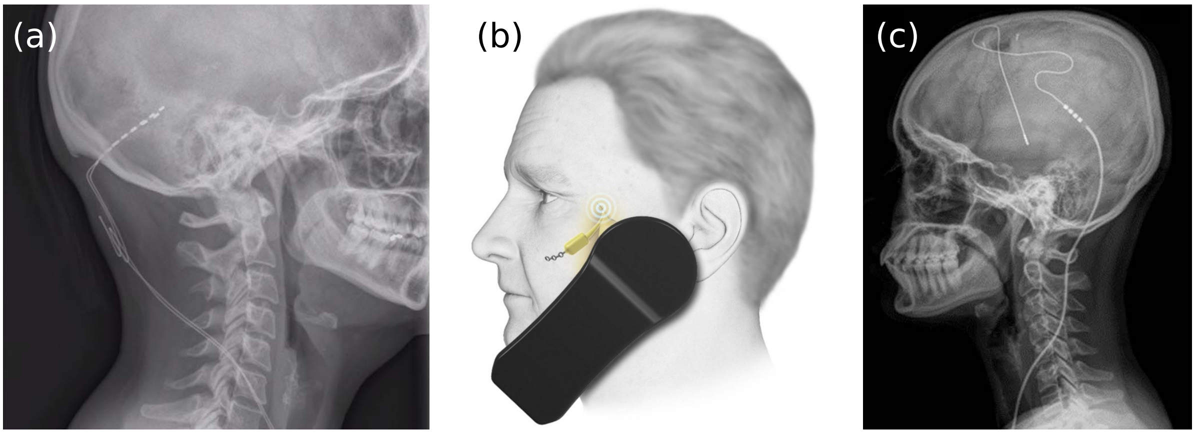

Figure 2.3: Different invasive stimulation devices. **a)** Occipital nerve stimulator used for preventive treatment of refractory chronic migraine and cluster headaches. **b)** *Pulsate SPG* device for SPG nerve bundle stimulation. Used to prevent chronic cluster headaches. **c)** Deep brain stimulator for ventral tegmentum and posterior hypothalamic regions. Used for acute treatment of cluster headaches. Modified images taken from [6]

Other invasive devices are located deep inside the head without the need for craniotomy. The *Pulsate SPG* neurostimulators is an example of such a device. This stimulator delivers current pulses to the SPG nerve bundle, which is located extracranially [6]. Thus, there is no need for an invasive surgical procedure for implantation. The stimulator has been miniaturized and it operates with an internal battery. The miniaturization and ease of implantation are the most attractive characteristics of this type of device. Similarly to the occipital nerve stimulator, this battery would limit the life span of the stimulator, since it requires replacement after some years. This is not the only disadvantage of the device, since the remote control for the device has to be external and hand held by the patient [6] (see Figure 2.3.b).

Finally, the most invasive procedures are those for deep brain stimulation devices. These devices usually target the ventral tegmentum region and the posterior hypothalamic region [6]. This procedure is only used when the non-invasive options turn out to be ineffective for the patient. Similar to the occipital stimulation, this device has a set of electrodes that is implanted deep in the brain and a battery and control unit that are implanted somewhere else in the body. The connection between the two is done via wires, so all the disadvantages and unreliability that were discussed in the previous examples also apply to this particular type of stimulator. A deep brain stimulator can be seen in Figure 2.3.c.

2.1.2. Requirements for the Target Application

The target areas for this project will be the supraorbital and occipital nerves. In order to target such areas, there needs to be one electrode array for each of the nerves, adding up to four electrode sites in total, for the two supraorbital and two occipital nerves. This means four neurostimulators for each of the electrode arrays, since the use of wires introduces unreliability and possible failure points.

All the examples of non-invasive and invasive simulators illustrate the main challenges when designing systems for headache diseases. These challenges can be used to determine the characteristics of each of the neurostimulators. Firstly, such devices should not require the active participation of the patient (no hand held components). It should also be small in size to make them implantable. Miniaturization should be a priority to minimize the invasiveness of the surgical procedure (if one is needed). Secondly, the system should be long lasting and reliable. This means the elimination of implanted wires and batteries. Finally, it should be able to predict or monitor the nerve activity at the implantation site. This would mean that the device can be used not only for headache suppression, but for headache treatment and prevention.

2.2. Active Implantable Biomedical Microsystems (AIBMs)

Considering the application requirements, the AIBM needed to perform the chronic headache treatment should excel in: implantability and durability, efficacy and safety. Good implantability is achieved through miniaturization, which involves wireless power transfer methods. Durability can be greatly improved by means of replacing batteries with said wireless power transfer link, as well as by reducing the overall power consumption. Efficacy and safety can be guaranteed by means of adding charge metering and charge balancing topologies. The state of the art regarding the above-mentioned requirements is further explained here.

2.2.1. Wireless Power Transfer

During the application review, it was discussed that the use of wires in implantable devices adds sources of failure as well as additional power losses. For the proposed system, it was decided to power the implants wirelessly. The wireless link introduces some additional challenges like power efficiency, implantation depth. safety, etc. In addition, there is a need for an external transmitter which delivers the required power to all four neurostimulators within the proposed system.

2.2.1.1. Standard Techniques

In principle , there are many ways of wirelessly transferring power inside of the body. The most common technologies for wireless power transfer (WPT) are: acoustic power transfer (APT) using ultrasound (US), radio frequency far-field power transfer (RF), and near-field inductive coupling (NF). There are a couple of differences between these three methods, which might be beneficial or not depending on the specific application. The different regions of operation for the three techniques are depicted in Figure 2.4.

The depth of operation of the wireless power link is determined by the distance between the transmitting end outside of the body and the implant itself. The implant can be at different depths depending on the application. For example, for deep brain stimulation the implant can be several centimeters inside the body, whereas for a cochlear implant, the device is much closer to the surface. Thus, the first consideration when choosing the powering method is the location of the implant. If the three methods are compared, it can be seen that ultrasound reaches deeper in the tissue (>10 cm) [7, 8]. This means that the energy can be focused at large depths of over 10cm with higher power transfer efficiency. The use of inductive coupling has been widely used for near-field (short distance) power transfer. If the coils are big enough and the alignment is precise, the power transfer efficiency can outperform the other methods. Cochlear or Retinal implants are examples of systems that use inductive coupling for the power transfer. Far-field RF either requires a large distance or very high frequencies (to be in the far field). As a consequence, it will have limited power efficiency, as the path loss is large, so it is most of the times not chosen as the preferred method.

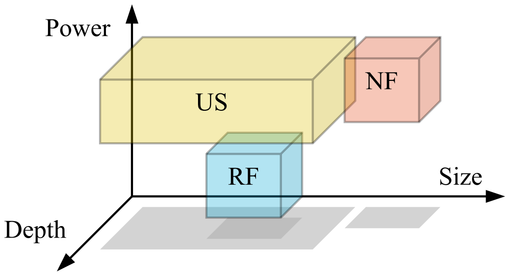

Figure 2.4: Operation limits for the three different wireless power transfer (WPT) methods, namely ultrasonic (US), RF far-field (RF), and near-field inductive coupling (NF). Image inspired from [9].

As hinted in the previous paragraph, the size of the implant plays a very important role when deciding on an optimal power transfer method. If the implant is deep in the body and in the sub-mm size range, then ultrasound outperforms far-field RF, as mentioned above. Regarding the efficiency, ultrasound has a better transduction efficiency because the wavelengths are smaller (mm) and the tissue attenuation is low [9, 10]. For near-field applications, US is better than inductive coupling because of the inefficiency in systems smaller than around 5 mm [10]. Inductive coupling requires cm-scale coils that occupy larger volumes [11]. Although

US seems as the most promising option for small implants, the desired distance for maximum power transfer is still in the transition from the near-field to the far-field. In the near-field, the acoustic waves interfere with each other creating regions of constructive interference and destructive interference (highs and lows in amplitude). This effect is referred as the near-field standing wave [12]. If the transmitter is too close to the receiver, then the efficiency might decrease significantly because the receiver might be in one of the lows of the standing wave [12]. There are ways of fixing this by changing the operating frequencies until the device is placed on a peak of the standing wave, but the specifics will be explained later in paragraph 2.2.1.2.1.

Finally, side effects and stability concerns have to be accounted for when choosing the desired WPT method. Regarding stability of the implant (biostability), US does not interfere with the electromagnetic fields of the implants due to it's acoustic nature [7, 8]. This is not the case for near-field inductive coupling or far-field RF. In terms of biocompatibility (safety for the tissue), due to losses in the tissue (either conductive, dielectric or mechanical) the temperature may rise in all three WPT methods. Thus, the electromagnetic methods are only compatible if used withing some safe intensity regions. Similarly, US is safe to the human body at the standard desired frequencies and power levels [10]. These safe frequencies are in the range of several hundreds of kHz to several MHz. In conclusion, US causes less interference in the circuitry and it is also biostable, making it the most suitable option for most applications. But, although US is safe and reliable, it might still cause some side effects in neural activation. This topic is extensive so it will be explored in depth in Section 2.3.

Regarding this project, the system includes four separate neurostimulators which need to be simultaneously powered. It was theorized that they could be powered using an ultrasonic link using the skull bone as the conductor. This system conceptualization will be further explored in Chapter 3

2.2.1.2. Ultrasonic Wireless Power Transfer Transducer

Once the acoustic energy has been transferred along the skull, there is a need for an electro-mechanical transducer element that converts said energy from the mechanical domain to the electrical domain. There are various kinds of ultrasonic transducers, which will be described and compared in the following subsections. There are multiple factors to consider when comparing different ultrasonic transduction methods.

Firstly, the acoustic impedance of the transducer and the propagation medium (bone in this case) should be close to each other. When there is a mismatch in acoustic impedance, part of the acoustic energy is reflected and lost. The reflection coefficient can be calculated using the following equation [12]:

$$\Gamma = \frac{Z_{bone} - Z_{transducer}}{Z_{bone} + Z_{transducer}} = \frac{P_\mathrm{r}}{P_\mathrm{i}} \tag{2.1}$$

In Equation 2.1, Z_{bone} represents the acoustic impedance of the propagating medium, or bone in this particular application, and $Z_{transducer}$ represents the acoustic impedance of the ultrasonic transducer. Γ can also be interpreted as the ratio of the amplitude of the reflected ultrasonic wave P_r and the amplitude of the incident wave P_i [12]. If two mediums have different acoustic impedances, a matching layer between them can be introduced to minimize the reflection of the US incident waves. The acoustic impedance ($Z_{matching}$) and thickness ($th_{matching}$) of the matching layer depend on the acoustic impedances of the media and the wavelength (λ) of the propagating wave, respectively [12]:

$$Z_{matching} = \sqrt{Z_{bone} \times Z_{transducer}} \tag{2.2}$$

$$th_{matching} = \lambda/4 \tag{2.3}$$

The thickness of the matching layer is dependent on the frequency, thus the matching will only be effective within a small frequency range. In other words, the bandwidth is compromised. In this case, the ultrasonic link is mainly used for power transfer, therefore the frequency bandwidth does not have to be wide. What's more, the best energy transfer is obtained in case of resonance and thus at a fixed frequency.

Secondly, the Q factor of the ultrasonic transducer should be as high as possible. Q is defined as:

$$Q = \frac{f}{BW} \tag{2.4}$$

A higher Q is better for power transfer, while a lower Q is better for imaging applications, for example. In this case, the ultrasonic link is mainly used for power transfer, thus a higher Q factor is desirable.

Ultimately, the most important parameter from an ultrasonic transducer is the coupling coefficient. The coupling coefficient specifies how efficiently the mechanical energy is converted into electrical energy in the ultrasonic transducer [13].

$$k_T^2 = \frac{E_{\text{elec}}}{E_{\text{mech}}}, \tag{2.5}$$

where E_{mech} is the input mechanical energy and E_{elec} is the converted electrical energy. The highest the coupling coefficient k_T^2 is, the better is the transduction from one energy domain to the other. In other words, the energy is transduced more efficiently.

Knowing the different parameters that characterize the transduction efficiency, the following transducers are compared.

2.2.1.2.1 PZT vs. MUTs: There are two distinct types of ultrasonic transducers: Micromachined Ultrasonic Transducers (MUTs) and Piezoelectric Ultrasonic Transducers (PZTs). The first are realized using microelectromechanical systems (MEMS), whereas the second are implemented using piezoelectric ceramic materials.

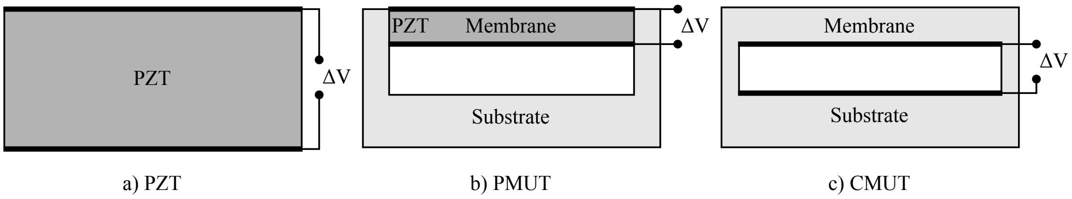

Figure 2.5: **a)** Piezoelectric transducer. The deformation in the crystal lattice generates a difference in potential. **b)** Piezoelectric Micromachined Ultrasonic Transducer. The deflection of the membrane deforms the PZT generating a voltage difference. **c)** Capacitive Micromachined Ultrasonic Transducer. The deflection of the membrane generates a change in capacitance between substrate and membrane, which can be detected as a voltage or current difference.

Micromachined ultrasonic transducers (MUTs) are composed by a membrane structure. This membrane vibrates when the ultrasonic wave hits it and deforms the PZT generating a potential difference in the case of Piezoelectric Micromachined Ultrasonic Transducers (PMUTs), or it is transduced to the electrical domain as variations in the capacitance between the membrane and the substrate in the case of Capacitive Micromachined Ultrasonic Transducers (CMUTs) (Figure 2.5). CMUTs have lower acoustic impedances and, as a result, these devices are very easy to acoustically match with air and fluid mediums [14].

PZTs are constructed with piezoelectric ceramic materials where the deformation in the crystal lattice generates a difference in potential. When performing ultrasonic investigations in solids, piezoelectric transducers might be preferred due to their higher acoustic impedances, however, the difference in impedance with respect to fluids makes them very unsuitable in said mediums [15]. If they were to be operated in fluids, they would require a matching layer, which introduces three problems. Firstly, the matching materials required are rarely available. Secondly, the higher energy coupling compromises the bandwidth of the system. Thirdly, high frequency transducers require impractically thin matching layers [15].

Piezoelectric ultrasound transducers are big in size, so they are not as suitable for implantable biomedical devices [16]. In addition, they have very small bandwidths, which makes them hard to be operated. In the near-field range of the ultrasound transfer, the standing wave effect is significant, lowering the power transfer if the receiver is in one of the valleys of said standing waves. As a result, a device with higher bandwidth is desired (MUT), as the transmitting frequency can be tuned so that the power transfer in the near-field is as high as possible, similarly to what is done in [16].

2.2.1.2.2 PMUTs: In standard Piezoelectric MUTs (PMUTs), the two electrodes are located in the top and bottom side of the membrane or diaphragm. As a result, the capacitance across the electrodes is larger than in CMUTs operated in the conventional-mode [14]. As transmitters, the electric field between the top and bottom electrodes generates some transverse stress that forces the membrane to bend by the inverse piezoelectric effect [14]. In their receive mode, PMUTs deflect due to an incident acoustic wave, and charge is generated between the two electrodes due to the direct piezoelectric effect [14].

The PMUT has a characteristic that is particularly useful for bio-implantable power applications: it can operate at much lower frequencies that the standard PZT transducer and, as a result, there is less signal/power attenuation and tissue heating [17]. It has also been shown that for sub-millimeter range, the PMUT generates more power than the standard PZT and it is significantly less sensitive to changes in implant depth due to the lower path loss at those lower frequencies [17].

When it comes to PMUTs, the uniformity of the piezoelectric activity of the different membranes is hard to achieve [18]. Also, they sometimes contain materials that are toxic to the tissue like lead [16, 19, 20], and their fabrication is usually not compatible with standard micromachining techniques [18]. Some PMUTs are developed using alternative materials like zinc oxide (ZnO) [21], but they still carry all the other disadvantages mentioned above. Another alternative is aluminum nitride (AlN), which can be deposited at low temperatures, allowing for compatibility with standard CMOS processes [14, 22, 23].

PMUTs might still be a good option for other types of applications like catheters, where the devices are not being implanted. As a result, the toxicity of some of the components is not as critical [20].

2.2.1.2.3 CMUTs: Capacitive MUTs, also known as CMUTs, are CMOS compatible. They are composed by membranes that vibrate when an acoustic wave interacts with the device. The variation in capacitance when the membrane vibrates can be detected, thus the acoustic wave can be transduced into an electrical signal. In other words, the sound vibration is measured by two electrodes and converted into a modulated capacitance. Many individual CMUTs can be coupled together in an array and be used as a single transducer element. One of the great advantages of CMUTs is that they have a bandwidth of 100% at -6dB for the applied bandwidth [24].

In the case of CMUTs, the element size should be approximately half of the ultrasonic wavelength. Early designs of CMUTs already achieved coupling coefficients of $k^2 > 0.5$ [25], which compete with other ultrasonic transducers. Nowadays these coupling coefficients can be even higher in some cases. In order to achieve these higher coupling coefficients, the CMUTs are usually biased. Different biases or modes of operation will determine the sensitivity and coupling coefficients of the transducers.

The following can be said regarding mechanical and thermal properties. In regular fabrication processes, the holes used to empty the sacrificial layer that releases the membrane are a disadvantage that compromises the uniformity of the membrane vibration. The designs proposed by [26] avoids the holes problem and, in addition, it doesn't use silicon for the mechanical support (high acoustic impedance) but silicon nitride instead (for better backing and less ringing). CMUTs also exhibit less self-heating than PZT transducers as well as less dielectric losses [27].

Mode of Operation

There are a couple of ways to improve the transduction efficiency of CMUTs. The first one is to introduce a bias voltage to improve resonance (Figure 2.6.a), and the second one is to operate in collapse mode (Figure 2.6.c) where the capacitance of the CMUTs increases as the two plates get in contact with each other, which also requires a much larger biasing voltage. The closer the membrane is to the substrate, the more sensitive the CMUT becomes. In other words, the proximity of the two plates causes a greater coupling between acoustic and electrical signal energy [24]. Initially, one of the main advantages of using PMUTs vs CMUTs is that they don't require biasing voltages in order to achieve the desired sensitivity [14], but there are two techniques that can be used to increase k^2 in CMUTs without biasing, as explained below.

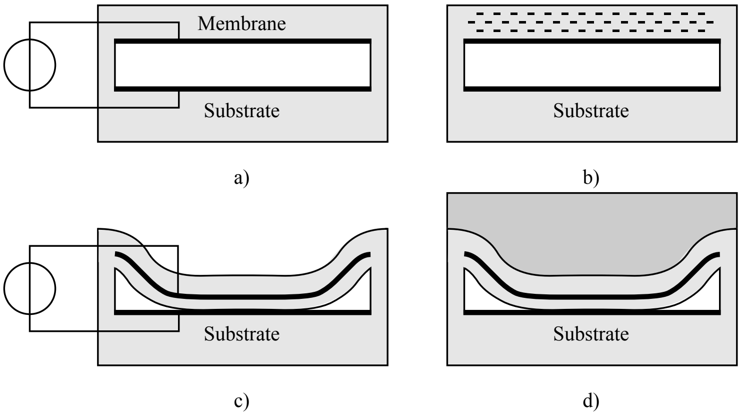

Figure 2.6: **a)** CMUT at regular operating mode with applied bias voltage. **b)** Pre-charged CMUT at regular operating mode with zero applied bias voltage. **c)** Electrically collapsed CMUT at collapse operating mode with applied bias voltage. **d)** Mechanically pre-collapsed CMUT at collapse operating mode with zero applied bias voltage.

Pre-charged: The problem of biasing CMUTs is great because they usually require voltages that are impractical to be implemented in an implantable device. An innovative solution to this problem is presented in

[28], where a DC electrostatic deflection at zero applied voltage is possible, due to trapped dielectric charges, as depicted in Figure 2.6.b. The deflected membrane can be used in the conventional mode of operation with the desired sensitivity. In [28] it is demonstrated that at zero applied voltage the CMUTs are more efficient than at some other biasing voltages. The power transmission of these CMUTs is comparable to some single element piezoelectric transducers, and their sensitivity is much higher [28]. But the trapped dielectric charges are not a product of the fabrication process of the CMUTs. As a result, these CMUTs have to be pre-charged prior to their usage by means of collapsing the membrane with voltages higher than two times the collapse voltage. This process traps the charge in the dielectric and when the applied voltage is removed, these trapped charges improve the resonance of the membrane during the CMUT operation.

In [29] the approach is very similar. An electrically floating island is charged using a bias voltage much higher (2.5 times) than the collapse (or pull-in) voltage. This creates a sufficiently strong intrinsic electric field between the two electrodes in the substrate and the membrane. In [29], it has been shown that the trapped charge can remain in place unchanged for at least 19 months (~1.6 years).

In [30] is was shown that these pre-charged CMUTs can be used for wireless power transfer to implants deep in the body (around 7 cm). The presented CMUT had an efficiency of 76% and the overall power link had an efficiency of 0.3% considering the tissue attenuation across 7 cm.

Pre-collapsed: When a regular CMUT is biased to bring the plates closer together, only the central part of the membrane will be in close proximity to the other plate, thus being sensitive in a very small region. When the membrane is operated in the collapse mode, a greater region (ring) experiences the small distance between the two plates, and as a result the overall sensitivity if the CMUT would be higher. In order to operate the CMUT in a collapse mode, a large voltage (tens of Volts) is required, which makes the device hard to implement into medical implantable devices. As a result, in [24] a technology is proposed that allows the membrane to be in the collapse mode without external applied voltages. In this case, the electrostatic force required to collapse the membrane is substituted by a mechanical support that holds the membrane in the collapse mode, seen in Figure 2.6.d.

The CMUT coupling coefficient is a measure of the efficiency of energy storage by the device, and it can be calculated using the following equation [24]:

$$k^2 = 1 - \frac{C_s}{C_T}, \tag{2.6}$$

where $C_s = \frac{Q}{V}$, $C_T = \frac{dQ}{dV}$, $Q = Voltage$ and $V = Voltage$.

When the membrane is brought from the conventional-mode to the collapsed-mode and then brought back from the collapsed-mode to the conventional-mode, the coupling coefficient exhibits a hysteresis effect. In other words, it is not symmetrical. this is the main reason why CMUTs have to be operated in one of the modes only. With the proposed pre-collapsed CMUTs in [24], the hysteresis problem disappears, so when the voltage is increased or decreased, the coupling coefficient changes in the same way. A typical piezoelectric transducer (PZT) has an effective coupling coefficient of 0.42, while with the proposed CMUT in [24] the coupling coefficient can be increased to 0.65, approximately.

In order to apply the mechanical structure (lens), the membrane needs to be held in the collapse mode by using bias voltages or pressure. Then a lens can be deposited. The advantage of the lens is that it provides additional functionalities to the transducer: mechanical structure, robustness and a physical cover; it provides electrical insulation as the lens is non-conductive; it provides focal properties; and finally it can also provide acoustic matching to the system. The materials used can be PDMS for example. The performance characteristics of each membrane can vary due to small tolerances in membrane thickness and size, but this can be easily adjusted by applying the required small voltages to each of the membranes until they all match together [24].

In conclusion, CMUTs are an innovative and new solution that can satisfy the power demands of an AIBM. All the advantages mentioned before, in addition to the fact that they can compete against traditional methods like PZT in terms of transduction efficiency, make CMUTs in pre-collapsed or pre-charged modes of operation a good WPT solution for this project.

2.2.1.3. Bone Acoustic Conduction

As mentioned earlier, the proposed system utilizes the acoustic conductive properties of the bone to transfer ultrasonic power to the four neurostimulator implants. In order to determine the energy levels and requirements for such implants, it is crucial to understand the acoustic conductive properties of skull tissue.

Measurements of bone acoustic conduction have been made since as early as the 1940s. The early measurements concluded attenuations of 10 dB cm^{-1} to 40 dB cm^{-1} for 1 MHz to 3 MHz, but the measurement setup was not very rigorous. Two decades later, in [31], the first rigorous measurements (with human specimens) of acoustic properties in bone such as velocity of sound, acoustic impedance and acoustic absorption were made (for MHz frequencies). For the application presented in this paper, the measurements of the acoustic bone absorption are the most relevant. The initial results in [31] show attenuation values of 19.19 dB cm^{-1} to 24.60 dB cm^{-1} for outer and inner cortical bone in skull, and 16.1 dB cm^{-1} for diploe bone. Ever since these results were published, many more studies have been made to measure attenuation and absorption values for different acoustic frequencies. The values of the measurements have been in disagreement (sometimes orders of magnitude) between studies due to the different measurement setups [32]. For example in [33] values of attenuation are 1.22 dB cm^{-1}, 4.6 dB cm^{-1}, and 6.08 dB cm^{-1} for 0.272 MHz, 0.548 MHz and 0.840 MHz respectively; whereas in [34] values of 2.78 dB cm^{-1} and 21.19 dB cm^{-1} were found for 0.27 MHz and 0.836 MHz. These differences are very high even though the studies were made only four years apart. Another example is the attenuation of 15.7 dB cm^{-1} for 2.25 MHz measured in [35] versus the values found in [34] for 1.965 MHz and 2.525 MHz, which were too high to be measured according to the source.

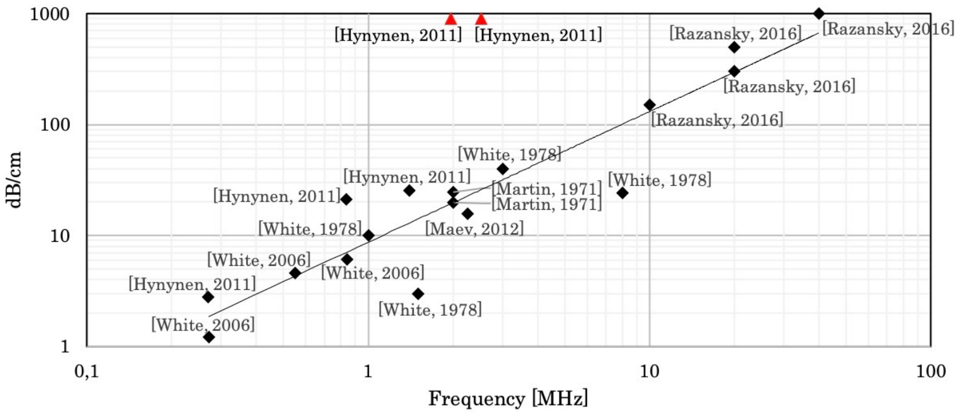

Figure 2.7: Attenuation measurements of different studies. The attenuation of cortical bone was used for those studies that made distinctions between cortical and diploe bones. A power line fit was also plotted with a coefficient of determination $R^2 = 0.87$, which shows some sort of trend. The values of 1.965 MHz and 2.525 MHz from [34] are presented in red because their attenuation could not be measured.

Figure 2.7 shows all the data points extracted from [31–36]. In this plot, a frequency of 2 MHz was selected for [31], since the actual value was a range from 1-3 MHz. As it can be appreciated, there is some trend between all data points, which answers to a power relationship between attenuation and frequency. Some data points were still not included in the graph, like the values of 1.965 MHz and 2.525 MHz from [34]. This is due to the fact that for these frequencies, no signal was measured during the experiments, indicating that the attenuation was too high to be detected. In [34], the experimental setup used an ultrasonic transmitter placed at some distance below a sample of human skull. The transmitter was focused on the center of the sample and the signal at different points on the surface was measured, thus calculating the attenuation with respect to a central position. This setup lead to very small signals, so the undetectable ultrasounds at high frequencies might be due to a measurement equipment limitation rather than the actual attenuation of the bone at those frequencies.

Although the frequencies follow some sort of trend (Figure 2.7), the variation of results for a given frequency is still significant. All the data points used for Figure 2.7, as well as the ones that were not included are tabulated in Table 2.1. The variance between results might be too high to come up with a prediction for the real attenuation. The attenuation is very important to know for the specific application. The circuitry in a neural stimulator has power demands of around 10 µW to 100 µW in standby ([3, 37, 38]), while the power required during stimulation is in the order of 10 mW to 20 mW [38–40]. Hence, the power received by the different neurostimulators needs to be around tens of mW and the transmitter has to be designed to emit as much power as needed to reach that level.

The values for attenuation are disagreeing at some frequencies, and the measurement setups were different for all studies. Thus, a finite element simulation of the propagation of ultrasound on the human skull

Table 2.1: Attenuation of skull bone for different GHz-region frequencies. This table contains results from studies made over the past fifty years

	Frequency [MHz]	Attenuation [dB cm^{-1} MHz^{-1}]		Attenuation [dB cm^{-1}]	
		Cortical Bone	Diploe Bone	Cortical Bone	Diploe Bone
[36]	10-20	15*		150-300**	
	20-40	25*		500-1000**	
[34]	0.27	10.29**	10.94**	2.78	2.95
	0.836	25.35**	25.35**	21.19	18.76
	1.402	18.21**	23.23**	25.54	32.57
	1.965	-***			
	2.525	-***			
[32]	1	10**		10*	
	3	13.33**		40*	
	1.5-8	2-3*		3-24**	
[31]	1-3	6.63-24.6**	5.37-16.1**	19.9-24.6	16.1
[35]	2.25	6.98**		15.7*	
[33]	0.272	4.49**		1.22*	
	0.548	8.39**		4.60*	
	0.84	7.28**		6.08*	

* = The study does not make a distinction between diploe and cortical bones.
** = Calculated values using the information in the studies.
*** = This study argues that the attenuation was so high that it couldn't be measured.

is performed in Chapter 3. This simulation is able to account for many different frequencies, as well as geometries and other variations of the skull bone between different humans. Even though the simulation is not of the highest accuracy, it is homogeneous in methodology across all frequencies and other parameters. In other words, the behavior is correctly simulated, and the actual values can then be adjusted based on further experiments.

2.2.2. Power Efficiency: Ultra High Frequency Stimulation

Conventional neurostimulators use DC power sources to deliver the electrical stimulus. The reason for this is the good control of the charge injected, since DC currents are easily generated, their amplitude is constant, and the duration of the pulses is easily controlled. The disadvantage with this method regarding current delivery is related to power consumption. The generation of DC currents is power demanding because it requires extra components (AC/DC converters, DC/DC bust converters, etc) to generate it. Furthermore, these DC supplies are usually implemented by means of batteries, which increase the size of the stimulator and reduce their lifetime.

As explained in the previous subsection, an alternative is to deliver the power wirelessly, which requires the use of AC power signals. As a result, most wirelessly powered implanted neurostimulators contain some sort of AC to DC power conversion unit, like a rectifier. An recent alternative for these systems (using AC to DC converters) is to introduce the ultra high frequency (UHF) pulsed technique for the stimulation. In this paper, *Low frequency* (LF) stimulation and *high frequency* (HF) stimulation refer to the frequency of the stimulation pulses, while *ultra high frequency* stimulation refers to the frequency of the AC signal used to build up each individual (LF or HF) stimulation pulse.

UHF stimulation can lead to neural activation [41, 42], thus potentially eliminating the need for AC to DC converters and other components, which consume area and power. Furthermore, both UHF stimulation and ultrasonic wireless power transfer work in the MHz frequency range, so the ultrasound signal can be "directly" used for the electrical stimulation of the tissue by means of a simple transducer [7].

The principle of operation of UHF stimulation is the following. It uses the capacitive behavior of the neuron membrane to integrate the current over time and accumulate enough charge to elicit an action potential [42]. As a first approximation, if the membrane is considered as a capacitor, the integration of the current over time is straightforward to understand. This can be easily seen using the standard capacitor equations:

$$i_m = c_m \frac{dV_m}{dt} \tag{2.7}$$

$$V_m = \frac{1}{c_m} \int i_m + V_R \tag{2.8}$$

, where C_m is the capacitance of the membrane, i_m the current across it, V_m its voltage, and V_R its resting voltage level. But the total amount of charge injected also depends on the tissue impedance [42]. In other words, although the ultra high frequency stimulus is integrated on the axon due to the capacitive properties of the cell membrane, the resistive component of the membrane should be taken into account as well. This is studied using the cable model for the membrane [43]. This cable model is represented using the following equivalent circuit for the axon:

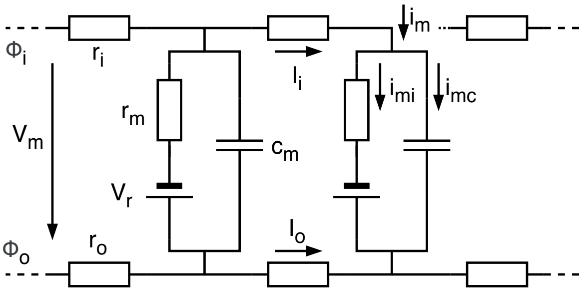

Figure 2.8: Cable model of the axon. $\Phi_{i,o}$, intracelular and extracelular electric potentials. r_i, intracelular axial resistance of axoplasm. r_o, extracelular axial resistance of extracelular medium. r_m, radial membrane resistance. c_m, membrane capacitance. $I_{i,o}$, total longitudinal intra/extracelular current. i_m, total transmembrane current. $i_{mc,mi}$, capacitive/ionic component of the transmembrane current. V_m, membrane voltage. V_R, resting membrane voltage. Model taken from [3].

Based on Figure 2.8, the following cable equation can be derived when the cell membrane is stimulated with a step current:

$$-\lambda \frac{\delta^2 V'}{\delta x^2} + \tau \frac{\delta V'}{\delta x} + V' = 0 \tag{2.9}$$

$V' = V_m - V_R$ is the deviation of the membrane voltage, $\lambda = \sqrt{\frac{r_m}{r_i + r_o}}$ is the length/space constant, and $\tau = r_m c_m$ is the time constant. In terms of Equation 2.9, the response of the cell to ultra high frequency stimulation can be seen as the time constant of the axon filtering the AC signal and raising V_m [42].

The UHF technique has been applied in existing literature by means of charging and discharging and inductor from a DC source for the ultra high frequency pulse generation [41]. An advantage of such a design is that the ultra high frequency pulses can be distributed to different electrodes in an alternating fashion. This is important when aiming for a multichannel configuration [41]. In turn, the intensity of the stimulation at each channel can be independently controlled by properly distributing the ultra high frequency pulses. This solves a common power efficiency problem present in most multichannel neurostimulators, where all channels must remain at the highest power level required by the most demanding channel, which in turn results in unwanted power dissipation at all the remaining channels. With the appropriate control in place, this multichannel operation could be extended to the case where the incoming signal from the ultrasonic WPT link is "directly" used to build up the UHF stimulation pulses, as previously mentioned.

One drawback of the UHF stimulation technique is that there are no studies that evaluate the effect of ultra high frequency stimulation over long periods of time [41].

There are many other ways of improving the power efficiency of the entire system. A few examples might include the use of Gaussian shaped waveforms as compared to standard rectangular pulses [41], or introducing inter-pulse delays [41]. The scope of the project did not include the optimization of the power consumption of the proposed neurostimulators, so those techniques that require extra circuitry (like the use of Gaussian shaped pulses) were not included in the design. Nevertheless, all the other techniques like the UHF stimulation or the inter-pulse delays, which did not require any extra components, were implemented in the project.

2.2.3. Stimulation Safety: Charge Balancing

Before analyzing the state of the art with respect to electrical stimulation efficacy and safety, it is crucial to make sense of the electrode tissue interface and the mechanisms of activation. Many state of the art designs cannot guarantee stimulation safety because of a poor interpretation of the electrode-tissue interface response to electrical stimulation. Thus, a detailed explanation of such an electrode-tissue interface behavior under stimulation follows.

Initially, when the electrodes are placed in the tissue, a redistribution of charge occurs in the electrode-tissue interface resulting in an intrinsic potential, referred to as the *half-cell* potential (E_{hc}) shown in Figure 2.9 [3]. This potential is always present, even when no stimulus is applied to the electrode. When the electrode is supplied with an electric source, there are two main mechanism in which charge can flow through the electrode tissue interface: non-Faradaic reactions where there is no transfer of electrons but redistribution of chemical species, and Faradaic reactions where electrons are being transferred between electrode and tissue, thus leading to reduction-oxidation (redox) reactions [44].

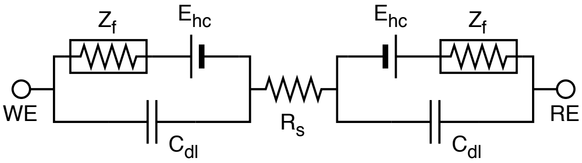

Figure 2.9: Load model base on a dual electrode tissue interface topology. The two access points are the working and return electrodes, WE and RE. C_{dl} represents the double layer capacitance and E_{hc} the half-cell potential. R_s represents the resistive behavior of the tissue, and Z_f represents the impedance that relates to the Faradaic reactions that occur at the electrode tissue interface

The double layer capacitance C_{dl} depicted in Figure 2.9 represents the charge transfer through said non-Faradaic reactions. This redistribution of charge is said to be reversible because if the polarity of the stimulus is reversed, the chemical species in the tissue return to their original locations [44]. Z_f represents the Faradaic transfer of charge through redox reactions. It is represented as an impedance that models the different redox reactions that might contribute to charge dissipation or loss [44]. In general terms, these reactions are considered to be irreversible, and in most cases unwanted, as they can damage the tissue and the electrodes. There are cases where they can be reversed if the polarity of stimulus is flipped fast enough, such that the recently formed products of the redox reactions are still at the interface and can be reversed [44], but this is usually not the case. It general terms, for small electrode over-potentials, the capacitive (non-Faradaic) branch dominates while the Faradaic resistive branch is only significant when large potentials are applied to the electrodes.

The reduction and oxidation of electrodes or tissue are unwanted mechanisms. The biostability of the system is compromised if the device is damaged, and the biocompatibility is compromised if the tissue is damaged. In this work, the safety of the neurostimulator will be maximized by reducing the number of Faradaic irreversible reactions during the stimulation cycles.

2.2.3.1. Charge Delivery Methods and Stimulation Pulse Modalities

Conventional neurostimulators use current or voltage sources to deliver the required charge to the tissue. Voltage-controlled stimulation, also know as potentiostatic stimulation, is less popular because the charge delivered cannot be controlled accurately, as it depends on the load impedance [44]. On the other hand, galvanostatic or current-controlled stimulation is very popular because the amount of charge is easily controllable by the stimulation current intensity and pulse width.

As hinted above, the stimulation is commonly delivered in the form of pulsing. These pulses can be monophasic, where the charge is delivered in one direction, or biphasic, where the pulse is divided into two charge delivery phases of opposite polarity [44]. The first phase in a biphasic pulse is called the stimulation phase as it elicits the desired physiological effect [44]. The second phase is called the reversal phase and it reverts the electrochemical processes that occurred during the stimulation phase [44]. Cathodic pulses are generally used for the stimulation phases, which means that the working electrode WE, where the stimulation is delivered, is driven more negative and depolarizes the close-by cell membrane. Anodic pulses are used for the reversal phase. It is possible to use anodic pulses for the stimulation phase, but the depolarization happens far from the WE, which requires three to seven times more charge to elicit cell activation, thus making this modality less precise and less energy efficient [44].

During the first cathodic phase of the stimulation pulse, the electrode potential is being moved away from equilibrium. The further away from equilibrium, the more irreversible Faradaic reaction will occur. This effect will continue until the reduction of water happens through the process of electrolysis. From that moment onwards, and due to the high water presence, all the extra charge will be exclusively transferred through the reduction of water [44]. The water oxidation is also a limiting threshold when the electrode is driven positive during the anodic phases. Since the cathodic phase will inevitably lead to some irreversible Faradaic reactions, the amount of charge required to revert the voltage across the double layer capacitance C_{dl} during the anodic phase will always be a fraction of the one used in the cathodic phase [44]. State of the art designs still fail to understand this process, and they wrongly assume that the perfect charge injection matching between anodic and cathodic phases would lead to safety. If the two phases are perfectly matched, the potential at the electrode would increase over multiple periods, which results in unwanted electrode corrosion [44]. The reduction-oxidation window, widely referred as the water window, is used as a reference for the acceptable potential levels across the electrodes after each stimulation pulse.

2.2.3.2. Charge Balancing: State of the Art

In theory, blocking capacitors can be used to block any unwanted DC current signals, thus preventing any charge buildup. But in practice, due to the non-linearity of the electrode-tissue interface, higher frequencies still can cause charge buildup as explained above, so blocking capacitors are neither necessary not effective [45]. Apart from these capacitors, there are two main approaches to achieve charge balancing. The first one is through passive topologies that do not require any measurement of the residual voltage, and the second approach involves active topologies that measure the residual voltage and act accordingly.

Passive discharge is the simplest charge balancing technique. This is done by shorting the electrode by means of a MOS switch, during the interpulse delay. Here the interpulse delay refers to the time between consecutive biphasic pulses. Passive discharge does not prove to be a good method on its own because the time it takes to discharge the electrode-tissue interface might be larger than the interpulse delay, which would not give enough time for the electrode to go back to its resting potential [9]. But this technique might be very useful in combination with other methods in order to get rid of any last small residual charge. This passive discharge can be seen in Figure 2.10.c.

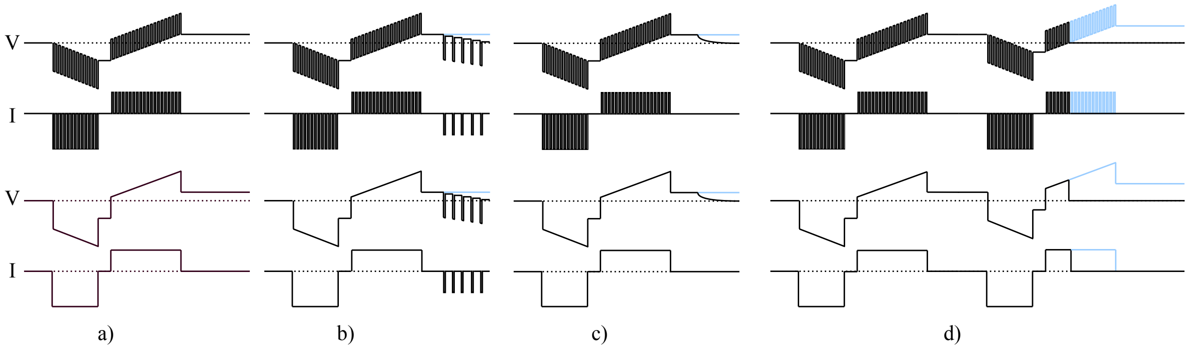

Figure 2.10: Different charge balancing techniques using the UHF technique (top) and a regular DC source (bottom). Blue represents the case with none of the charge balancing techniques. **a)** No balancing because due to a perfect match between cathodic and anodic phases. **b)** pulse insertion. **c)** Passive discharge. **d)** Offset regulation.

One of the most common techniques being used to charge balance the stimulation pulses is called the push-pull charge matching. This technique consists of perfectly matching the cathodic and anodic charge injection, like in [38, 46]. As explained before, this approach is fundamentally wrong because there are always Faradaic reactions happening during the cathodic phase, resulting in an overall positive residual voltage after the anodic phase. The voltage buildup over consecutive pulses would eventually lead to electrode corrosion. This particular approach can be seen in Figure 2.10.a.

The simplest forms of push-pull charge matching assume a constant current source that will not change between cathodic and anodic phases, remaining perfectly constant. In [47] the H-bridge topology is simply used to deliver current in the first and second phases for the same period of time. Often, the second anodic phase has lower current intensity and longer phase width in order to avoid unwanted effects such as unwanted activation or electrode corrosion, thus the approach in [47] becomes unsuitable too. Furthermore, as stated in [45], the timing control of the phases would suffer from inaccuracy due to process variations. One way around it is to sample the current during the first phase and adjusting for it in the second phase [48]. Many designs match the pull and push currents using charge metering topologies. Some of those metering topologies are shown in [37, 49–54]. A detailed description of the possible charge metering topologies will be explained in Subsection 2.2.4.

Pulse insertion is another popular active charge balancing technique. For this, a comparator is introduced to measure the remaining voltage at the electrodes, and the remaining charge is removed by means of small cathodic pulses. Examples of designs that use pulse insertion are [55, 56]. Some systems like [43] even allow the use of one single comparator because the charge balance can be performed one by one for all channels.

Another active closed-loop topology, referred to as offset regulation, uses feedback from the electrode voltage to adjust the stimulation parameters, and the time available to discharge [57, 58]. For example in [42] the residual voltage is measured after each pulse in order to adjust the second phase of the subsequent pulse. The disadvantage of this design is that it requires a comparator or amplifier per channel, which makes it not easily scalable. This approach can be seen in Figure 2.10.d.

Some recent designs combine multiple of these techniques. In [59], the passive shorting, pulse insertion, and offset regulation are simultaneously used. [57] combines the push-pull and the offset regulation technique by measuring the current mismatch between the cathodic and anodic phases and adjusts for it in the next biphasic pulse.

One big disadvantage of the pulse insertion, passive discharge and offset regulation techniques is that they are *a posteriori*. There is no guarantee that right after the anodic phase of the first pulse there is no corrosion. Furthermore, by completing the stimulation cycle and bringing the charge back to zero, the power efficiency of these techniques becomes lower. Thereby, there is a need for an *a priori* technique that can work in a more preventive way. The working principle of an ideal design is shown in Figure 2.11, where the anodic phase stops right when the electrode voltage reaches zero, meaning there is no accumulated charge. In other words, a design where the voltage returns to its original equilibrium state. There are some designs that already accomplish this by means of introducing some self-oscillating circuitry that interrupts and resumes stimulation until net zero residual voltage is achieved [60, 61].

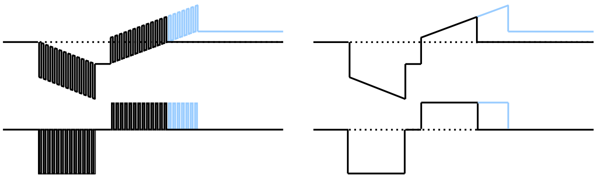

Figure 2.11: Ideal Charge balancing technique using a dynamic offset regulation with UHF stimulation technique (left) and with a regular DC source (right). Blue represents the case with none of the charge balancing techniques.

2.2.4. Efficacy: Charge Metering

In Figure 1.1.b it was shown how the effective activation of the tissue is dependent on the amount of charge being used for the cathodic phase of the stimulation pulse. This is easy to achieve if the energy source of the neurostimulator behaves like an ideal current source.

When the neurostimulator is being wirelessly powered, there are many factors that can affect the intensity and overall reliability of the received wireless energy. For example, if the alignment between the transmitter and receiver of the wireless power link shifts, or if the implant displaces a bit in the implantation site (e.g., due to body movement or change in position), then the energy transfer efficiency might change. In addition to this, the receiver, in this case a CMUT, does not behave like an ideal current nor voltage source.

Considering the importance of having a wireless power link that allows for miniaturization, as well as the importance of stimulation efficacy, there is a need for charge metering circuitry. This charge metering block ensures that, regardless of the input power levels or their unreliability, there is always enough charge in every cathodic phase to elicit activation.

Currently there are only a few designs that employ charge metering for this purpose. Most designs that include some sort of charge metering functionality, use that functionality to match the cathodic and anodic phases as explained in Subsubsection 2.2.3.2.

There are multiple ways of measuring the charge that flows through the stimulation path of the neurostimulator. The first technique connects a small series resistor and measures the current flow through it. This sensing resistor is connected to an integrator that integrates the sampled current as charge. This technique is being used in [49] and [50]. Right from the start, this topology is not ideal, as the series sensing resistor will introduce losses in the system. In addition to this, if the resistor is to be minimized, then there is a need for an amplification of the measured signal, which introduces extra amplifiers per channel.

A second possible technique is to use a capacitor in series with the stimulation path. Capacitors are current integrators by nature, so the total charge delivered to the tissue will be recorded in the form of a voltage drop across said capacitor. This approach comes with a trade-off between area and voltage drop. Ideally the capacitor would be very small to minimize the chip area of the neurostimulator ASIC. But small capacitors would lead to a large voltage drop in series with the tissue, which can compromise the stimulation efficacy. This charge metering approach is used in [51] and [52]. In both designs there is a need for an amplification of the voltage across the capacitor. In addition to this, the capacitors are being used to match the two phases of the stimulation pulse, but cannot be used to control the amount of charge that goes into the cathodic phase. In other words, the control of the charge is still being done in time. A better approach is being used in [54] where a capacitor is placed in series and charged with a small package of charge during stimulation. When the desired voltage threshold across the capacitor is reached, signifying that the unit package of charge has been fully stored in the capacitor, a comparator outputs a trigger signal that is sent to a counter. By charging and discharging the unit capacitor a specific number of counts, the total charge delivered to the tissue can be measured. The advantage of this design is that it allows for small capacitors and small voltage drops simultaneously. The only drawback is that the resolution of the charge metering is dependent on the number of counts. The topology in [54] will be further explained in Chapter 4 because it serves as the inspirational basis of the topology proposed in this thesis.

The third way of measuring the stimulation charge is by making a scaled copy of the stimulation current and apply any of the aforementioned techniques to measure the charge. With a smaller but proportional copy of the stimulation current, it is much easier to integrate the current [62]. In [63] this concept is applied, where a copy of the stimulation current is used to charge and discharge a smaller capacitor. The number of charges and discharges is outputted by a comparator to a digital controller. These approaches are very useful to accurately measure the stimulating charge, but they are still not very friendly with multichannel configurations as the current integrators are required per channel. In addition to this, their correct operation in the presence of UHF pulses is still uncertain.

2.3. Effect of Ultrasound in Electrical Stimulation

When the power is transmitted wirelessly via ultrasonic waves, these waves do not only reach the implant, but also the electrodes and the body cells as well. The presence of ultrasonic waves on the tissue can potentially modify the thresholds required to activate the cells electrically. In other words, the ultrasound can modulate the electrical stimulation being delivered by the neurostimulator. In addition, there is also a chance that the cells could be activated by the ultrasound stimulus alone.

It is important to study the effects of this side effect, because it could modify how the system works. If the effect is properly understood, then it can be accounted for and reversed, or even used to our advantage.

Early studies, like [64], explore the effect of ultrasound in the compound activity of excitable cells. In [64] it was established that the presence of ultrasound (500 kHz) can affect the cells mechanically and thermally, and change their response to electrical stimuli. The temperature was found to rise in the tissue by 1.4 °C after 5 min of ultrasound exposure. Similarly, in [65] an increase of the Compound Action Potentials (CAP) and Conduction Velocity (CV) were observed for ultrasounds at 5 MHz central frequency. The duty cycle was also found to play an important role (50 % lead to greater change in CAP and CV). The results show an increase of 41.3 % and 3.8 % for CAP and CV, respectively. Although [64, 65] study the effect of ultrasound, they do not offer any insight on the mechanism that leads to the change in cell activation.

Membrane cavitation is one possible explanation for the excitability of cells in the presence of US [4, 66]. In this scenario, a portion of the membrane expands and contracts as shown in Figure 2.12. The changes in membrane capacitance could induce changes in membrane currents that affect the stimulus response of excitable cells. In [4], it is theorized that rings of proteins could encapsulate sections of the membrane that expand and contract as a response to the incident pressure waves. Since the wavelength of the incident waves are in the order of mm, all parts of the membrane are subjected to similar effects from the incident US. In this study, the resting membrane voltage of −70 mV was changed to values ranging from −280 mV to −60 mV by means of US incident waves. The efficiency of stimulation using US was still found to be less than in the case of electrical stimulation, which requires less intensity ($1.3\,\mu\mathrm{W\,cm^{-2}}$ vs. $1.15\,\mathrm{W\,cm^{-2}}$ for US) and less energy ($1.3\,\mathrm{nJ\,cm^{-2}}$ vs. $5.0\,\mathrm{mJ\,cm^{-2}}$ for US) to activate the excitable cells [4].

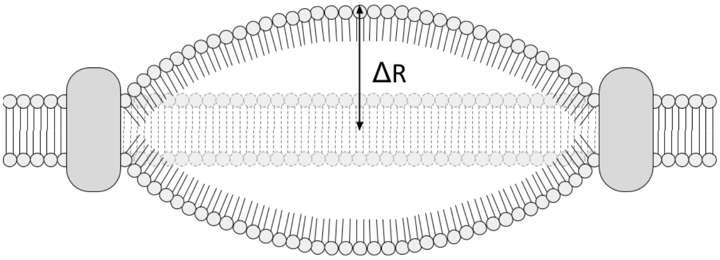

Figure 2.12: Membrane cavitation principle. The lipid layers encapsulated in a ring of proteins vibrate and generate changes in membrane capacitance.

Membrane cavitation is not the only phenomenon that could explain the variations in membrane voltage. Perforation of the lipid layer, thermal changes, the presence of stretch activated ion channels, and other forms of membrane mechanical deformation are some of the other possible explanations for the effect of US in cell activation [2]. In [2] a mathematical model for the changes in capacitance is presented as a possible explanation of the membrane response towards US. Figure 2.13 shows the cable model with the axon when the US modulates the capacitance of across the membrane.

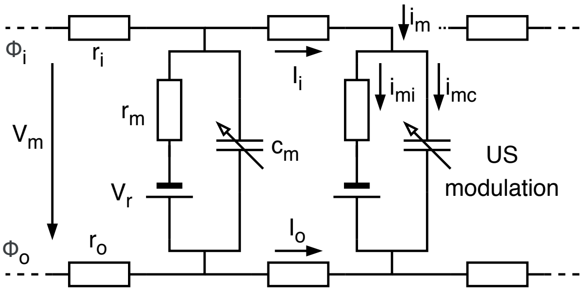

Figure 2.13: Cable model of the axon. $\Phi_{i,o}$, intracelular and extracelular electric potentials. r_i, intracelular axial resistance of axoplasm. r_o, extracelular axial resistance of extracelular medium. r_m, radial membrane resistance. c_m, membrane capacitance. $I_{i,o}$, total longitudinal intra/extracelular current. i_m, total transmembrane current. $i_{mc,mi}$, capacitive/ionic component of the transmembrane current. V_m, membrane voltage. V_R, resting membrane voltage. Model taken from [2].

Equation 2.9 still holds in this case and the membrane capacitance can be expressed as being in one of two cases $c_m \in \{c_L, c_H\}$; one of low capacitance and another one of high capacitance [2]. This equation can be further simplified to a single lumped-element model without considering spatial effects, so the distribution of charge in subs-threshold membrane potential V' from a stimulus current I_S can be expressed as:

$$V' = I_s r_m \left(1 - e^{-t/\tau}\right), \tag{2.10}$$

where $\tau = r_m c_m$. If the first phase (forward current I_f) of the biphasic pulse is delivered during periods of low capacitance and the second phase (reverse current I_r) during periods of high capacitance, then [2]:

$$\begin{aligned} I_f &= C_L \frac{dV'}{dt}\left(e^{\frac{t}{\tau}}\right) \\ I_r &= C_H \frac{dV'}{dt}\left(e^{\frac{t}{\tau}}\right) \end{aligned} \tag{2.11}$$

This imbalance of currents will accumulate charge across the membrane, which can help with membrane activation. Studies in [2] show a deviation in strength-duration curves (Figure 1.1) by 8.17 mV, 31.8 mV, and 7.40 mV with a 3 MHz sinusoidal US input delivered by a piezoelectric element driven with amplitudes of 5 V, 10 V, and 20 V respectively. The details of the experimental setup are explained in [2]. The important conclusion is that US stimulation indeed helped with the accumulation of charge across the membrane, thus modulating the electrical stimulation.

As mentioned above, the effect of US in electrical stimulation of excitable cells might be caused by different phenomena. These include thermal effects as well as non-thermal effects such as membrane capacitance oscillations like in [2], membrane cavitation like in [4, 66], or radiation force. The contribution of each of the effects are studied in [67], to clarify which one is more dominant in electrical stimulation modulation. In this study, the effects are believed to come from changes in thermosensitive and mechanosensitive ion channels [67]. The experiments were done in *C. elegans* that have very sensitive thermosensory and mechanosensory neurons. When the thermosensitivity was removed, the effect of US was the same. But when the mechanosensitive channels were removed, the US didn't have any effect. As a result, the non-thermal effects are believed to be the predominant cause of US modulation of electrical stimulation [67].

From all the above studies, it can be concluded that the mechanisms for US effects on electrical stimulation are still unclear. In general, the most plausible cause for this side effect points to changes in membrane capacitance, allowing for charge buildup, and membrane deformation, which modulates the gating of mechanosensitive voltage controled ion channels. Nevertheless, the effect is very present and it should be taken into account when designing the neurostimulator. This effect can be just acknowledged and adjusted for, or it can actually be taken as an advantage to elicit the desired cell activation with smaller electrical stimuli.

2.4. Goal of the Project & Research Questions

Based on the literature survey made in this chapter, it can be concluded that there is still a need of a wirelessly powered system that can stimulate the occipital and supraorbital nerves for the treatment of chronic headache diseases.

Said system must be implantable and miniaturized. Due to the nature of the stimulation target, different spatial patterns of stimulation, such a bipolar or tripolar, should be possible with the proposed design. They can be used to shape the electric field to target groups of cells that are topographically segregated [57]. Thus the neurostimulator should be designed in such a way that they can stimulate in modes other than standard monopolar and bipolar [57]. This also means that the system should be able to operate multiple channels.

Since the system will be powered wirelessly using an ultrasonic WPT link, CMUTs are the preferred transducers to be used at the receiver side. Given the unreliable nature of the power source of the system due to the WPT link, there is a need for a charge metering block in the design of the neurostimulator. In addition to this, the stimulation should be safe. The charge balancing block of the neurostimulator must be active and preventive instead of *a posteriori*.

3

System Design: High Level Stimulation Network

The proposed design does not aim to target all kinds of nerves responsible for headache diseases. In this particular case, the targeted application is the stimulation of the occipital and supraorbital nerves. This would be a total of six nerves to be potentially stimulated: the supraorbital nerves, the greater occipital nerves, and the lesser occipital nerves.

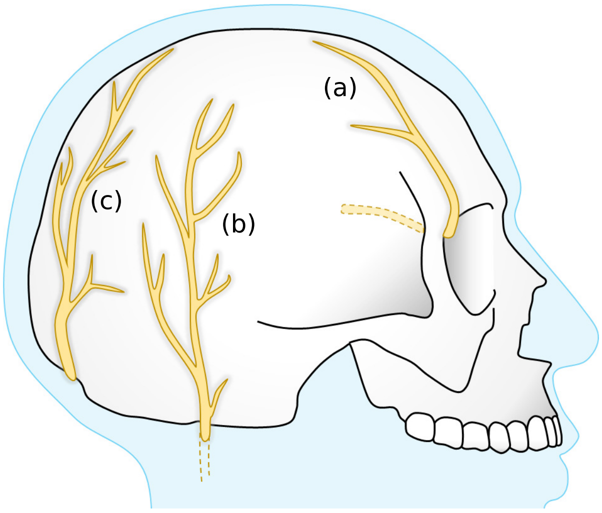

Figure 3.1: Nerves targeted with the proposed system. a) Right Supraorbital Nerve. b) Right Lesser Occipital Nerve. c) Right Greater Occipital Nerve. Similar on the left side.

As seen in Figure 3.1, all the nerves targeted with the proposed system are outside of the cranium. As a result, the implants can be implanted close to the surface of the head. The invasiveness of the implantation procedure would be less than other deep-brain implants. It has already been shown in Section 2.1 that both the lesser and greater occipital nerves can be simultaneously targeted by the same implant due to their proximity. A similar set of neurostimulators can be implemented for the supraorbital nerves. In conclusion, the placement of four neurostimulators with their respective electrode arrays is the most suitable solution for all the nerves to be targeted. This would mean two implants for the left and right supraorbital nerves, and two implants for the left and right pair of occipital nerves. An schematic of this distribution can be seen in Figure 3.2.

The size, placement, invasiveness and usability requirements specified in the concluding paragraph of Subsection 2.1.2 would be satisfied with such a system.

Regarding the reliability, power loss and the size of the implants, it would be ideal if they were powered wirelessly. This would eliminate the need for wires and bulky batteries.

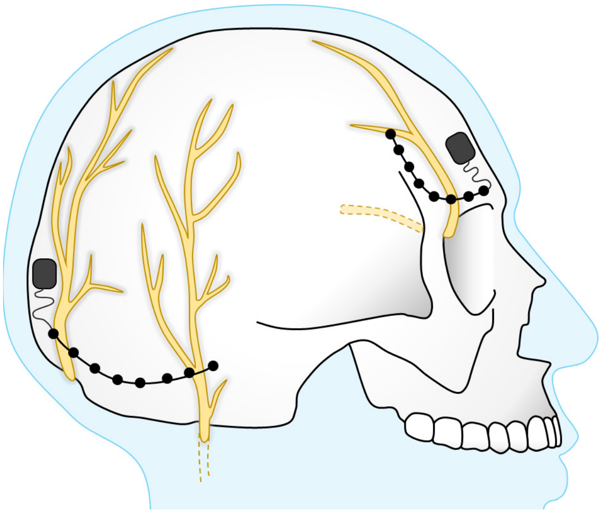

Figure 3.2: Possible location of the four neurostimulators and their respective electrodes. Two implants for the left and right supraorbital nerves, and two implants for the left and right pair of occipital nerves

In this case, the wireless powering of the implants could be made by means of ultrasonic wave propagation. The location is beneficial as the wireless link does not have to cross bone tissue, which is known to have higher acoustic impedance than soft tissues. This difference in material properties would cause a power mismatch in the power link that would significantly reduce the power transfer efficiency.

For the particular application presented here, the location of the four implants is over the skull, very close to the surface of the skin. This means that, initially, one might consider using the inductive coupling method to power each of the four implants. If the implant is miniaturized, then this method is not preferred anymore. For US, the standing wave effect might occur, and it might compromise the power efficiency, but it is still an option if the frequency can be changed to counteract this effect. In any case, both options require either a good coil alignment or a focused acoustic beam. The result of this would be the need of four transmitters for each of the four implants with neurostimulators in them. The system would have four implanted neurostimulators, four external transmitters, and four wireless power links between each of the pairs of transmitters and implants. This is depicted in Figure 3.3.a. A system with eight devices, out of which four are on the surface of the skin, is clearly not practical for the patient. Thus, a different topology is required.

3.1. Power Link between Transmitter and Implants

It has been concluded that the usage of one external transmitter for each of the implants is not practical. Therefore, there is a need for a different system that simplifies the connections between devices. The proposed solution makes usage of the conducting properties of the internal tissues in the head to connect the different implants. This solution introduces only one wireless power link between the outside and the inside of the patient. For this, an extra implant is required. the fifth implant is not a neurostimulator, but rather a receiver/transmitter that receives the power from the external transmitter, and redirects this power to the four neurostimulators implanted in the different regions of the head (Figure 3.3.b). This means, of course, that there is still a need of an external device, but the great advantage is that now the system is convenient (aesthetically and practically) to the patient. The biggest advantage of the proposed system is that it is easily scalable. For example, if there is ever the need of implanting more neurostimulators, they could just be added and no extra connections between the outside and the inside would be needed.

The power link between exterior and interior has been addressed, but there is still a need for a wireless power link between the fifth implant and the four implanted neurostimulators. For this, the proposed solution takes advantage of the acoustic conductive properties of the bone tissue. It is intuitive to think that bone might be a good acoustic conductor, since its density is higher than that of other tissues. For this link, the US WPT method would be preferred. The principle of bone acoustic conduction has been already explored for audible-range frequencies for bone anchored hearing aid (BAHA) systems [68]. These systems use a screw that is anchored (inserted) inside the skull bone and conducts acoustic waves through the skull. The waves travel through the skull into the cochlear path, thus allowing the patient to hear the vibrations [68]. The spec-

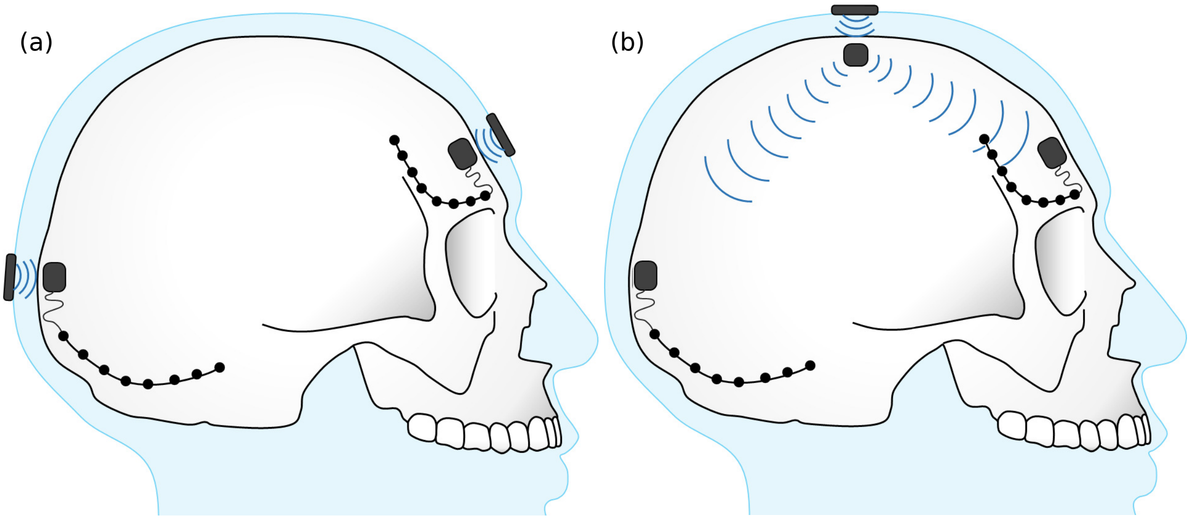

Figure 3.3: Possible Configurations for wireless power transfer. **a)** Schematic if the system when each of the implants is powered using Inductive Power Transfer (IPT), RF Power Transfer, or Acoustic Power Transfer (APT) using Ultrasound (US). This method requires n external transmitters for n implants. **b)** Schematic of the system with an additional implant, which receives the power from the outside and distributes it to the neurostimulators (rest of implants) via bone tissue. This system requites only 1 external transmitter for n+1 implants: 1 internal receiver/transmitter implant and n receivers/stimulators.

ifications of such devices do not exceed 10 kHz in general. This means that the propagation of frequencies in the desired range for our application is still unknown (hundreds of kHz to several MHz).

3.2. Bone Conduction: COMSOL Multiphysics Simulations

In order to simulate the frequency and transient behavior of the human head, COMSOL Multiphysics® was chosen as the preferred tool. In this simulation, a source of acoustic pressure was inserted in the cortical bone of the skull. The details of all the simulations are further explained below.

3.2.1. Head Model: Materials and Geometry

In order to simulate the acoustic behavior of the head, first the geometry and materials to be used have to be specified.

The geometry was designed first. For this, a sphere with six layers was defined, as shown in Figure 3.4. An external layer with perfectly matched boundaries was designed. This layer functions as a fictional infinite body of air because there are no reflections on the outermost boundary. The next five internal layers correspond to the head. For the head, first a sphere of diameter d_s was designed. The d_s diameter corresponds to the diameter of the skull. Over the skull sphere a layer of skin was designed with a thickness of th_{skin}. Thus, the skull sphere plus the skin layer make up the five layers of the head. Inside the skull sphere there are four layers. The three external layers correspond to the cortical-diploë-cortical composition of the skull bone, and the internal layer corresponds to the brain.The dura was not modeled. As explained in [34], the diploë layer inside the skull bone usually takes up to 60 % of the total thickness, regardless of the total thickness of the skull. Based on this information, the thickness of the outer and inner cortical bones was designed as one fifth of the skull thickness th_s. Of course, for the diploë layer the thickness is $0.6 \times th_s$. These relative dimensions of all the layers are graphically explained in Figure 3.4.

Regarding the numerical values of the geometric parameters, these were taken from literature. The thickness of the skull can vary between 5 mm and 10 mm [34]. The diameter of the skull varies depending on the direction in which it is measured, and also depending on the gender and age of the individual. It was determined that a range of 140 mm to 180 mm takes all these variations into consideration. Although 140 mm corresponds to the diameter from side to side and 180 mm from front to back, the geometry was still chosen to be spherical for simplicity purposes, and spheres of 140 mm and 180 mm were simulated. These spherical shapes were used assuming that going from a realistic oval shaped head to a spherical shape should not interfere much with the simulated results. The values of the geometric parameters are shown in Table 3.1.

Now that the geometry was designed, the next step was to define the material properties. For this simulation five different type of tissues were considered. From the outside to the inside of the sphere the materials

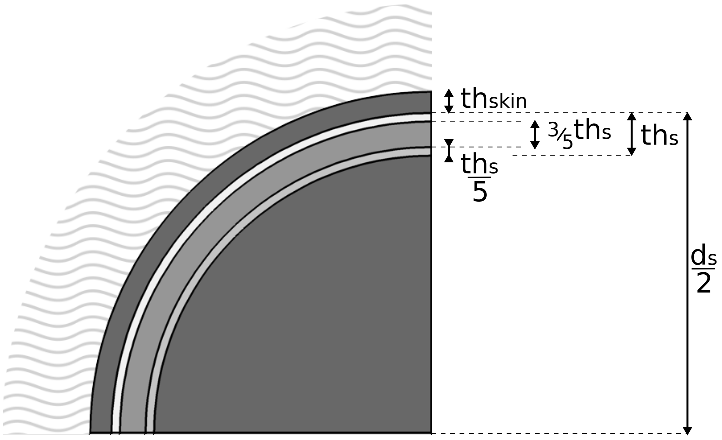

Figure 3.4: Geometry used for the COMSOL Multiphysics® simulations. d_s is the diameter of the skull, th_{skin} the thickness of the scalp, and th_s the thickness of the skull bone.

were: air, skin, cortical bone, diploë bone, cortical bone, brain. Initially, the difference between inner and outer cortical bone was to be implemented, but the differences were proven to be very small, resulting in the use of five materials for six layers. Likewise, for simplicity, the material properties used for the brain and the skin were the same in the simulation because they both correspond to soft tissue. In addition, the two materials are never in direct contact, as there is skull bone in between; so the effect of having two separate characterizations for the two materials would be minimal. In other words, similar tissues that were not in direct contact were clustered together under the same material definition. The material distribution is again explained in Figure 3.5.

Initially, three materials from the COMSOL Multiphysics® were used: Air, Bone, and Liver (human). The Air properties were unchanged, since the material in the library was already sufficient for the level of accuracy required in this paper. For the bone, there was a need to differentiate between the cortical and diploë layers. As a result, some additional parameters were adjusted and manipulated. The parameters used for the cortical and diploë bone are shown in Table 3.2. As explained above, the two cortical bone layers were considered as the same material because they are very similar and not in contact. Similarly, for the brain tissue some parameters were modified (Table 3.2) from the default Liver model in COMSOL. The parameters were changed, leading to an accurate representation of brain tissue. The skin was also characterized with the same properties as the brain (both referred as *soft tissue* in Table 3.2).

3.2.2. Frequency Analysis Simulation

The frequency behavior of the head was simulated by placing a 1 W monopole source right on the surface of the outer cortical layer of the bone. This means that the source was also in contact with the skin. The location was chosen to study both the frequency behavior of the bone, as well as that of the skin, when they are in contact with the monopole source.

The frequency range studied in this simulation was from 0.1 MHz to 10 MHz. In other words, the frequency of excitation of the monopole source was swept with said range. This frequency range was selected based on the most common operation frequencies of ultrasonic transducers used for wireless power transfer applications. Since the diameter and thickness of the head can vary among people, two additional sweeps

Table 3.1: Geometrical properties of the model used for the COMSOL Multiphysics® simulations. These properties were used for the parametric sweeps in the transient and frequency simulations. They are: thickness of the scalp th_{skin}, thickness of the skull th_s, diameter of head/skull d_h, and central frequency f_0 of the Gaussian pulse for the transient simulation

	Value 1	Value 2	Value 3	Value 4	Value 5	Value 6	Value 7	Value 8
th_{skin} [mm] [69]	5	-	-	-	-	-	-	-
th_s [mm] [34]	5	7.5	10	-	-	-	-	-
d_h [mm]	140	160	180	-	-	-	-	-
f_0 [MHz]	0.01	0.05	0.1	0.5	1	2	5	10

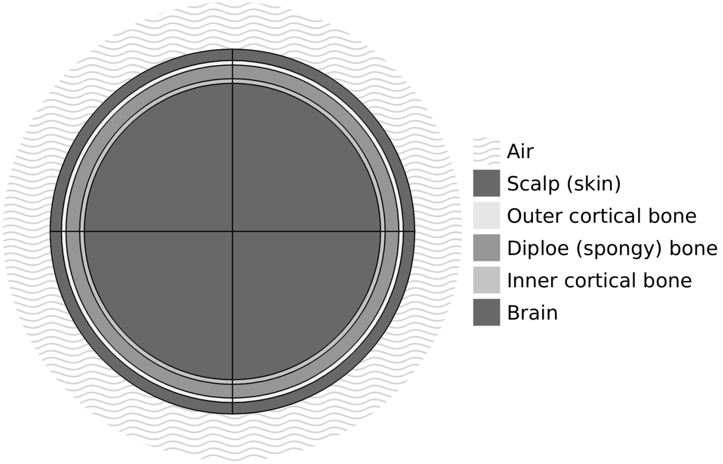

Figure 3.5: Materials used for the COMSOL Multiphysics® simulations. From the outside inwards: air, scalp, outer cortical bone, diploë bone, inner cortical bone, and brain.

Table 3.2: Physical properties of the tissues used for the COMSOL Multiphysics® simulations. They are: density ρ, Young's modulus E, Poisson's ratio ν, heat capacity C_p, thermal conductivity k, and speed of sound c. The sources from which the values were taken are also specified.

	ρ [$\mathrm{kg\,m^{-3}}$]	E [Pa]	ν	C_p [$\mathrm{J\,kg^{-1}\,K^{-1}}$]	k [$\mathrm{W\,m^{-1}\,K^{-1}}$]	c [$\mathrm{m\,s^{-1}}$]
Cortical Bone	1969 [70]	17×10^9 [64]	0.3 [64]	1313 [71]	0.32 [71]	3476 [70]
diploë Bone	1055 [70]	350×10^6 [64]	0.25 [64]	1313 [71]	0.32 [71]	1886 [70]
Soft tissue	1040 [72]	9.5×10^3 [73]	0.458 [73]	3540 [71]	0.52 [71]	1560 [72]

were made on the thickness th_s and diameter d_h of the skull and head. Finally, another sweep of angular distance d from the probes to the source was made for a fixed set of head geometry parameters.

A selection of graphs from the simulation results are presented in Figure 3.6. As a general trend, the skull is able to conduct the acoustic energy at two different bands. The first band of conduction happens at low frequencies from 0.1 MHz to 0.6 MHz, while the second conduction band occurs in the range of 1 MHz to 2 MHz. This dual band is probably due to the difference in mechanical properties between cortical and diploë bones. Although both bands conduct the acoustic energy, the difference in attenuation was still considerable at around 4 orders of magnitude. This means that at lower frequencies the intensity was at $100\,\mathrm{mW\,mm^{-2}}$, while at higher frequencies this intensity drops to around $10\,\mathrm{\mu W\,mm^{-2}}$. Finally, it can be seen that the conduction at higher frequencies is practically zero. As a result, frequencies higher than 10 MHz were not considered.

The three different dimensions for the head and skull were considered for the secondary parametric sweeps. The diameter of the head was the first secondary sweep. In reality, the shape of the human cranium is not spherical, but rather oval. The different diameters accounted for the difference in diameter within the same individual. When the diameter of the head d_h was swept, as shown in Figure 3.6.a, no significant difference was noticeable. This leads to the conclusion that the spherical representation of the head was approximate enough, as an oval would show a very similar frequency response because the diameter does not play a crucial role.

The second parameter taken into account was the angular distance of the probes with respect to the monopole source. In Figure 3.6.b it can be seen that the intensity of the acoustic signal was also independent of the location of the probe. This result is very insightful, because it implies that the location of the receiving implant does not really matter.

Finally, the last parameter being swept was the skull thickness. This parameter accounts for the differences in thickness based on gender and age. As opposed to the two previous parameters, the skull thickness th_s clearly influences the frequency behavior of the head. This can be seen in Figure 3.6.c. The thinner the skull is, the higher in frequency the secondary conduction band is. This result poses a significant concern when deciding on the operating frequency of the system, because it is not easy to find a frequency that accommodates to all skull thicknesses. Based on these findings, a frequency of 2 MHz would be a promising

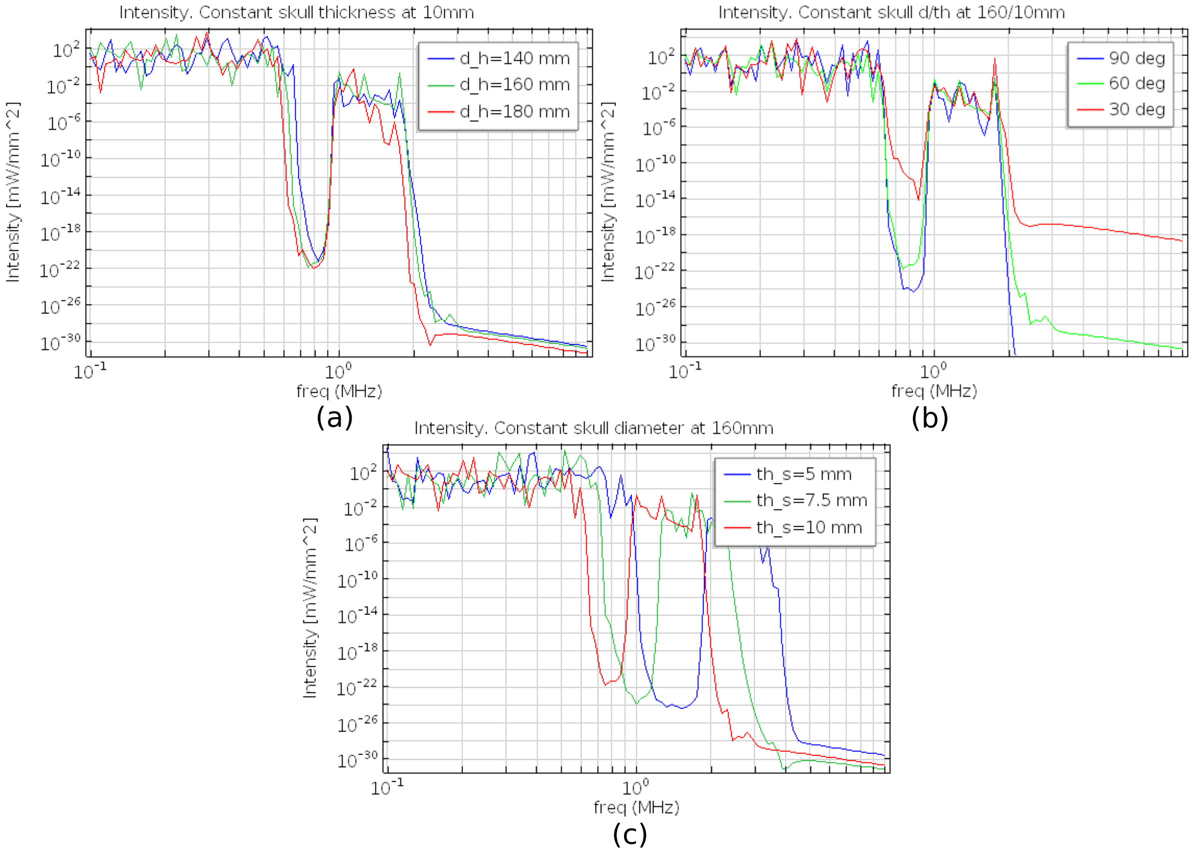

Figure 3.6: Intensity distribution comparison over frequency. **a)** constant skull thickness (th_s = 10 mm) and angular distance (d = 60°) from the source, but different head diameters h_d. **b)** constant skull thickness (th_s = 10 mm) and head diameter (h_d = 160 mm), but different angular distances from the source. **c)** constant head diameter (h_d = 160 mm) and angular distance from the source (d = 60°), but different skull thicknesses th_s.

choice. An operating frequency in the 0.1 MHz to 0.6 MHz could potentially be used, but there are reasons, which will be elaborated later on, to avoid these frequencies.

So far, all the conclusions are only applicable to the bone, which is where the measurements were taken from the simulation. But the effect of the acoustic power on other tissues should also be studied. For this, the acoustic intensity in different tissues was probed. The angular distance was kept constant across all layers for the simulation. The results of the simulations are shown in Figure 3.7.

As seen in Figure 3.7.a, the intensity is almost the same for lower frequencies (from 0.1 MHz to 0.6 MHz). Initially this is not desirable, because in the ideal case the brain of the patient should remain as isolated as possible form the input power. At higher frequencies though, ranging from 1 MHz to 2 MHz, the difference in intensity across tissues was noticeable. Figure 3.7.b displays a close up of the frequency range of interest. In this second frequency band, the intensities are still close to each other for different tissues, but it is clear that the cortical bones conduct better than other tissues. Once again this strengthens the choice for operating frequencies in this range.

So far, it has been demonstrated than the conduction over skull bone is possible at certain frequencies. But there is still a need to consider the possible constructive and destructive interference at different locations in the head. Looking at Figure 3.8, it is visible that for 1 MHz there are regions along the skull that do not receive any intensity, and other regions of high intensity. If an implant is placed on one of the white areas where there is low intensity, the power transfer might not be enough to power the implant. Fortunately, this can be solved by increasing or decreasing the frequency by small amounts. As seen in the left plot in Figure 3.8 for 1.05 MHz, the low intensity areas for 1 MHz are now areas of high intensity. This suggests that for any implantation site on the skull, there is a frequency close to the desired operating frequency in which the intensity received is highest.

In conclusion, the following can be derived from the frequency analysis. Skull bone conducts mostly in

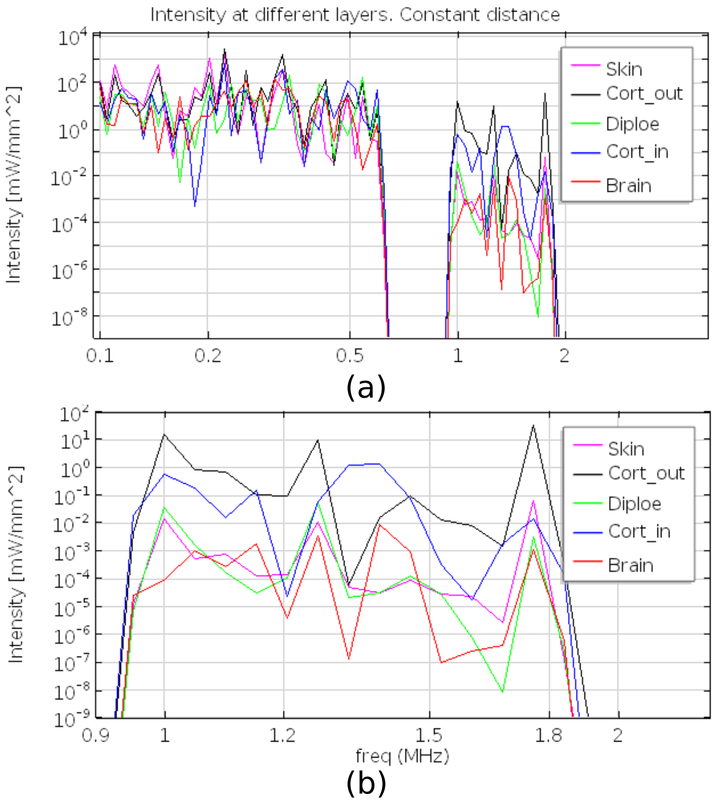

Figure 3.7: Intensity over frequency for different tissues. **a)** Intensity from 0.1 MHz to 5 MHz. At lower frequencies the intensities measured at different tissues were approximately the same. **b)** Intensity from 0.9 MHz to 2.2 MHz. It can be appreciated how the intensities at the cortical bones are measured to be higher than in other tissues.

two frequency bands, 0.1 MHz to 0.6 MHz and 1 MHz to 2 MHz. The diameter of the head does not affect bone conduction. Intensity is practically independent of the implantation site of the receiver; thus, the attenuation along the bone is almost negligible. Skull thickness affects the frequency range of the conduction band, leaving 2 MHz as the desired operating frequency since conduction is possible for a wide range of skull thicknesses. At low frequencies (0.1 MHz to 0.6 MHz) the conduction happens in all tissue layers, which is not desirable. At high frequencies (1 MHz to 2 MHz) the conduction happens mostly along the bone tissue. Finally, destructive interference can be accounted for by shifting the 2 MHz operating frequency by a few kHz.

3.2.3. Transient Time Analysis Simulation

The transient behavior of the head was simulated by placing a monopole source right on the surface of the outer cortical layer of the bone. The monopole source was Gaussian shaped with a flow rate of 1 $\mathrm{m}^3\,\mathrm{s}^{-1}$ and a bandwidth frequency of f_0. In this case the frequency f_0 was the sweep variable (sweep values are displayed in Table 3.1).

As mentioned in Subsection 3.2.2, at low frequencies, all tissues conduct acoustic waves in a similar fashion. This means that when the wave-front hits the intersection between bone and brain tissue, it is able to penetrate the brain. As a result, at $f_0 = 0.1$ MHz the acoustic wave propagates through the entire head equally, as shown in Figure 3.9.a. The lack of reflections also helps to propagate information in amplitude, as the wave does not get corrupted while traveling along the bone.

When a low frequency is used, the transfer of information is possible, as mentioned before. In Figure 3.10 it can be seen how the wave-front propagates while getting attenuated. In this case, a diameter of $d_h = 16$ cm was used in the simulation for the diameter of the head. The attenuation from 0 to 1.1 rad (equivalent to 8.8 cm traveled distance) was of 20 dB. This equates to an attenuation of 2.27 dB cm^{-1}. This value is consistent with the ones presented in Figure 2.7, but it is important to note that the attenuation is not a result of the bone properties, but rather by the fact that the input power has to distribute along the surface of the sphere. If the energy is conserved, but the wave-front gets larger and larger, it is understandable that the amplitude decreases.

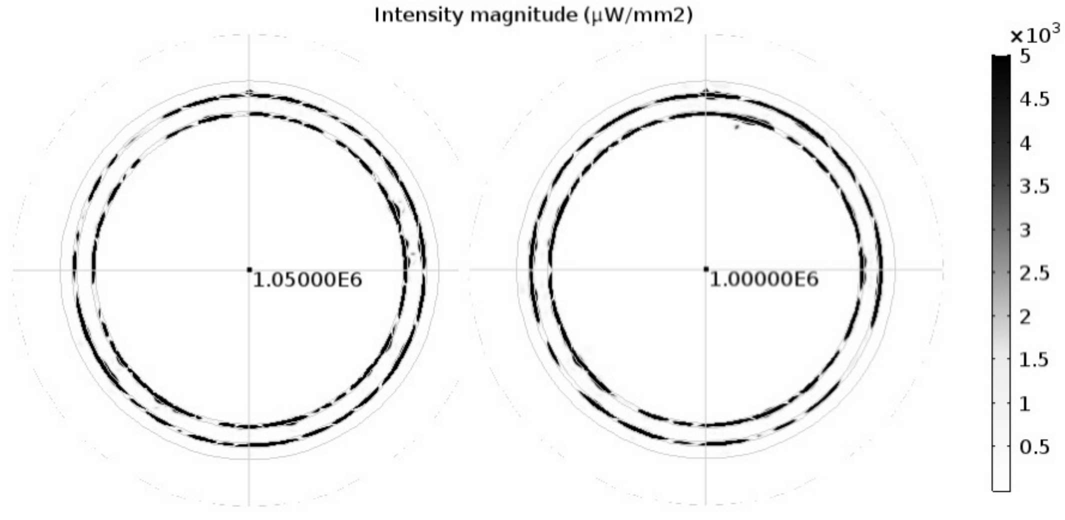

Figure 3.8: Intensity along the vertical cross-section of the head model for 1 MHz (right) and 1.05 MHz (left)

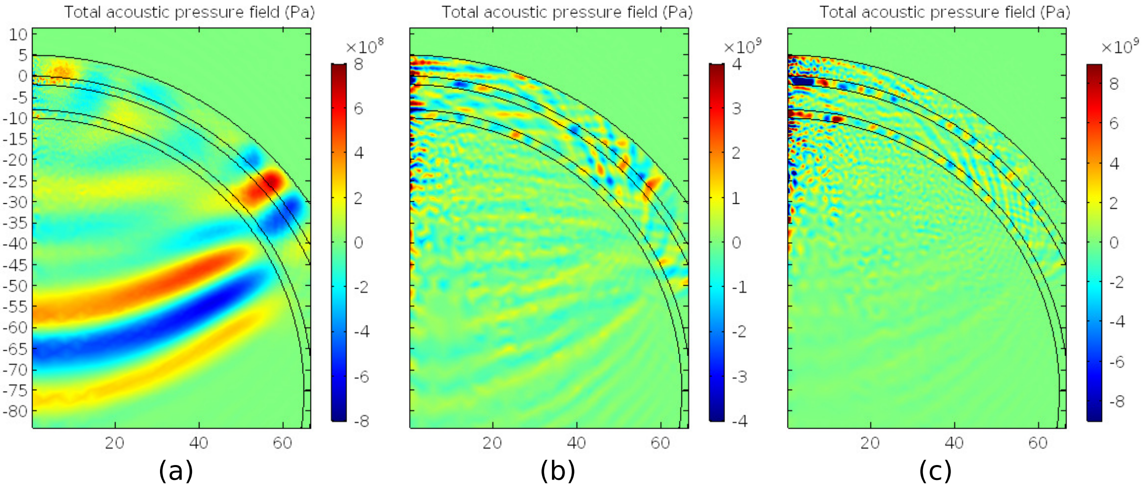

Figure 3.9: Total Acoustic Pressure at time 50 µs after a Gaussian input with flow rate $1\,\mathrm{m^3\,s^{-1}}$ and bandwidth **a)** $f_0 = 0.1\,\mathrm{MHz}$ **b)** $f_0 = 0.5\,\mathrm{MHz}$ **c)** $f_0 = 1.0\,\mathrm{MHz}$ is applied in the outer cortical bone at time 5 µs.

As the frequency increases (and as predicted by the frequency simulations) the conduction through soft tissues is less than in bone tissues. This effect can be appreciated in Figure 3.9. As a result, the reflections between media are higher, and the wave-front keeps bouncing between the internal and external surfaces of the cranium.

In Figure 3.9.b and Figure 3.9.c there are some pressure waves in the brain close to the y-axis. This was probably a result of the simulation software, and not the actual mechanical properties. The head was modeled as a flat half circle that was then rotated around a vertical axis generating the sphere. This was chosen for simulation time optimization. As a result, the areas close to the vertical axis of symmetry are not well characterized, and this might be the reason why the results are a more inconsistent in those areas.

If the reflections are multiple, the energy is still transferable, but information cannot be modulated in amplitude. Instead, if frequencies around 1 MHz are used, the information transfer would have to be modulated in frequency for example.

In Figure 3.11 three frequencies are compared for the time analysis simulation: 0.1 MHz (blue), 0.5 MHz (green), and 1.0 MHz (red). At low frequencies the reflection is small, and the Gaussian shape is maintained along propagation. At high frequencies the shape is not maintained and reflections occur everywhere. The difference in amplitudes in Figure 3.11 is due to the fact that the pulse was defined by its flow and bandwidth, thus the amplitude varies when the frequency (bandwidth) is changed. Therefore, the plot was only used to

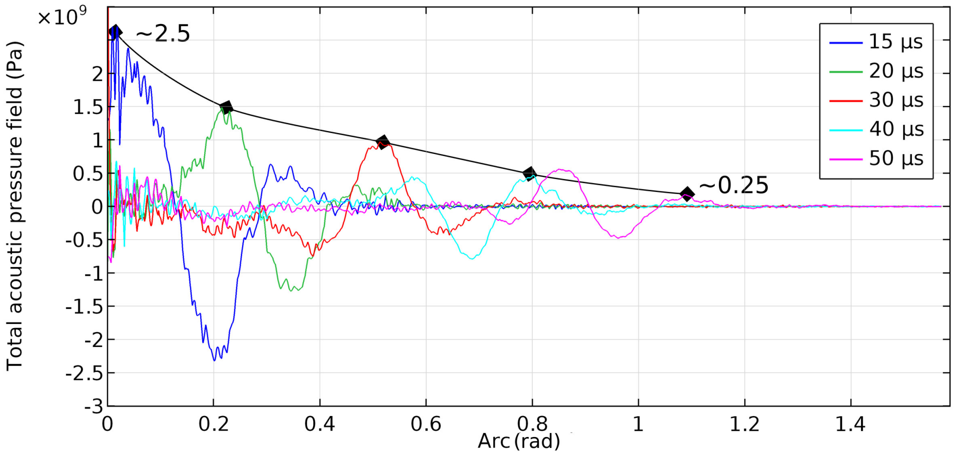

Figure 3.10: Total acoustic pressure (Pa) along the cortical bone at different times. The frequency bandwidth of the Gaussian pulse is $f_0 = 0.1\,\text{MHz}$. The attenuation of the signal along the cortical bone is around 20 dB. The horizontal axis represents the angle traveled along the cortical bone spherical surface from the source to the 90°. $d_h = 16\,\text{cm}$

study the reflections, but not their amplitudes.

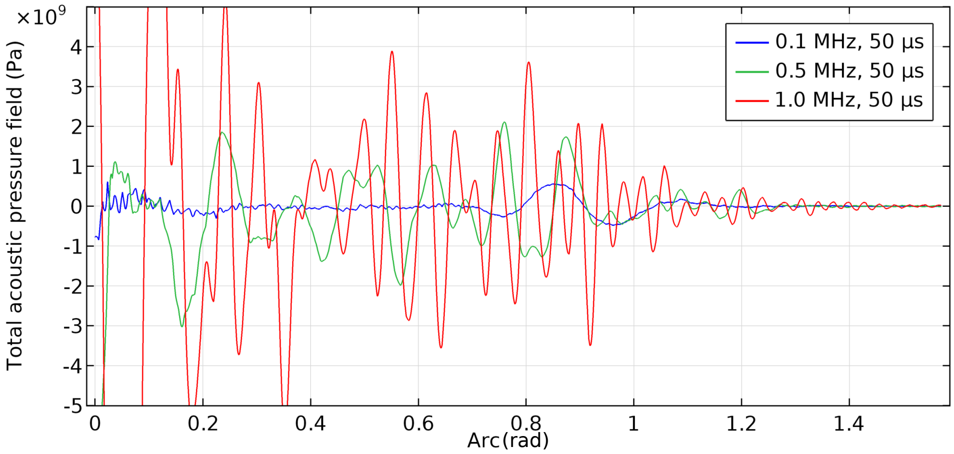

Figure 3.11: Total acoustic pressure (Pa) along the cortical bone of the skull for three different frequencies: 0.1 MHz (blue), 0.5 MHz (green), and 1.0 MHz (red). All lines correspond to time $t = 50\,\mu\text{s}$, 45 µs after the pulse was generated. The black plot tracks the source peak propagation over time. The horizontal axis represents the angle traveled along the cortical bone spherical surface from the source to the 90°. $d_h = 16\,\text{cm}$

The conclusions that can be derived from the time analysis are the following. Low frequencies around 0.1 MHz propagate well in all tissues. This is advantageous to transfer information, but not desirable because tissues like the brain get affected too. High frequencies like 1.0 MHz are preferred because they propagate mostly in bone. The drawback of high frequencies is that information cannot be modulated in amplitude. Finally, the attenuation along the bone is mostly due to geometrical factors rather than the mechanical properties of the bone.

3.3. Conclusions from Simulations

After this study of ultrasound bone conduction along the skull, the most relevant takeaways are the following.

Skull bone conducts mostly in two frequency bands, which are 0.1 MHz to 0.6 MHz and 1 MHz to 2 MHz.

The intensity is practically independent of the implantation site of the receiver as seen in Figure 3.6.b; thus, the attenuation along the bone is almost negligible. The small attenuation comes from the increase in area as the wave-front propagates along the sphere. For example, assuming that all the implants remain in the same half hemisphere of the sphere, the maximum attenuation expected is within one order of magnitude if the source is placed in the middle.

The diameter of the head does not affect bone conduction. However, skull thickness affects the frequency range of the conduction band, leaving 2 MHz as the desired operating frequency because it is included in all conduction bands for a wide range of skull thicknesses.

At low frequencies (0.1 MHz to 0.6 MHz) the conduction happens in all tissue layers, which is not desirable for safety reasons, although it is beneficial for information transfer. At high frequencies (1 MHz to 2 MHz) the conduction happens mainly along the bone tissue. At these frequencies, the waves propagate while reflecting on the bone walls. Frequency modulation could be a suitable way of transferring information in this case.

Finally, destructive interference can be accounted for by shifting the frequency by a few kHz.

4

Neurostimulator Design

As described in Chapter 3, the proposed system consists of one wireless link between a single external transmitter and an internal receiver/transmitter, and four wireless links between said implanted receiver/transmitter and the four proposed neurostimulators. Each of the neurostimulators needs to generate the desired electrical stimulus to be delivered to the target tissue via some electrodes.The connection between the neurostimulators and the electrodes was done with electrical wires. Long wires can lead to failure due to mechanical stress. For that reason, it is preferable that the electrodes and the neurostimulators are in close proximity.

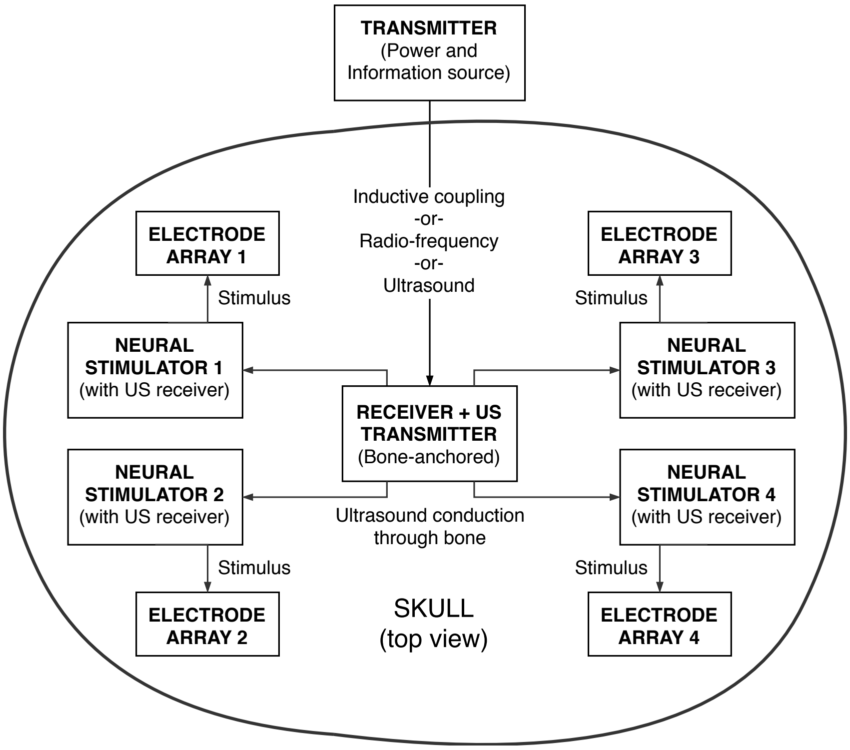

Figure 4.1: Block design of the complete system with all four neurostimulators and their respective electrode arrays

A complete view of The network system level design with all four implants is depicted in Figure 4.1. Figure 4.2 depicts the system diagram between the external power transmitter to one of the electrode arrays, as well as the environment for each of the blocks (air, skin or bone). As explained before, the link between the external transmitter and the ultrasonic power transmitter can be realized with any of the preferred WPT techniques. Next, the energy is distributed to the rest of the neurostimulators using the bone as a conductor.

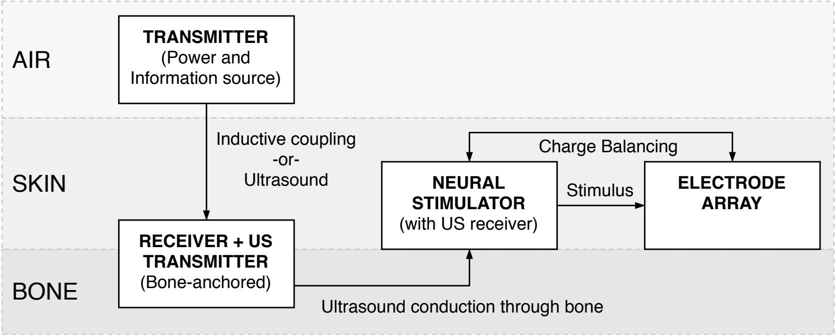

Figure 4.2: Block design of the link between the external transmitter and the electrode array of each of the neurostimulators

4.1. Neurostimulator System Level Design

4.1.1. Requirements

The overall power path of the system is presented in Figure 4.3. P_1 refers to the power link between the outside and the anchored device on the skull. This link is not within the scope of the project; it could be realized in different ways using inductive links, RF or Ultrasonic wireless power transfer. P_{US} refers to the ultrasonic power link described in Chapter 3. The limits for US power in the body for diagnosis have been set by the FDA to a value of $P_{US,TX} = 7.2\,\mathrm{mW/mm^2}$ [74]. The US attenuation along the skull was of 20 dB, as concluded in Chapter 3. This attenuation can be translated to a power transfer efficiency of $\eta_{skull} = 1\%$. Consequently, the maximum energy that reaches the neural stimulator is $P_{US,RX} = 7.2\,\mathrm{mW/cm^2}$.

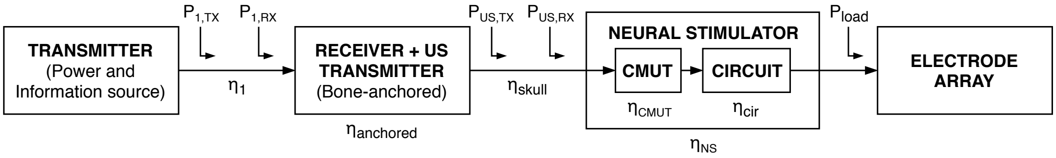

Figure 4.3: Power path of the complete system

Power requirements for standard implant operation are in the order of 10 mW to 20 mW [38–40]. This consumption would correspond to a receiver area of $2.78\,\mathrm{cm^2}$ (1.67 cm × 1.67 cm). As a consequence, the power consumption of the implant must be reduced considerably in order to allow its miniaturization.

In the following proposed design, most of the power received is delivered to the tissue, thus the power limitations are set by the power consumption during the stimulation phases. For the specific application of this work, the power requirements are around 11 mW. This value was estimated from stimulation patterns of already available neurostimulators for chronic headaches, as shown in Table 4.1. This estimate is consistent with measured power consumption (10 mW to 20 mW) of the output stage in other systems for different applications [38–40].

Table 4.1: Stimulation parameters from occipital nerve stimulation used in different devices and studies [75]

	Literature				Calculations Assuming $R_L = 10\,\mathrm{k\Omega}$	
Study	Voltage (V)	Duration (µs)	Freq (Hz)	Period (ms)	Current (µA)	Power (µW)
1	3.2	400	55	18	320	1024
2	1.5-10.5	90-180	90-180	6-11	150-1050	225-11025
3	0.1-6.7	240-450	25-60	17-40	10-670	1-4489
3 Avg	2.6	399	38	26	260	676
4	0-10.5	60-450	3-130	8-333	0-1050	0-11025
5 Avg	6.36	364	66	15	636	4045
5	2.4-10	40-100	270-450	2-4	240-1000	576-10000
6	0.3-3.15	450	60-130	8-17	30-315	9-992
Range:	0-10.5	40-450	3-180	2-333	0-1050	0-11025

CMUTs with power transfer efficiencies of $\eta_{CMUT} = 70-80\%$ have been reported in literature ([30]), which leave around $5.76\,\mathrm{mW/cm^2}$ of usable power. Assuming $\eta_{cir} \approx 100\%$ (because the US frequency can be used "directly" to stimulate) and $P_{load} = 11\,\mathrm{mW}$, the area of the CMUT should be $A = 1.9\,\mathrm{cm^2}$. Assuming that the CMUTs are round, this area translates to $\varnothing = 1.56\,\mathrm{cm}$.

The above calculations highlight how critical the size to power trade-off is. A diameter of $\varnothing = 1.56\,\mathrm{cm}$ is too big for the next generation of neurostimulators. Nevertheless, if the electrodes are also optimized for the specific application and their proximity to the target tissue is improved, the power requirements of the neurostimulator might be relaxed. This reduced power consumption might allow smaller CMUT sizes.

Furthermore, the FDA limitation for ultrasounds in the body ($7.2\,\mathrm{mW/mm^2}$) was specifically defined for imaging, or for high intensity focused ultrasound devices [12]. If the operation is with continuous waves, there are no limitations specified [12]. In addition to this, the limitations are specific to some types of tissue, like vessels. Different tissues might have different ultrasound intensity limitations [12]. One different way of evaluating the safety is the mechanical index (MI), which relates to the cavitation effect that might occur in case the amplitude of the wave is too high [12]:

$$\mathrm{MI} = \frac{p_n}{\sqrt{f_\mathrm{c}}} \tag{4.1}$$

The FDA limits the MI to 1.9 [12]. Given a frequency of 2 MHz, the maximum amplitude that would be admissible is $p_n = 1.9 \cdot \sqrt{2} = 2.69\,\mathrm{MPa}$. If this is applied to cortical bone, the intensity would be:

$$I = \frac{p_n^2}{\rho \cdot c} = \frac{2.69\,\mathrm{MPa}^2}{1969\,\mathrm{kg/m^3} \times 3476\,\mathrm{m/s}} = 1.05\,\mathrm{MW/m^2} = 1.05\,\mathrm{W/mm^2}$$

This high value for the power limit is also consistent with Figure 3.7.b in the following way. If brain damage is considered as the limiting factor, when the $7.2\,\mathrm{mW/mm^2}$ requirement is applied to brain tissue, the requirement for cortical bone would be around three to four orders of magnitude higher, due to the fact that at 2 MHz the acoustic energy propagates mostly in bone tissue and not in the other soft tissues (Figure 3.7.b). This gives a power limit of $\approx 10\,\mathrm{W/mm^2}$ for the cortical bone. This value is consistent with the MI limits.

In conclusion, the power availability is not the main limiting factor for the size of the neurostimulator, if these alternative safety limits for ultrasound are applied instead.

4.1.2. Block Diagram

The proposed block diagram of the neurostimulator is shown in Figure 4.4. The principal blocks of the system are the following:

- An ultrasonic transducer that receives the incident incoming acoustic waves and translates them into the electrical domain.
- A power conditioning block that takes the incoming electrical power from the ultrasonic transducer and shapes it to be used at the output stage.
- The output stage takes the incoming conditioned power and delivers it to the electrodes in accordance to the desired stimulation pattern.
- A charge balancing block guarantees stimulation safety by ensuring zero residual charge at the electrodes, as explained in Subsection 2.2.3.
- A charge metering block to ensure efficacy as explained in Subsection 2.2.4.
- A digital unit, which is in charge of the control of the output stage, charge metering and charge balancing blocks.
- A small power storage unit for the powers supply for the digital circuit.
- A data demodulator from the output of the ultrasonic transducer.
- And a clock generator or extractor for the correct operation of the digital unit.

For the ultrasonic transducer, a CMUT was chosen. If the CMUT is pre-collapsed or pre-charged, then there is no need for a high DC voltage withing the neurostimulator. For the power conditioning a simple full wave rectifier was used. The small power storage unit, data demodulator, clock generator and the digital unit designs were not within the scope of this project. Instead, the focus was put on the charge metering, charge balancing and the output stage of the neurostimulator.

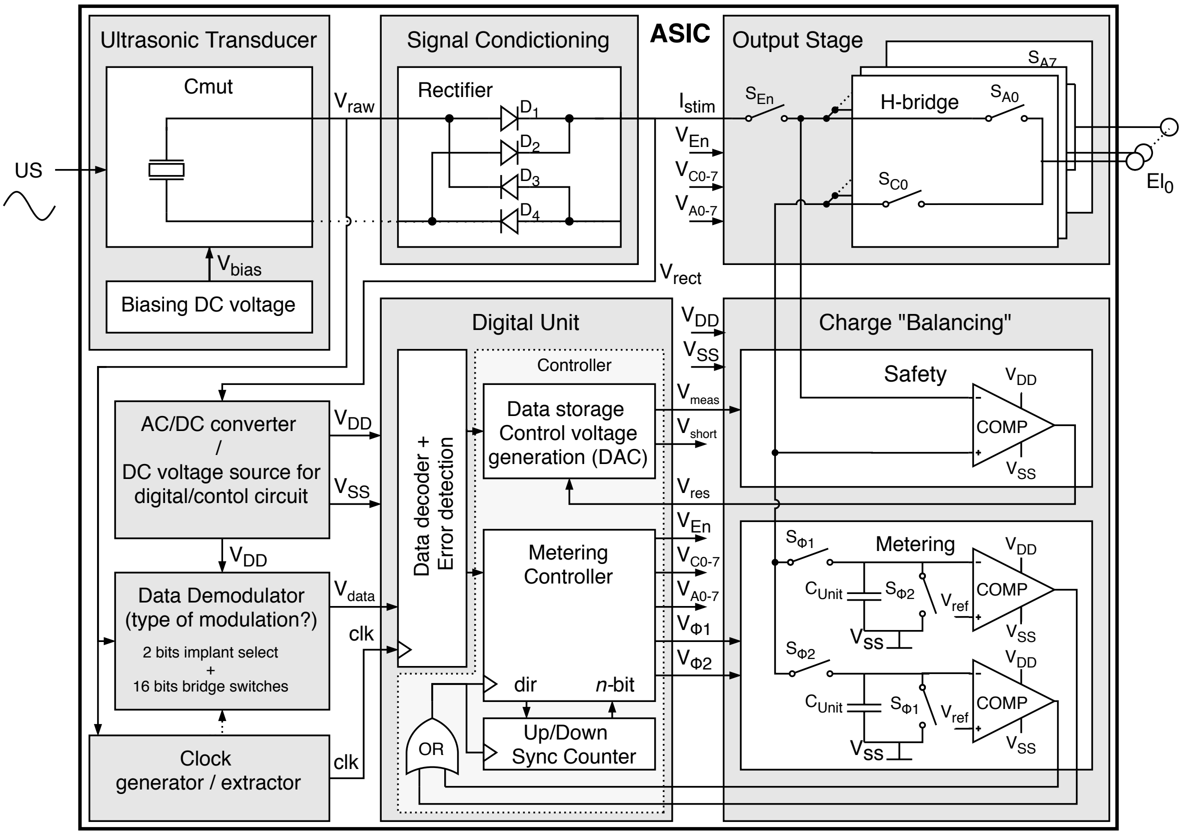

Figure 4.4: Block diagram of the proposed implantable neurostimulator.

The specific circuit designs of each of the blocks within the scope of the project are explained in the following section.

4.2. Neurostimulator Circuit Design

Regarding the output stage, an H-bridge configuration was chosen as it allows to stimulate with both polarities while using one single power source. For example, in a biphasic stimulation pulse, the use of the H-bridge allows to generate the two stimulation phases: cathodic and anodic. The H-bridge is also particularly useful for multichannel configurations, as it can be used to select channels too.

Although the specific application only requires the stimulation of one nerve per implant, a multichannel configuration might be useful. This ensures that, regardless of the implantation site accuracy, there will always be a channel that's close enough to the stimulation target. In addition, spatial patterns of stimulation could be used to increase specificity and the spatial resolution of the stimulation. This is achieved by using bipolar or multipolar configurations, which shape the electric field [57]. Furthermore, new developments to increase efficacy in pain suppression treatments point at stimulation patterns in which the different poles are stimulated in a sequential manner to emulate skin caressing in an electronic form, also know as *pleasure stimulation* [76]. Thus the neurostimulator should be designed in such a way that it can stimulate in modes other than standard monopolar and bipolar [57]. For this purpose, a multichannel configuration of the output stage was considered.

4.2.1. Activation Efficacy: Charge Metering Circuitry

In order to measure the charge being delivered to the tissue during stimulation, a design similar to the one presented in [54] was used. The topology can be observed in Figure 4.5.a. The difference lays in the operation of such topology. Instead of using the circuit to match the cathodic and the anodic phases, here it is being used to match the cathodic phases of consecutive stimulation pulses. This ensures that the charge delivered to the tissue is always the same. From Figure 1.1 it can be seen that for longer stimulation periods, more charge might be required. This effect is associated to the charge dispersion in the membrane vicinity, as well as Faradaic reactions. This means that for different power supply levels, the charge metering circuit might take longer or shorter to deliver the programmed amount of charge, and the actual required amount of charge my differ from the said programmed one. Nevertheless, the charge metering circuitry was designed to compensate for small variations of the power supply, so this effect should not be critical to the design. In other words, it is safe to assume that same amounts of charge will elicit a similar response in the target tissue even when the supply varies by small amounts.

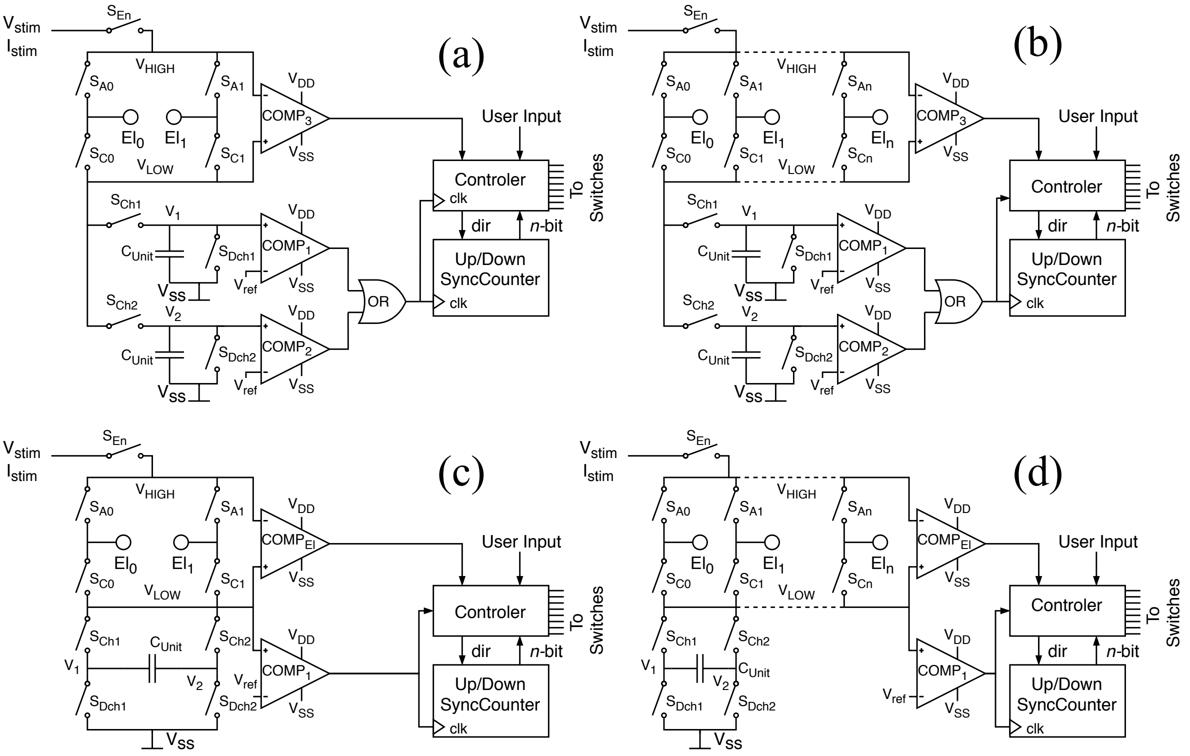

Figure 4.5: Output stage of the neurostimulator. **a)** Initial design. **b)** Initial design with a multichannel configuration. **c)** Improved design. **d)** Improved design with a multichannel configuration.

The operation of the charge metering circuit shown in Figure 4.5.a is as follows. During the cathodic phase the H-bridge switches are used to steer the incoming charge in the correct direction. This means that S_{En}, S_{A1}, and S_{C0} are closed. Since electrode El_0 is driven negative, the cathodic stimulation will happen there. During the cathodic phase, there are two branches with capacitors C_{unit} in series that are use to directly measure the charge. These two branches alternate to charge and discharge some unit capacitors $C_{unit_{1,2}}$. A counter tracks the number of times these unit capacitors are being charged to a specific value, thus measuring the total charge being delivered to the load.

The detailed operation of the circuitry is the following. First, the first branch (S_{Ch1}, S_{Dch1}, C_{unit_1} and $COMP_1$) is connected by closing switch S_{Ch1} while leaving S_{Dch1} and S_{Ch2} open. C_{unit_1} is then charged through S_{Ch1} while the stimulation is going on. When the voltage across C_{unit_1} reaches a predetermined value determined by V_{ref}, comparator $COMP_1$ generates a trigger signal that is being registered in the counter. The charge corresponding to that count is determined by the following equation:

$$Q_{unit} = C_{unit} \times V_{ref} \tag{4.2}$$

The output trigger of $COMP_1$ is also being used to change the control of the state of the switches. Now,

S_{Ch1} opens and S_{Dch1} closes allowing C_{unit_1} to discharge. At the same time, S_{Dch2} opens and S_{Ch2} closes, which allows the stimulation to continue while charging C_{unit_2} through S_{Ch2}. Similarly to the previous time, when C_{unit_2} is charged to V_{ref}, a trigger is generated from $COMP_2$. That trigger is then sent to the counter and to the switch control unit. The alternation of the two branches keeps going until the desired count is reached at the counter. The total charge being delivered to the tissue is then calculated using Equation 4.3, where N represents the number of counts. This is assuming that V_{ref} is constant with no variations and that C_{unit} is linear. The operation of the charge metering during the cathodic phase can be observed in more detail in the blue shaded areas in Figure 4.6.

$$Q_{total} = N \times C_{unit} \times V_{ref} \tag{4.3}$$

From Equation 4.3 it can be deduced that there is a trade-off between the number of counts N, V_{ref} and C_{unit}. In an IC implementation it is desirable to reduce C_{unit} as much as possible in order to minimize area and improve on charge metering resolution. In a standard 0.18 μm CMOS technology, the area for integrated capacitors is around 12 fF/μm^2 or 1 fF/μm^2 to 4 fF/μm^2 if metal-insulator-metal (MIM) capacitors are allowed [77]. Similarly to C_{unit}, in an ideal IC, V_{ref} would also be reduced to conform with the supply headroom and to improve the resolution. In practice, having small C_{unit} and V_{ref} require more counter bits (more counts) as well as a higher operation speed, since the branches would be switching very fast. All these have to be taken into consideration when designing for this part of the neurostimulator circuit.

An improved design is also proposed in this work. To the author's knowledge this is a novel design that uses the same control switches as the one explained above. The main difference is that instead of having two parallel branches with a $C_{unit_{1,2}}$ capacitor per branch, it connects a single C_{unit} capacitor from the V_1 node between S_{Ch1} and S_{Dch1} to the V_2 node between S_{Ch2} and S_{Dch2}. This can be seen in Figure 4.5.c. This way, the unit capacitor is being charged with opposite polarities during each count. The operation of the switches remains the same. The advantage of this new design does not only rely on the use of one capacitor, but it also allows to get rid off one of the comparators by measuring the voltage across C_{unit} from the V_{LOW} node. As demonstrated later on in the results section, the operation of this improved topology is comparable to the one presented in [54].

As explained in Chapter 2, this charge metering has several advantages over other topologies. Firstly, since the C_{unit} capacitors are in series with the stimulation load, the topology is making a direct measurement of the charge. Secondly, because the C_{unit} capacitors are small in size, the topology is easy to implement into an IC. Thirdly, this topology does not require a separate charge metering circuit per channel. Instead, it utilizes the switches in the H-bridge to select which channel is being measured. Finally, it uses comparators instead of amplifiers to measure the voltage across the unit capacitors. These comparators already function as single-bit ADCs (by definition) and they are easily scalable with the circuit.

Finally, multichannel operation becomes also possible thanks to this topology. Every time a count is triggered, the H-bridge can switch the configuration to stimulate another channel. Individual packages of $C_{unit} \times V_{ref}$ charge can be distributed in an orderly fashion across multiple channels to build up charge simultaneously. This provides a way of complying with different charge demands for each channel. The only disadvantage of this operation is that it would require to keep track of the counts for each for the channels independently. The multichannel operation of the system was kept in mind during the design process, but it was not further explored during Chapter 5.

4.2.2. Safety: Charge Balancing Circuitry

As mentioned in Subsection 2.2.3, the best approach to charge balancing is to actively monitor the charge accumulation at the electrode tissue interface. A dynamic offset regulation approach is optimal as it compensates for the charge *a priori* and it stops the second phase of the stimulation pulse right when there is no more charge accumulation at the double layer capacitance C_{dl}.

The challenge with measuring the capacitance across the electrodes during stimulation is that there is a voltage drop coming from the resistive behavior of the tissue in between, R_S. In other words, in order to measure an accurate indication of the $V_{V_{dl}}$, there stimulation must not be active so that there is no voltage drop across the tissue. Fortunately, the charge metering circuitry is already present in the system. This is of interest because, during the charge metering operation the stimulation is stopped briefly to change between branches, or to flip the capacitor orientation in the improved design. This small windows in-between the stimulation can be used to measure the voltage across the electrodes. The voltage is being measured across nodes V_{HIGH} and V_{LOW}, which also allows for the adaptation to a multichannel configuration as seen in

Figure 4.5.b and Figure 4.5.d. This is because $COMP_3$ and $COMP_{el}$ can be connected to any pair of electrodes simply by using the H-bridge switches, $S_{A1\rightarrow An}$ and $S_{C1\rightarrow Cn}$.

The topology for charge balancing operates as follows. When the second phase is initiated, the direction of the counter reverses. Because in the first half of the anodic phase the voltage across the electrodes is still far from zero, the charge metering operates for half of the counts without any charge balancing measurement. Once half of the counts have been recorded, the charge balancing phase starts. Every time one of the two branches triggers a count, the stimulation is paused and the output of $COMP_3$ or $COMP_{El}$ (for the improved topology) is measured. Once the voltage across the electrodes crosses the zero line, the stimulation is stopped and a shorting phase follows for the entirety of the interpulse delay. The shorting phase closes switches $S_{A0,A1}$, $S_{C0,C1}$, $S_{Ch1,2}$ and $S_{Dch1,2}$.

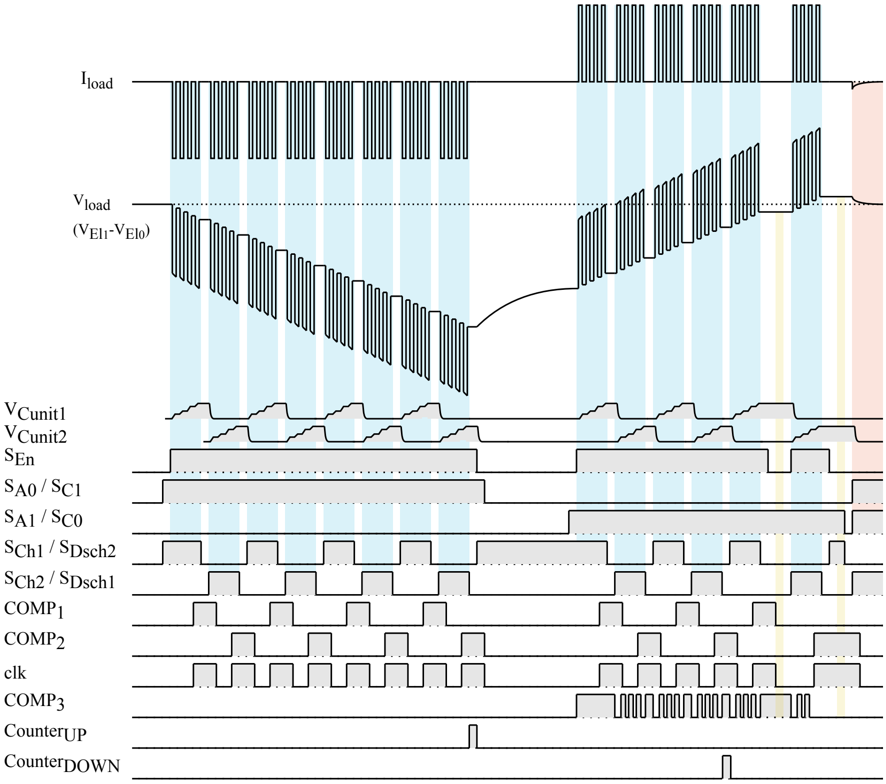

Figure 4.6: Time diagram of the charge metering and charge balancing operation during a biphasic stimulation pulse.

The complete timing operation of the charge balancing and charge metering circuits can be seen in Figure 4.6. Plots V_{Cunit1} and V_{Cunit2} show the voltage across the unit capacitors. Plots S_{En}, $S_{A0,C1}$, $S_{C1,C0}$, $S_{Ch1,Dsch2}$, and $S_{Ch2,Dsch1}$ represent the control signals for the switches, where *HIGH* means closed and *LOW* means opened. Plots $COMP_{1,2,3}$ show the digital output of the comparators. The inputs in $COMP_3$ are connected to nodes V_{HIGH} and V_{LOW} (Figure 4.5). As a result, the output of $COMP_3$ is *HIGH* when $V_{load} > 0$ and *LOW* when $V_{load} < 0$ during the cathodic phase, but it is *LOW* when $V_{load} > 0$ and *HIGH* when $V_{load} < 0$ during the anodic phase. Plots clk, $Counter_{UP}$ and $Counter_{DOWN}$ show the digital control signals for the counter. The interphase delay between the anodic and cathodic phases shows an exponential decrease in magnitude of V_{Cel} due to Faradaic reactions. The blue bands correspond to each individual charging period for a unit capacitor C_{unit}. The yellow bands show the instances during the anodic phase when stimulation is stopped to measure the voltage across the electrodes, by means of reading the output of $COMP_3$. The red band shows the shorting phase. The high frequency pulses in the I_{load} and V_{load} plots represent the UHF pulses.

Similarly to the charge metering, the charge balancing circuitry has several advantages over other topologies. Again, this topology does not require a separate charge balancing circuit per channel. Instead, it utilizes the switches in the H-bridge to select which channel is being measured. Just like for the charge metering, the comparator already functions as ADC and it is easily scalable with the circuit.

4.3. Prototype design

Once the topology was validated, a printed circuit board (PCB) prototype was devised using discrete components. A diagram with the implementation of such prototype circuitry can be found in **Figure 4.7**.

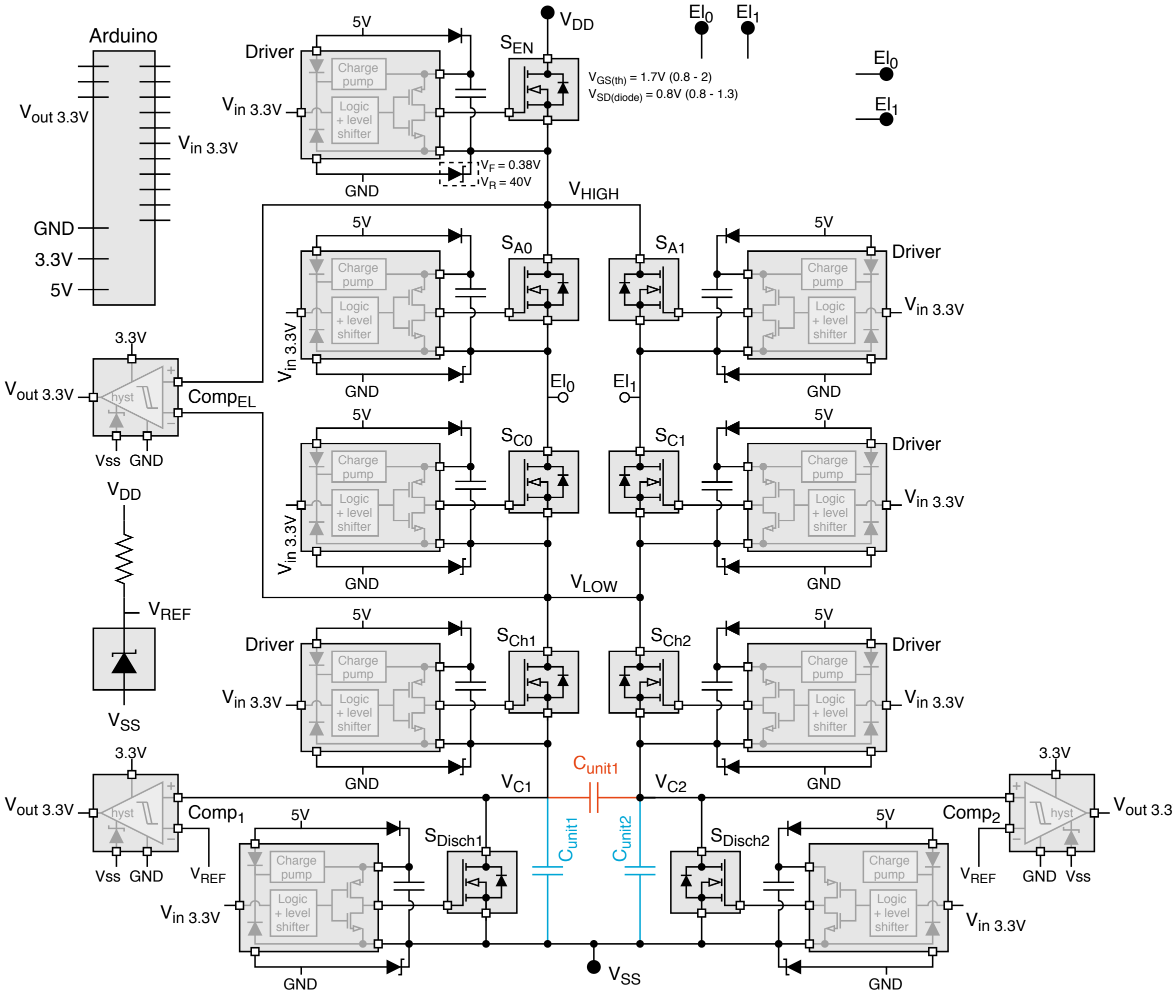

Figure 4.7: PCB diagram with the two proposed topologies: initial topology in black and blue, and improved topology in black and red.

In the PCB implementation (diagram in **Figure 4.7**), the unit capacitors C_{unit} were not soldered to the board. Instead, pins at nodes V_C1, V_C2 and V_{SS} were placed as access points. This allowed the interchange of different C_{unit} with different capacitances, as well as the change between the original and improved charge metering topologies. In **Figure 4.7**), the configuration with the two blue capacitors corresponds to the circuit in **Figure 4.5.a.** Oh the other hand the topology with the single unit capacitor C_{unit} in red is a hybrid between **Figure 4.5.a.** and **Figure 4.5.b.** because a single unit capacitor is being used, but there are still two comparators $COMP_1$ and $COMP_2$ connected to V_C1 and V_C2 respectively, instead of connecting a single comparator to V_{LOW} for the charge metering (the ideal improved topology).

The most critical part of the design was the trade-off between number of counts N, V_{ref} and C_{unit}. In order to choose said values, the total charge needed for activation was calculated. Based on **Table 4.1**, the stimulation charged needed for the treatment of chronic headache diseases is not greater than 500 nC. Thus, this value was taken into consideration as the worst case scenario in which the charge needed for activation is the highest.

For simplicity of the design, an *Arduino MKR Zero* board was used for the generation of the control signals of the prototype. This particular board was chosen because it contains a 16-bit counter and runs at a 20 MHz clock. This translates to a minimum delay of $t_{min} = 50$ ns and a total number of counts of $N_{tot} = 65536$. For the reference voltage, the *LTC1389* from *Linear Technology* with a $V_{ref} = 1.25$ V was selected also for simplicity. It was assumed that the comparators will trigger whenever the voltage across the unit capacitor, C_{unit}, reaches $V_{ref} = 1.25\,\mathrm{V}$. Based on the assumption, and using Equation 4.3, the minimum capacitance required for the correct operation of the system would be:

$$C_{Unit_{min}} = \frac{Q_{tot}}{N_{tot} \times V_{ref}} = \frac{500\,\mathrm{nC}}{65\,536 \times 1.25\,\mathrm{V}} = 6.10\,\mathrm{pF}$$

As a reminder of the area consumption of such a capacitance in an IC, an implementation of 6.10 pF into a standard 0.18µm CMOS technology would require an area of ~0.05 mm^2 to ~0.61 mm^2.

For the implementation of the switches, nMOS transistors were chosen. The *BSS123* from *On Semiconductor*® was selected based on the low gate charge $Q_G = 1.4\,\mathrm{nC}$, low on resistance $R_{on} = 6\,\Omega$ and high drain-source voltage compliance $V_{DS} = 100\,\mathrm{V}$. Since these transistors are stacked up along the stimulation path, *LTC7004* gate drivers from *Linear technology* were used to operate them. These gate drivers are controlled with a digital input. When the input is low, the gate is connected to the source directly, keeping the transistor off. When the input is high, the driver places a charged capacitor between source and gate, which pushes V_{GS} over the threshold turning the transistor on. For the rectifier, *RB706D-40* shottky diodes from *Rohm Semiconductor* were used because they offer a lower voltage drop than regular diodes. Finally, the comparators were implemented with the *LTC1440* ICs from *Linear technology* and their builtin hysteresis $V_{hys} = 50\,\mathrm{mV}$. The PCB prototype with all the discrete components of the design can be seen in Figure 4.8.

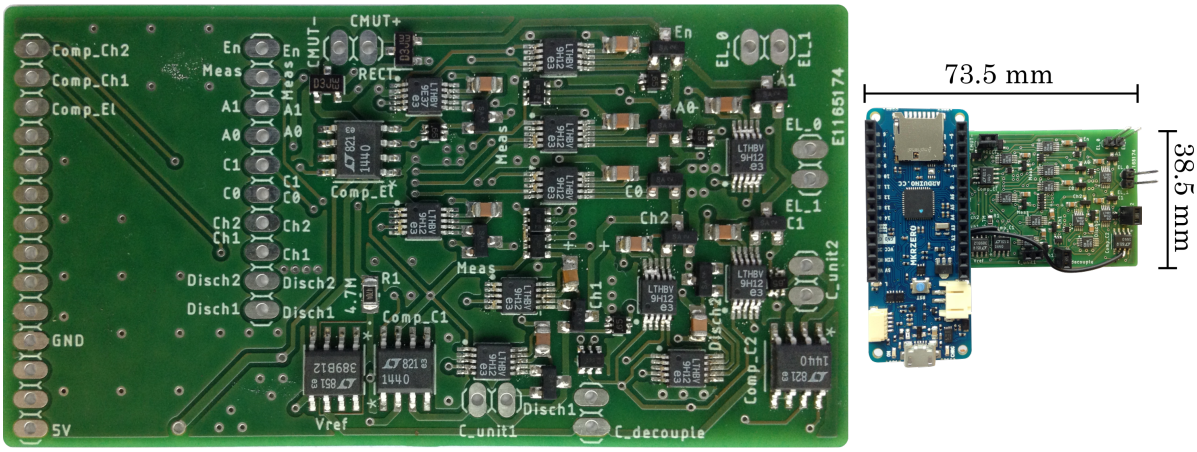

Figure 4.8: PCB with soldered components (left). PCB together with the *Arduino MKR Zero* board (right).

For the correct operation of the circuits,it is required that at all times no short between V_{LOW} and V_{SS} happens. This is because if one of the electrodes is connected to V_{SS} (e.g. S_{Ch1} and S_{Dch1} opened), the stimulation charge would flow directly to ground without being measured, and the charge metering topology would not perform accurately. Another critical situation is the shorting phase where all switches are closed while the enabling switch S_{En} is opened. If S_{En} takes longer to open, there could be a situation where the supply V_{DD} is directly connected to ground V_{SS}. For that purpose, operation of the charging and discharging switches (or any other switch) cannot be considered simultaneous, as process variation during their fabrication might make the switches slower or faster with respect to each other. One way of making sure that the discharging switch is not closed while the charging switch still is, is to sense the opening of the charging switch and generate a signal that closes the discharging switch. For this, a sensing element or technique would be required, adding complexity, power consumption, etc. to the system. Another approach is to introduce a delay between the two control actions.

Implementing the delay with the Arduino creates another problem. After some preliminary testings of the speed of the Arduino, it was found that the minimum delay between command lines was around 200 ns to 300 ns. The stimulation happens in the order of magnitude of 100 µs and, if 65536 counts are used, the amount of lost time with no stimulation would be:

$$t_{loss} = t_{min} \times N_{tot} = 300\,\mathrm{ns} \times 65\,536 = 19.66\,\mathrm{ms}$$

This time being lost throughout stimulation is not practical. The number of counts should be reduced by a factor of 10^3 or 10^4 in order to get a time loss of 1.98 µs to 19.8 µs. This places the number of counts at $N \approx 60$

Finally, it is interesting to compute how long it takes for the device to charge the unit capacitor C_{unit}. The time constant for the charging of the unit capacitor can be computed as follows:

$$\tau = (R_S + R_{on}) \times (2 \times C_{dl}^{-1} + C_{unit}^{-1})^{-1} \tag{4.4}$$

Where R_S is the tissue impedance in the order of 10 kΩ [37], C_{dl} is the electrode-tissue double layer capacitance in the order of 10 nF to 100 nF [37], R_{on} is the sum of the on-resistances of the S_{En}, $S_{A_{0,1}}$, $S_{C_{0,1}}$, and $S_{Ch1,2}$ transistors, and C_{unit} is the unit capacitance being charged. C_{dl} is multiplied by two because there are two double layer capacitances in series in the tissue circuit model, one per electrode. Considering that the on-resistances of the switches are negligible in comparison to the tissue impedance, and that the unit capacitor is much smaller than the electrode-tissue double layer capacitance, the time constant can be approximated to:

$$\tau = R_S \times C_{Unit} \tag{4.5}$$

For example, using $R_S = 10\,\text{k}\Omega$ and the calculated value for the smallest C_{unit}, a time constant of around 122.1 ns can be obtained. In addition to this, the time that it takes for the unit capacitor to charge can be calculated with the following equation:

$$t_{charge} = -\ln\left(1 - \frac{V_{ref}}{V_{DD}}\right) \times \tau_{C_{unit}} \tag{4.6}$$

If, for example, $V_{DD} = 6\,\text{V}$, then $t_{charge} = 28.52\,\text{ns}$. Knowing that the Arduino board takes around 200 ns to 300 ns to execute a command line, it is clear that using a $C_{unit} = 12.21\,\text{pF}$ is not realistic. As a result, $C_{unit} = 1\,\text{nF}$ was used as a more manageable value for C_{unit}. Combining Equation 4.4 and Equation 4.6 plus using $R_S = 10\,\text{k}\Omega$ and $C_{dl} = 100\,\text{nF}$, the resulting new charging time was calculated to be 2.32 µs. For a $N = 30$ count, a duration of 79.6 µs was calculated for the cathodic phase, including the t_{loss}. These calculations serve just as an example of how different trade-offs affect the operation of the systems, and how different parameters of said system can me calculated. Further simulations and experiments will follow.

Summarizing, two novel topologies were presented for the charge metering and charge balancing capabilities of the output stage of the neurostimulator. In order to proceed with the validation of these two new topologies, a discrete-component implementation for the proposed design was built on a PCB. Simulations of the design, as well as measurements of the PCB will be presented in the following chapter.

5

Validation

The validation of the two designs in Section 4.2 was done in two steps. Firstly, the correct operation of the topology was tested in a standard circuit simulator. Secondly, measurements were done on the PCB prototype in order to further validate the proposed designs.

5.1. Simulations

5.1.1. Circuit Simulations: Ideal Components

All the circuit simulations were performed using LTspice®. In order to do so, an electrical model for the CMUTs, as well as for the tissue, were used. The tissue model was already presented in Figure 2.9. The results form the circuit simulations can be seen in Figure 5.1.

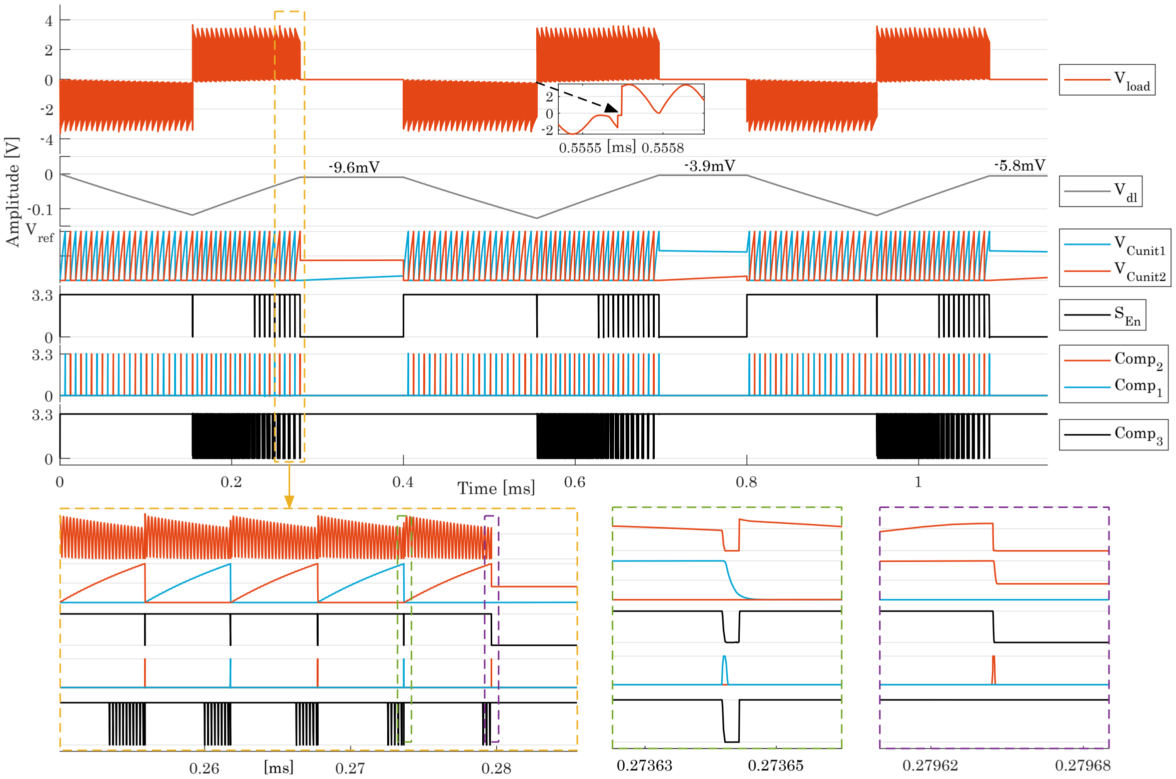

Figure 5.1: LTspice® simulation. Operation of the output stage of the neurostimulator using ideal components. Interphase delay shown in the small zoomed-in plot on top. Yellow rectangle: last counts before the end of the pulse. Green rectangle: sample of $COMP_3 = LOW$ during the second phase, so stimulation is resumed. Purple rectangle: $COMP_3 = HIGH$, so the second phase is ended.

A load model with $R_s = 10\,\text{k}\Omega$ and $C_{dl} = 100\,\text{nF}$ was used in the simulation. In addition, the unit capacitor was chosen to have a size of $C_{unit} = 1\,\text{nF}$. The counter in the system was set to $N = 24$ counts, as seen from the output of the comparators in **Figure 5.1**. The stimulation starts with a cathodic phase that is interrupted as soon as the counts reach $N = 24$. After the cathodic phase, there is a brief interphasic delay, which can be appreciated in the small zoomed plot next to the second pulse in the V_{load} plot. It can also be seen in the input of the control of the enabling switch S_{En}. The second, or anodic, phase starts right after the inter-phase delay, and it comprises two parts. The first part goes in a similar manner as the cathodic phase, but only until $\frac{N}{2} = 12$ counts are reached. The second part interrupts the stimulation every time a count is triggered. This can be seen in the zoomed-in plots. The S_{En} plot goes *LOW* (opens) for a brief moment to make a measurement across the electrodes V_{dl}.

The water window limits for the electrode-tissue interface residual voltage depend on the geometry, materials, etc of the electrodes being used. For example, in [78], cyclic voltammetry of an iridium oxide (IrOx) electrode ($3.7\,\text{mm}^2$) against a saturated calomel electrode (SCE) in a bicarbonate buffered saline solution showed a water window of −0.6 V to 0.8 V. Other values are −0.75 V to 1.25 V for titanium nitride (TiN) [79], or −0.6 V to 0.8 V for 2 mm platinum (Pt) electrodes against Ag/AgCl in a PBS solution [9]. Although these values are large for residual voltages in the electrode-tissue interface, other Faradaic reactions of different ions might take place, even within this water window. As a result, the safety limits for stimulation are usually much smaller than the water window. These limits can range from ±50 mV ([40]) or ±60 mV ([80]), to up to ±100 mV [56].

The residual voltage after each pulse was measured as well for the LTspice® simulations. In this case the measured voltages were 9.6 mV, 3.9 mV and 5.8 mV, which correspond to 96 nC, 39 nC and 58 nC of residual charges respectively. These values are well inside the safety limit.

It is important to notice that in this particular simulation, the source of stimulation was modeled as a voltage source. As a consequence, the operation of the system differs a little bit from the timing scheme presented in **Figure 4.6**. Furthermore, the control of the entire system was done using logic gates in LTspice ®. This control is completely different from the one in the Arduino software, being used in the PCB implementation, which will involve a slightly different control scheme. This can be observed in the output of $Comp_3$, which will be different in the measurements. The specific characteristics of the control were not the main objective of the project, so the simplest control format was chosen for each of the steps in the validation process.

5.1.2. Circuit Simulations: Real Components

The selection of the discrete components for the PCB implementation was done in parallel to the circuit simulations. This means that the chosen components were the ones already present in the LTspice® component library.

LTspice® was not the best tool to model circuits in combination with digital control circuits. A simulation with all the models for all real components, as well as all the control, was not practical for the purpose of this thesis. Instead, each of the real components was simulated individually to test their correct operation within the scope of this project.

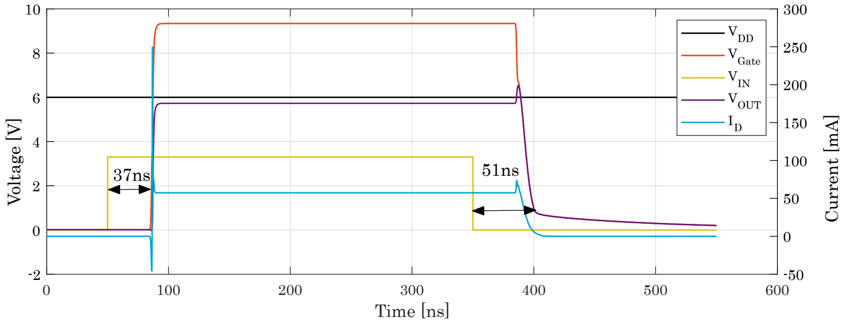

Figure 5.2: LTspice® simulation. Gate driver plus transistor rising time and falling time delays.

The simulations were used to validate the correct performance of the component before buying them for the PCB implementation. Thus the PCB design was done in parallel with these simulations. The most critical simulation was the falling and rising time delays of the transistor drivers. This simulation was done in combination with the transistor and the external capacitor and diodes required for the correct operation of the driver. The results of the simulation can be seen in **Figure 5.2**. As observed, the output rising time delay was simulated to be 37 nC, while the falling time delay was found to be 51 nC. These values were within the expected values reported in the data-sheet of the drivers, which were 13 ns to 90 ns and 13 ns to 40 ns respectively. This means that the delay of the input-output propagation was heavily influences by the driver, and not by the transistor (it was chosen to have a low gate charge $Q_G = 1.4\,\text{nC}$).

5.2. Measurements

The measurements of the PCB prototype were conducted with the same load model as before. This model corresponds to the one of an ideally polarizable electrode, where the Faradaic charge transfer is not present. The capacitor (C_{dl}) models the electrode tissue interface, and a resistor in series (R_s) modeling the tissue resistance [44]. Afterwards, the ideal model was replaced with a pair of electrodes in a phosphate-buffered saline (PBS) solution.

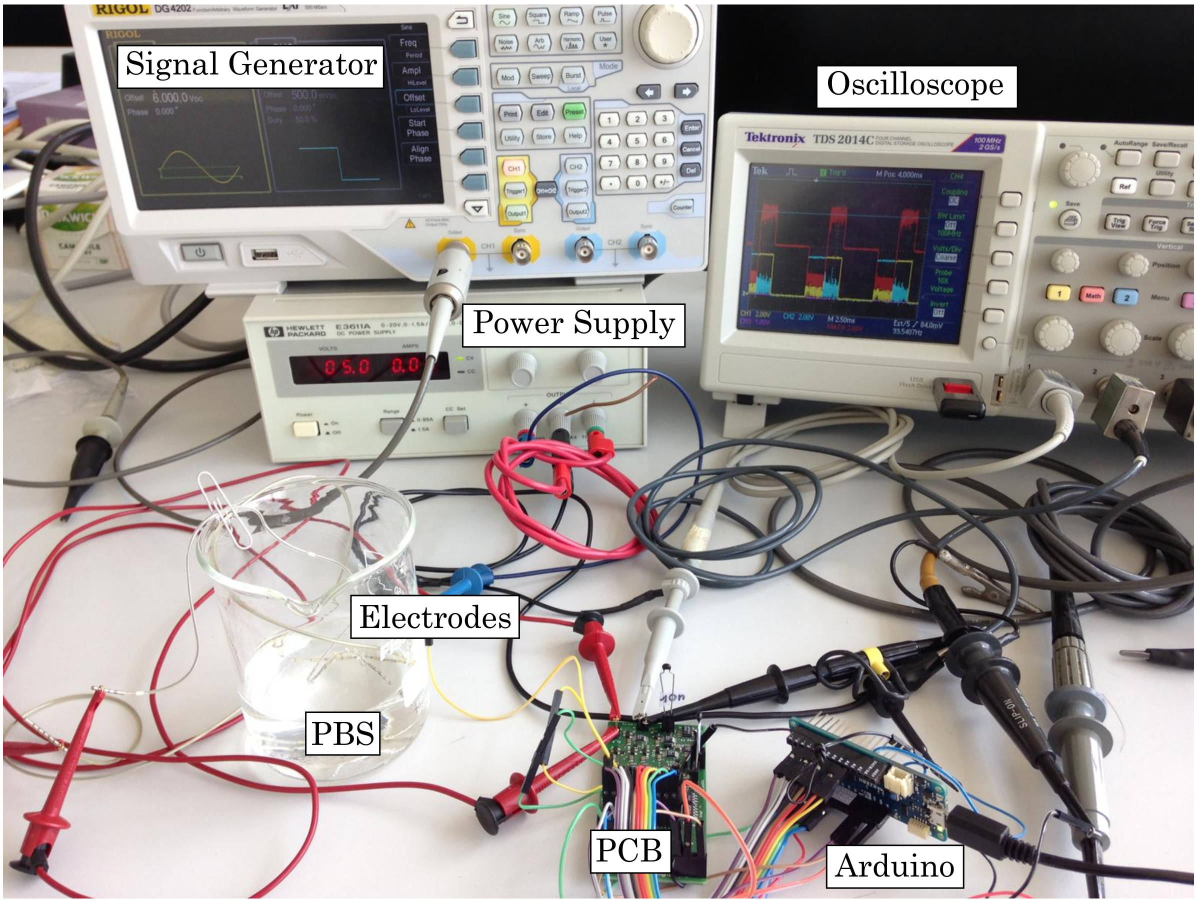

Figure 5.3: Experimental setup for all PCB measurements.

In order to deliver the energy required for stimulation, a power supply was connected to the V_{DD} node of the board. In this case, a voltage source was used for simplicity and availability. The *Hewlett Packard E3611A DC Power supply* was used for this purpose. Once the operation of the board was proven to function as expected from a DC power supply, the supply was replaced with a 2 MHz sine wave generated with a *Rigol DG4202 Signal Generator*. This UHF signal from the generator emulates the incoming signal from a CMUT. It was observed that the high frequency signal appeared as a DC source in the electrodes. Probably the capacitors in the PCB were the cause of this high frequency filtering of the incoming power.These capacitors are the ones responsible for the correct operation of the transistor drivers in the PCB. As it was explained in Subsection 2.2.2, the efficiency of UHF stimulation patterns relies on the fact that power conversion units like AC/DC converters can be removed. In the PCB implementation this was the case and, although an unaccounted DC-like behavior was found, this does not affect the efficiency of the power path between the generator and the electrodes. In conclusion, the DC-like behavior of the generator's output after its rectification does not pose a problem for the operation of the PCB.

A picture of the experimental setup can be seen in Figure 5.3. The measurements were taken with a *Tektronic TDS-2014C Oscilloscope*, and the load pins were connected to an array of electrodes. The electrode lead was submerged in PBS to emulate the environment of the inner body. The PBS solution was of 137 mM $NaCl$, 2.7 mM KCl and 10 mM phosphate buffer. The resistance between electrodes was measured to be around 200 kΩ; which corresponds to R_s in this case.

5.2.1. Charge Metering Measurements

In the proposed circuit, the charge metering circuitry is what guarantees stimulation efficacy. Stimulation efficacy depends on the charge buildup on the electrode-tissue interface, so it is desirable to monitor the voltage and thereby the charge at C_{dl}. In order to do that, the charge metering experiments were performed with the equivalent circuit of the tissue. This allowed to probe the potential at the node between C_{dl} and R_s, which is otherwise inaccessible when electrodes are used instead. Furthermore, all the charge metering experiments were performed on the cathodic phase, as it corresponds to the activation phase.

The first source of inaccuracy when measuring charge comes from the delays within the circuit. The comparators used (LTC1440) have a propagation delay ($t_{comp.delay}$) of 8 µs to 15 µs depending on the overvoltage with respect to the inverting input. Due to this delay, even after the unit capacitor has reached V_{ref}, the stimulation will continue. C_{unit} will continue to charge during the entire $t_{comp.delay}$ and the unit charge for that particular count will be overall increased. The offset charge per count depends directly on the speed at which the capacitor C_{unit} is charging during $t_{comp.delay}$. The rate of charging depends on the difference between the supply voltage and the voltage across the double layer capacitance $V_{C_{dl}}$. In other words, during a count, each unit charge is dependent on the previous ones. The mathematical formulation of all these dependencies is explained below.

For a given count, the charging time can be approximated as the delay $t_{comp.delay}$ plus the C_{unit} charging time from a supply of V_{DD} minus $V_{C_{dl}}$ at that particular instance. Given that the delay between the rising output of the comparator and the control to stop the charging of C_{unit} is around 200 ns to 300 ns, the new delay range was considered to be $t_{comp.delay}$ =8.3 µs to 15.3 µs. The delay is formally formulated as follows:

$$t_{charge,n} = -\ln\left(1 - \frac{V_{ref}}{V_{DD} - V_{C_{dl},n-1}}\right) \times \tau + t_{comp.delay} \tag{5.1}$$

Since $V_{C_{dl}}$ does not change much during one single count, it can be assumed that it is constant during one C_{unit} charging period. As such, the total voltage across C_{unit} at any particular count can be calculated as:

$$V_{C_{unit},n} = \left(V_{DD} - V_{C_{dl},n-1}\right) \times \left(1 - e^{-\frac{t_{charge,n}}{\tau}}\right) \tag{5.2}$$

After each count, $V_{C_{dl}}$ is increased proportionally to the charge stored in C_{unit}, as shown here:

$$V_{C_{dl},n} = V_{C_{dl},n-1} + \frac{V_{C_{unit},n} \times C_{unit}}{C_{dl}} \tag{5.3}$$

In occlusion, the overcharging of C_{unit} is an effect that is stronger during the first counts due to the higher difference between the power supply and the voltage across the double layer capacitance, $V_{C_{dl}}$. As the stimulation progresses the effect is being reduced. This effect was measured and it is presented in Figure 5.4.

The maximum values correspond to the calculations when $t_{comp.delay}$ = 15.3µs is used. The minimum values are consequently calculated assuming that $t_{comp.delay}$ = 8.3µs. As it can be appreciated from Figure 5.4, the measured behavior satisfactorily matches the theorized trend presented above. This effect will be taken into consideration when calculating the maximum (maximum comparator delay) and minimum (minimum comparator delay) expected values in all the subsequent measurement results.

For a neurostimulator to be efficacious, the stimulation intensity should be controllable. In the proposed design the intensity is controlled by setting the number of counts. Measurements of the voltage build-up and the charge delivered as functions of counts were made. The voltage build-up was calculated using Equation 5.1 Equation 5.2 and Equation 5.3 for the maximum and minimum cases with the 15.3 µs and 8.3 µs comparator delays respectively. The Voltage build-up across V_{Cdl} was measured directly with the oscilloscope, and the charge injected was calculated as $Q_{total} = V_{Cdl} \times C_{dl}$. An alternative measurement was made using the voltage across R_s during stimulation. Following Ohm's Law, the current through R_s was computed from the voltage measurements, and then it was integrated over the entire duration of the cathodic phase. The calculated and measured results are presented in Figure 5.5.

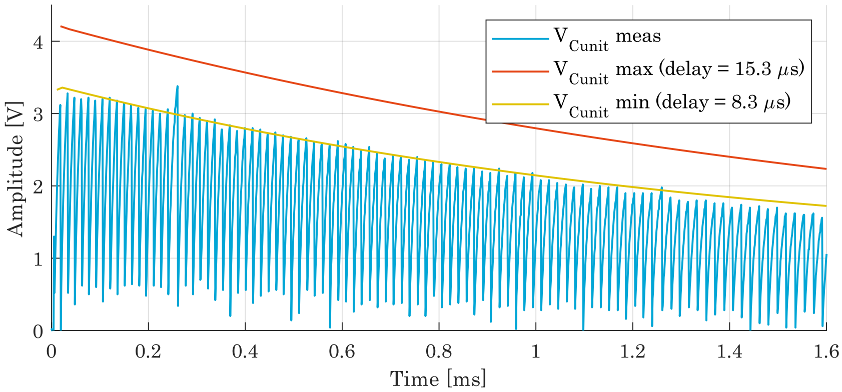

Figure 5.4: Measured (blue) $V_{C_{unit}}$ throughout stimulation; and progression of the calculated minimum (yellow) and maximum (red) $V_{C_{unit}}$ at the end of each count. $R_s = 10\,\mathrm{k}\Omega$, $Cdl = 100\,\mathrm{nF}$ and $C_{unit} = 1\,\mathrm{nF}$.

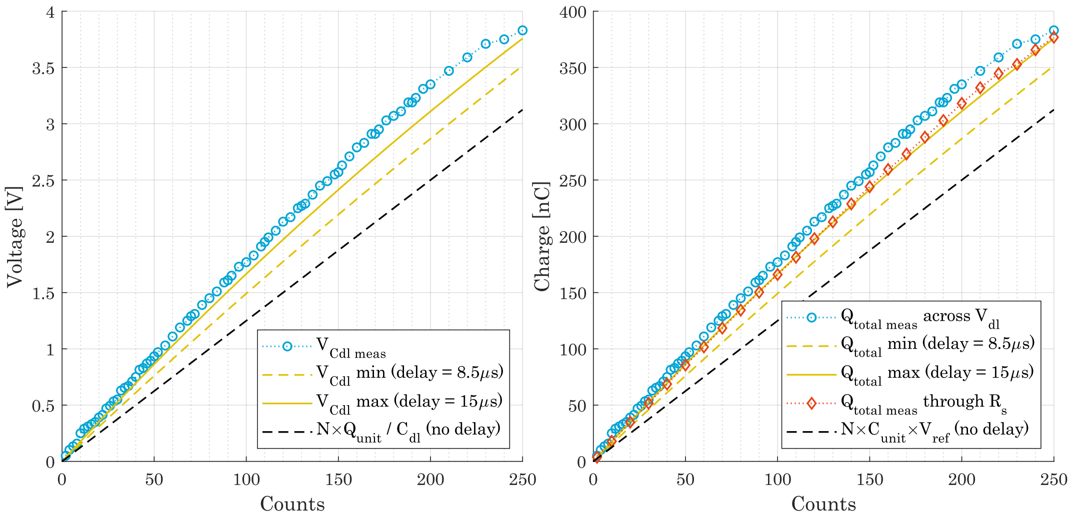

a) b)

Figure 5.5: Stimulation intensities. $R_s = 100\,\mathrm{k}\Omega$, $Cdl = 100\,\mathrm{nF}$ and $C_{unit} = 1\,\mathrm{nF}$. **a)** measured (blue) and calculated (yellow) stimulation intensities, proportional to V_{Cdl}, as a function of counts. **b)** Charge injected as a function of counts. Measured using V_{Cdl} (blue), measured using R_s (red), and calculated (yellow). The ideal cases with no delays in the circuit are shown in the black dotted lines.

As observed in Figure 5.5, the deviation from the ideal case with no delays (in black) increases as the number of counts is increased. As a result, a larger mismatch between the predicted and the delivered charge will happen for high intensity stimulation pulses. Nevertheless, the charge calculated through R_s (show in red) presents a similar trend to the calculated lines (in yellow). As a result it is very plausible that the difference between the measurements and the calculations might be due to an extra delay component that was not accounted for during the numerical calculations. In the case of V_{Cdl}, the measured value deviated a bit more from the expected ones. For lower counts the behavior is within the expected, but for higher counts it starts to deviate. This might be due to the fact that V_{Cdl} is already approaching the supply voltage. In addition, the voltage across C_{dl} after the cathodic phase was measured only once, in order to calculate the total charge delivered. This single point measurement was susceptible to the oscilloscope noise, and it might have lead to the deviation from the calculated values. Although the total charge delivered differs from an ideal case, the behavior of the stimulator is still highly predictable and homogeneous across consecutive stimulation pulses. The control and reproducibility of the charge injection are more important during stimulation than the specific amount of charge being delivered. In this case, the consistency of stimulation and the high resolution of the charge delivery are still proven to be present in the neurostimulator.

The robustness of the charge metering circuitry was measured next. In order to do that, the counts were set to a fixed number, and the supply voltage was swept. In an ideal implementation, the total charge delivered during the first phase should be constant regardless of the supply. In practice, the delay at the comparators still influences the total extra charge that is being delivered during every count. The expected and measured values for the charge delivery in this scenario are shown in Figure 5.6.b. The change in pulse duration for different supply voltages is also shown in Figure 5.6.a and Figure 5.6.c.

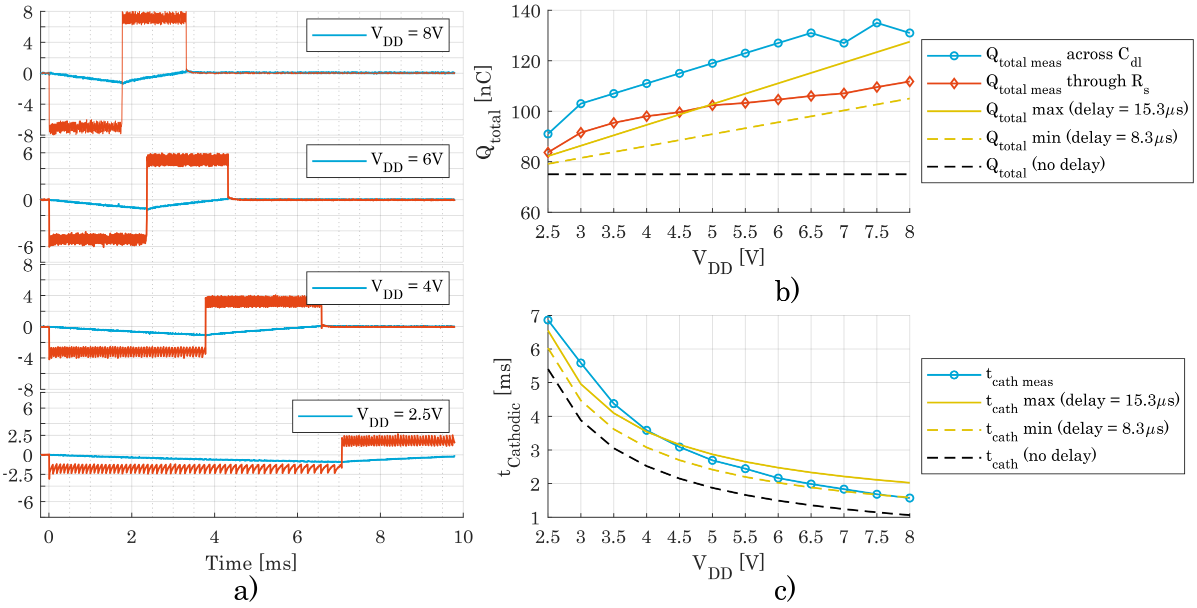

Figure 5.6: Performance at constant $counts = 60$. $R_s = 100\,\text{k}\Omega$, $Cdl = 100\,\text{nF}$ and $C_{unit} = 1\,\text{nF}$. **a)** Biphasic pulses (red) and electrode-tissue interface voltage, $V_{C_{dl}}$ (blue), for V_{DD} =2.5 V to 8.0 V. **b)** $Q_{total} vs. V_{DD}$. **c)** Cathodic pulse-width $t_{Cathodic} vs. V_{DD}$.

As seen in Figure 5.6.a, when the voltage supply was decreased, the stimulation pulse-width increased. This self regulating capabilities are a direct proof of the charge metering topology operation. It was also observed that the anodic phase was shorter in all cases although the number of counts was the same. This is because the voltage that charges C_{unit} is $V_{DD} + V_{C_{dl}}$ due the fact that the polarity of the stimulation has been reversed. As a result, the unit capacitor charges much faster during the beginning of the anodic phase.

Regarding the total charge as a function of V_{DD} it was observed that the measurements were not always in accordance to the calculations. As seen in the red plot, measured using the current through R_s, at low power supplies the circuit behaves more like the predicted values with the maximum delay scenario, while at higher voltages the circuit behaves like the predicted values for the minimum delay scenario. This is not surprising, as the delay of the comparator is highly dependent on the voltage difference between its inputs. This means that at lower voltages C_{unit} reaches V_{ref} slower, and the comparator expresses a larger delay. For high V_{DD} voltages, the unit capacitor reaches the reference faster, and the comparator threshold is crossed more rapidly, which results in a smaller delay. This might explain why the neurostimulator behaves slow for small V_{DD}s and fast for bigger V_{DD}. The consequence is that the neurostimulator has a flatter curve as compared to the calculated values, which is a desirable effect because the total charge should remain as constant as possible.

Once again, using $V_{C_{dl}}$ as a direct measurement of the charge does not lead to accurate predictions because for small values of $V_{C_{dl}}$ the signal becomes noisy. On the other hand, the duration of the pulses as a function of the supply voltage was measured with high accuracy, and its values are shown in Figure 5.6.c. Here the overall trend of the measurements follows the ideal situation with no delays, and the calculated predictions with the largest and smallest comparator delays. As observed in Figure 5.6.b, the circuit seems to behave slow at low power supplies and fast at higher ones. Figure 5.6.a also reinforces this statement, as the individual counts are more visible in the bottom graph.

In conclusion, the delay components of the circuit are the most critical parameters, as they influence the operation of the charge metering circuit. The consequence of that delay might be the following. If a charge threshold is established for activation at a certain supply voltage, if the voltage gets reduced, then the efficacy of stimulation might be compromised because the same number of counts will not build up the same amount of total charge. It is fair to note that these drawback is predominant for large number of counts or for very big changes in power supply (like 2.5 V to 8.0 V in Figure 5.6.c). In the envisioned application, the charge metering circuitry compensates small changes of an unreliable power source, like the ones provided with

WPT links, thus it is fair to assume that the activation will be guaranteed for a specific number of counts. Furthermore, the charge delivery could always be easily adjusted very precisely by means of increasing the number of counts

To summarize, the neurostimulator was found to be highly dependent on the delays in the control of the system, making it non-linear. Nevertheless, it's behavior can be easily predicted and compensated for.

5.2.2. Charge Balancing Measurements

The objective of the charge balancing topology is to bring the voltage across the electrodes back to zero, after the cathodic phase has ended. An acceptable range for the residual voltage is anywhere within the water window. As explained before, the water window depends on the particular dimensions and materials of the electrodes, but it is usually in the range of −0.6 V to 0.8 V. The safety window for stimulation is usually in the order of ±50 mV ([40]) to ±100 mV ([56]) in order to avoid other irreversible reactions apart from the oxidation or reduction of water.

As explained in Section 4.2, the anodic phase was purposely reduced to half of the counts with respect to the cathodic phase. If there is no charge balancing in place, the residual voltage will remain far from zero. This can be seen in Figure 5.7.a and Figure 5.7.b, where the V_{dl} does not return back to zero by the end of the anodic phase. Contrariwise, when the charge balancing topology is activated, the voltage (V_{dl} in grey) across the double layer capacitance is successfully brought back to zero, which can be appreciated in Figure 5.7.c and Figure 5.7.d.

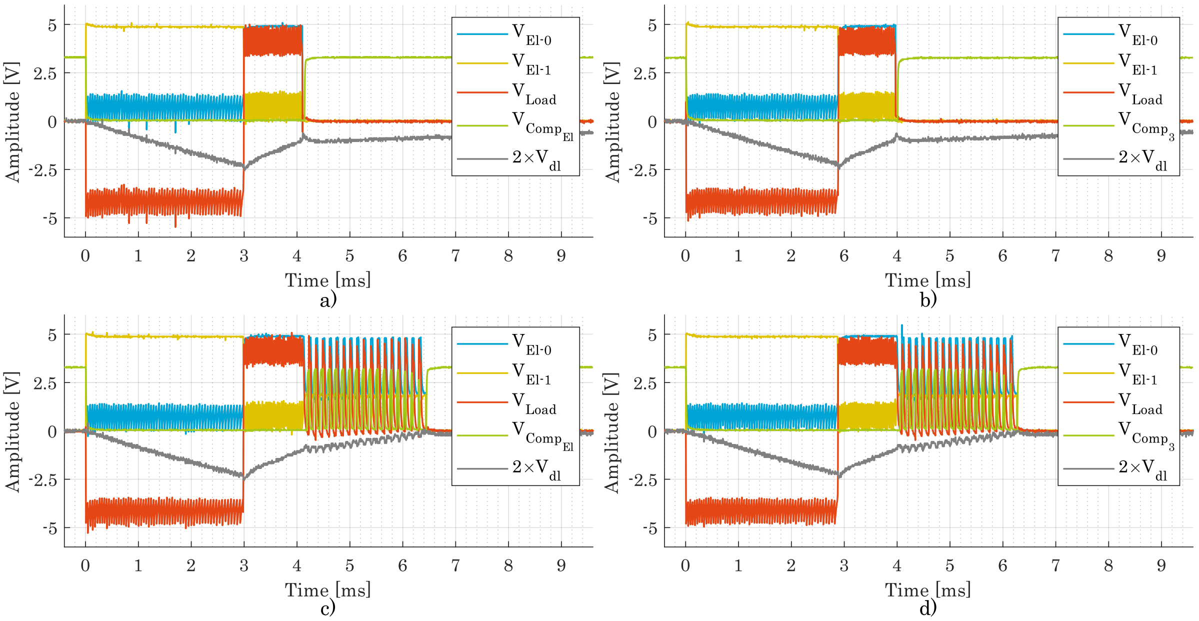

Figure 5.7: Biphasic pulse. $R_s = 100\,\text{k}\Omega$, $Cdl = 100\,\text{nF}$, $C_{unit} = 1\,\text{nF}$, $counts_{cath} = 60$, and $counts_{anod} = 30$. **a)** Improved topology with one C_{unit} capacitor, and charge balancing deactivated. **b)** Initial topology with two C_{unit} capacitors, and charge balancing deactivated. **c)** Improved topology with one C_{unit} capacitor, and charge balancing activated. **d)** Initial topology with two C_{unit} capacitors, and charge balancing activated.

Figure 5.7.a and Figure 5.7.c serve as a prove that the new topology with one single capacitor C_{unit} can lead to the same performance as the original one with two. This can be seen in the great similarity between Figure 5.7.a and .b, and Figure 5.7.c and .d. This novel topology has the advantage that the capacitive area of the circuit can be reduced by 50%, and one of the comparators can be eliminated as well. In all cases in Figure 5.7, the anodic phase was followed by a shorting phase that lasts the entire duration of the interpulse delay. This interpulse delay is not enough, as seen in Figure 5.7.a and Figure 5.7.b, because the voltage takes longer than the interpulse delay to get back to zero. This proves, once more, that active charge balancing is required.

The detailed operation of the charge balancing for the novel topology with one single capacitor is shown in Figure 5.8.

Figure 5.8.a details the operation of the circuit in the presence of charge balancing. The charge balancing in Figure 5.8.a is performed as follows. The node names in Figure 4.5 will be used here. At time 5.5 ms,

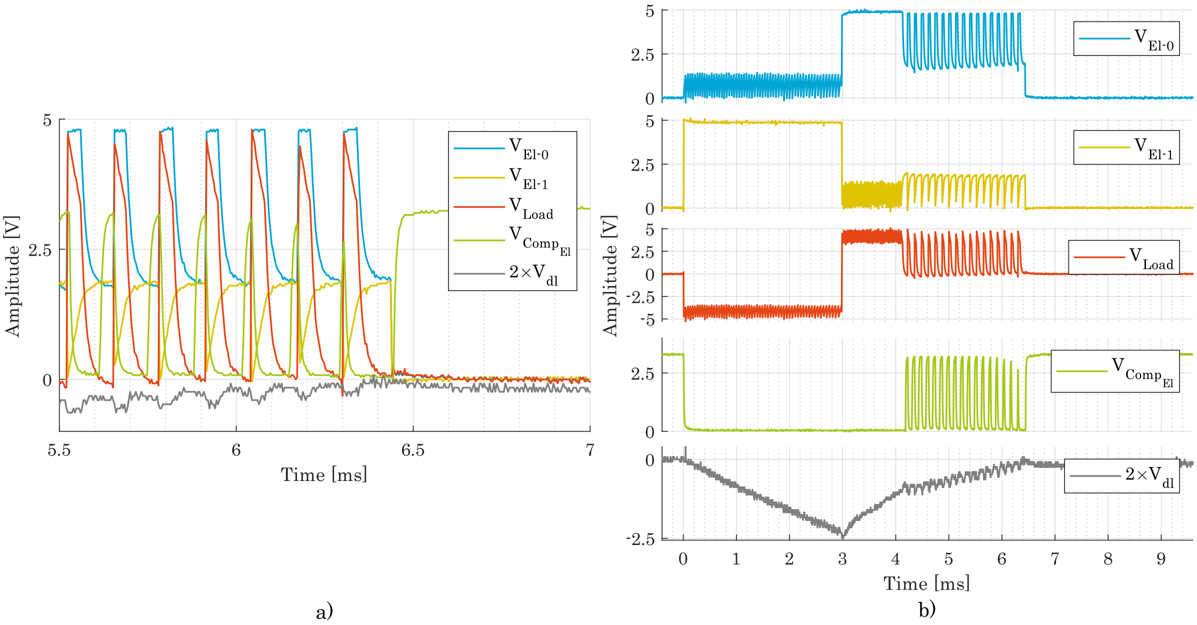

Figure 5.8: Biphasic pulse with active charge balancing for the novel topology with one single capacitor. $R_s = 100\,\mathrm{k\Omega}$, $Cdl = 100\,\mathrm{nF}$, $C_{unit} = 1\,\mathrm{nF}$, $counts_{cath} = 60$, and $counts_{anod} = 30$. **a)** detail of the last part of the charge balancing phase during the anodic part of the pulse. **b)** Entire biphasic pulse with active charge balancing and one single unit capacitor. Each signal has been presented facilitate the understanding of the circuit operation .V_{dl} was doubled to appreciate the amplitude variations in the plott.

V_{El0} (blue) or working electrode is driven positive to V_{HIGH} (same as V_{DD} because the enabling switch is on) because it is the anodic phase. Similarly V_{El1} (yellow) is driven low to V_{LOW} (sames as $V_{C_{unit}}$). V_{Load}, defined as $V_{El0} - V_{El1}$ is equal to V_{DD}. At all times the negative input of comparator is connected to V_{HIGH} and the positive input to V_{LOW}. So initially, the output $V_{COMP_{El}}$ is *LOW*. As the stimulation progresses, the unit capacitor charges, thus increasing the potential at V_{El1} to the voltage reference V_{ref}. This can also be seen in V_{Load} which decreases to $V_{DD} - V_{ref}$. Once V_{ref} is reached, the stimulation stops. V_{El1} remains at V_{LOW} and V_{El0} quickly drops to $V_{LOW} + V_{Load}$. Since $V_{Load} = V_{dl} < 0$, the voltage at V_{El0} is lower compared to V_{El1}, and the comparator triggers, outputting $V_{COMP_{El}}$ =*HIGH*. This trigger resumes the stimulation, and the cycle is repeated. At time ≈6.45 mV, $V_{C_{unit}}$ is charged to the last time to V_{ref}, thus stopping the stimulation. Similarly to before, V_{El1} stays at V_{ref} and V_{El0} drops to $V_{LOW} + V_{Load}$. But this time, V_{dl} is positive, so V_{El0} is not lower than V_{El1} anymore, and the stimulation pulse stops. Right after the en of the anodic phase, both electrodes are shorted to remove any further residual charge. This shorting phase can be seen as both V_{El1} and V_{El0} quickly drop to ground. Because $V_{El1} = V_{El0} = GND$ comparator $V_{COMP_{El}}$ triggers to high, and remains there due to the hysteresis effect, which requires a −50 mV difference to go back to *LOW*. This completes the operation for a single charge balance stimulation pulse.

Regarding the influence of the supply voltage on the charge metering circuitry, more experiments were conducted. Just like in Figure 5.6, the voltage supply was swept to measure the residual voltage after each of the biphasic pulses. Figure 5.9 shows the measurement results for different V_{DD}s. Figure 5.9.a-d illustrate the charge balancing technique in the case of four different supply voltages in the range of 3.0 V to 8.0 V. The voltage across the electrodes returned to values ranging from −82 mV to 30.4 mV for supplies form 3.0 V to 8.0 V respectively. As a side note, the pulse width increased when V_{DD} decreased, which indicates that the charge metering and charge balancing circuits can work simultaneously. Similarly, when C_{unit} was changed to $C_{unit} = 0.82\,\mathrm{nF}$ and to $C_{unit} = 0.51\,\mathrm{nF}$, for a 5 V supply. The residual voltages on a $C_{dl} = 180\,\mathrm{nF}$ were 0.5 mV, 4.1 mV and 29.6 mV for 1.00 nF, 0.82 nF and 0.51 nF respectively. These correspond to residual charges of 90.0 pC, 738 pC and 5.32 nC, which translate to 0.07, 0.72 and 8.42 C_{unit} counts. In order to obtain the residual voltage values, a Matlab smoothing algorithm was used on the output data of the oscilloscope, which used a Gaussian-weighted moving average over a of 50 data-points of 0.1 µs. all these values fall withing the safety window of ±100 mV in [56], and most of them under the ±50 mV ([40]) window too.

In the prototype design, different C_{unit} capacitors were used in order to establish their effect on the residual voltage after stimulation, as shown above. As explained in Section 4.2, due to the specifications of the Arduino, there is a minimum to the C_{unit} capacitance. This lower limit is defined by the requirements of the

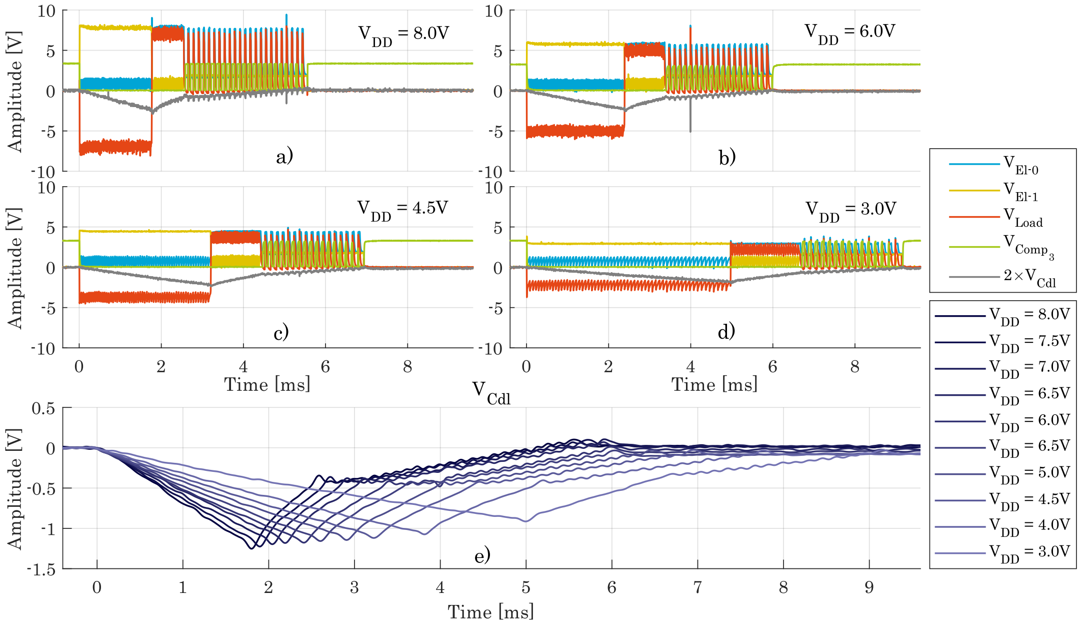

Figure 5.9: Biphasic pulses with charge balancing activated. R_s = 100 kΩ, Cdl = 100 nF, C_{unit} = 1 nF, $counts_{cath}$ = 60, and $counts_{anod}$ = 30.**a-d)**: biphasic phases for four different supply voltages: 8.0 V,6.0 V,4.5 V and 83.0 V. **e)** $V_{C_{dl}}$ for 3 V to 8 V.

charge metering operation of the device. Similarly, the charge balancing circuitry also sets some upper limits for the values of C_{unit}. During the anodic phase of the stimulation pulse, the voltage across the electrodes is being built-up by individual packages of $Q_{unit} = C_{unit} \times V_{ref}$. In a successful charge metering circuit, this Q_{unit} should increase the voltage cross the electrodes by an lesser amount than the safety window of the system. If that is the case, then the last count right before the end of the anodic phase will never lead to a residual voltage higher than the safety window. Based on this requirement, the following relation can be obtained:

$$\frac{Q_{unit}}{C_{dl}} < V_{safety}; C_{unit} < \frac{V_{safety}}{V_{ref}} \times C_{dl} \tag{5.4}$$

In most of the experiments, a capacitor $C_{dl} = 100\,\text{nF}$ was used to model the double layer capacitance. Given that $V_{ref} = 1.25\,\text{V}$, if the safety window is withing the range of $V_{safety} = \pm 50\,\text{mV}$, then the maximum allowed unit capacitor would be:

$$C_{unit} < \frac{0.05\,\text{V}}{1.25\,\text{V}} \times 100\,\text{nF} = 4\,\text{nF}$$

Otherwise, if $V_{safety} = \pm 100\,\text{mV}$:

$$C_{unit} < \frac{0.1\,\text{V}}{1.25\,\text{V}} \times 100\,\text{nF} = 8\,\text{nF}$$

The values of C_{unit} used during the measurements were $C_{unit} = 1\,\text{nF}$, $C_{unit} = 0.82\,\text{nF}$, and $C_{unit} = 0.51\,\text{nF}$. This means that, although the measurements of the residual voltage had to be done with curve smoothing techniques, it is safe to assume that the safety limits are being respected.

5.2.3. *In vitro* Measurements

The last measurements were dedicated to the stimulation of electrodes in PBS. For these measurements, the voltage across the double layer capacitance C_{dl} cannot be measured. Similarly, the current through the resistor R_s cannot be monitored. As a result, only the voltage across the two electrodes was monitored.

For these experiments, a single pellet of PBS was used to create a 137 mM $NaCl$, 2.7 mM KCl and 10 mM phosphate buffer solution. The resistance across the electrodes while submerged in the solution was 250 kΩ. The right connection was establish by trial and error, while trying different C_{unit} capacitors and different pairs of electrodes. Dues to the lack of time it was not possible to characterize the electrodes. This experiment was performed just as a proof of concept while using a real load, instead of an equivalent circuit. The value for C_{unit} was 10 nF.

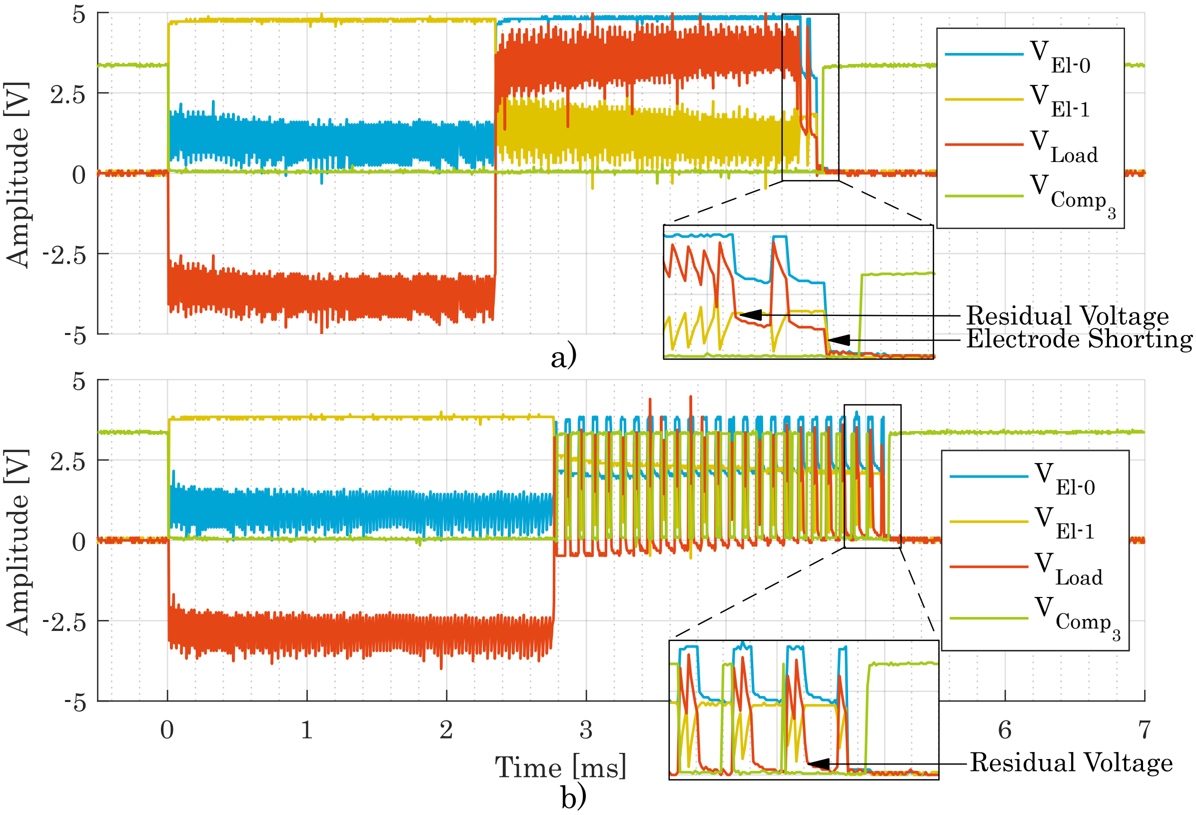

Figure 5.10: *In vitro* measurements.**a)** biphasic pulse with no charge balancing; $counts_{cath} = 120$, and $counts_{anod} = 120$. V_{DD} =5 V and $C_{unit} = 10$ nF. **b)** biphasic pulse with no anodic phase and with the charge balancing activated; $counts_{cath} = 120$. V_{DD} =4 V and $C_{unit} = 10$ nF.

Figure 5.10.a shows the case where there was no charge balancing programmed in the Arduino microcontroller. Counts of $counts_{cath} = 120$, and $counts_{anod} = 120$ were used. In this case, after the anodic phase the electrodes were shorted (as usual) and the voltage rapidly lowered ground. The exact mechanism for such a rapid discharge should be studied in the future. In order to appreciate the residual charge after an stimulation pulse, two small counts ($C_{unit} \times V_{ref}$) were programmed at the end of the anodic phase. As seen in the small close-up in Figure 5.10.a, the voltage had indeed built-up during the anodic phase. the value for the residual voltage was 1.32 V after the first dummy count, and 1.2 V in the second one. Immediately after, the voltage quickly dropped to zero. This proves that for *in vitro* experiments, there is still residual charge that has to be accounted for.

In Figure 5.10.b charge balancing was obtained with the same procedure as in Figure 5.8. In this particular case, the stimulation was successfully stopped when zero voltage was reached. A residual voltage of 80 mV was measured right after the last charge balancing pulse. Given that the $C_{dl}$is is unknown, it is not possible to calculate what was the expected residual voltage when using $C_{unit} = 10$ nF. In any case, $V_{safety} = \pm 100$ mV is used, then the stimulation is still successfully balanced.

6

Conclusions, Contributions and Recommendations

6.1. Conclusions and Contributions

This work presents a new system topology for an implantable device for electrical stimulation. The new topology comprises a network of neurostimulators that can be placed in different locations under the scalp for the treatment of chronic head deceases. The system utilizes the ultrasound conductivity of the skull to deliver power to the implant network. It was demonstrated that the bone can be used as an ultrasonic conductor with an attenuation of around 20 dB. The ultrasonic conduction was found to happen mostly in two frequency bands, which are 0.1 MHz to 0.6 MHz and 1 MHz to 2 MHz. It was observed that the 1 MHz to 2 MHz band conducts mostly in bone but not in other tissues, so 2 MHz was selected as the preferred frequency of operation for the WPT link.

The transduction of acoustic energy into electrical energy was proposed to be done with a CMUT in collapse mode. CMUTs can have up to 76% transduction efficiency, which place them as a very good option to maintain a good power efficiency in the WPT link [30]. In the proposed neurostimulator, the high frequency 2 MHz signal was rectified and used to "directly" stimulate the tissue using the ultra-high frequency technique. Regarding the neurostimulator, the main focus of this work was put into the output stage design. For this, a new charge metering and charge balancing topology was presented. For the charge metering circuit, an initial design with two unit capacitors C_{unit} (in series with the stimulation path) was proposed. The unit capacitors are charged and discharged alternately for a specified number of times, allowing the build-up of charge at the electrode-tissue interface with a resolution of $C_{unit} \times V_{ref}$. The charge metering circuit was further improved with a new topology that allowed for the use of only a single unit capacitor. For the charge balancing, the voltage across the electrodes gets monitored during the second phase of stimulation. Between two consecutive C_{unit} charging phases, the stimulation is interrupted and the voltage across the electrodes is measured using a comparator. This charge balancing technique brings the voltage across the electrodes back to zero in an active manner. Consequently, both tissue damage and electrode damage are prevented. The resulting topologies add only a capacitor C_{unit}, two comparators and four additional switches to the H-bridge of the neurostimulator, making the topologies simple, compact, multichannel compatible, and highly scalable.

The charge metering and charge balancing topologies were implemented on a PCB together with the Arduino *Arduino MKR Zero* microcontroller. The prototype was able to successfully deliver the required charge by means of controlling the number of counts. The charge resolution of the prototype was of 1.25 nC when $C_{unit} = 1\,\text{nF}$ and $V_{ref} = 1.25\,\text{V}$ were used, which corresponded to a $V_{C_{dl}}$ increase of 12.5 mV for $C_{dl} = 100\,\text{nF}$. The behavior of the PCB during the charge metering matched the predicted calculated behavior, as seen in Figure 5.5 and Figure 5.6. For the charge balancing circuit, the residual voltage was successfully brought back withing the safety window. residual voltages of −82 mV to 30.4 mV were obtained for voltages from 3.0 V to 8.0 V. A range of 0.5 mV to 29.5 mV was measured for different C_{unit}: 1.00 nF, 0.82 nF and 0.51 nF respectively. These values are acceptable with stricter safety window requirements of ±50 mV. The maximum residual charge or voltage was determined by the count resolution, which was 1.25 nC again. *In vitro* measurements in a PBS solution were made, and the proposed system performed as expected with a residual charge of 80 mV, well within the V_{safety} =±100 mV safety window.

6.2. Recommendations for Future Work

- **Ultrasonic wireless data transfer.** In this work, it was demonstrated that the ultrasonic wireless link can be used to power the neurostimulators. The work did not explore the communication link between the outside world and the neurostimulator. As seen in Chapter 3, the constructive and destructive interference of the pressure waves corrupt the transmitted waveforms, so they cannot be used to transmit information in amplitude. In future work, alternative methods for wireless information transfer should be explored. For example, the information could be encoded in frequency, or it could be transmitted through a completely different wireless link. Furthermore, the bone conduction technique was only validated using simulations. More experiments should be conducted in the future to prove the bone conduction concept and to quantify the real attenuation of ultrasonic waves along the skull.

- **Ultrasonic transducer.** This work presents CMUTs as a good option for the power receiver side in each of the neurostimulators. The WPT link and the CMUT were not included in the measurements of this project. The correct operation of the system with a CMUT as the power source should be tested in the future.

- **Neurostimulator blocks.** The focus of this work was put on the output stage of the neurostimulator. Not all the blocks in Figure 4.4 were implemented. In the future, the digital unit of the neurostimulator should be designed in accordance to its control requirements. Additionally, the design of a small energy storage unit is necessary for the operation of the digital block. Furthermore, other blocks like the data demodulator and clock generator or extractor should be implemented as well.

- **Multichannel operation.** The topologies of the charge metering and charge balancing circuits were made for a multichannel operation of the neurostimulator. The operation of such a multichannel neurostimulator would rely on the ability to charge each of the channels in an alternating fashion, one count at a time, as explained in Subsection 4.2.1. The multichannel operation was not tested in the PCB measurements for simplicity and due to time constraints. In future versions of the prototype, multiple channels should be included on the PCB in order to evaluate and validate this proposed multichannel operation.

- **PCB improvements.** There were a couple of drawbacks in the PCB implementation. The driver circuits used to control the transistors had some external components like 0.1 µF capacitors, which limited the frequency performance of the neurostimulator. In a future prototype, the transistors used for the switching could be controlled directly by generating the required gate voltages. Regarding the size of the PCB, it could be further reduced by optimizing the placement of the components and even by placing the components on both sides of the board. These improvements should not be the priority, as the ultimate goal is to integrate the neurostimulator in an IC. These improvements might help to minimize the side of the experimental setup, which can facilitate *in vitro* and *in vivo* measurements.

- **Designing for delays.** It was shown that the accuracy of the charge metering, and thus the efficacy of the system, is highly dependent on the delay of the comparators as well as the delay in the microcontroller signals. Future implementations should be design with these delays in mind, in order to minimize them.

- **More measurements.** The residual voltage and residual charge measurements of the system were hard to quantify, due to the measurement setup limitation. In a future implementation, an analog amplifier could be included in the PCB design in order to measure the residual voltage across the electrodes. If this is implemented, then the residual voltage as a function of C_{unit} and V_{ref} could be calculated.

- **Circuit integration.** Ultimately, the goal of this work is to design a neurostimulator that could be implemented into an IC. The design of the IC should already include all the building blocks of the neurostimulator as well as the CMUT. Ideally, such an IC would then be integrated in the fabrication flow for the electrodes and encapsulation as well.

A

LASCAS 2020 paper

Circuit Design Considerations for Power-Efficient and Safe Implantable Electrical Neurostimulators

Rui Guan[1†], Pedro G. Zufiria[1†], Vasiliki Giagka[1,2] and Wouter A. Serdijn[1]
[1]Section Bioelectronics, Dept. Microelectronics, Faculty EEMCS, Delft University of Technology, Delft, The Netherlands
[2]Technologies for Bioelectronics Group, Fraunhofer Institute for Reliability and Microintegration IZM, Berlin, Germany
Email: R.Guan-1@tudelft.nl, P.G.ZufiriaGerboles@student.tudelft.nl, V.Giagka@tudelft.nl, W.A.Serdijn@tudelft.nl

Abstract— **This paper presents the main circuit design considerations for power-efficient and safe implantable electrical neurostimulators. Related to medical applications, low-frequency (LF) stimulation for generating new action potentials and kilohertz-frequency alternating current (KHFAC) for blocking unwanted neural activity are introduced, respectively. For implantable medical devices, the choice of energy source type is important as it has an influence on the total size of the device and device comfort, thereby affecting the quality of life of the patients. In order to lengthen the lifetime of the stimulator, power-efficient designs using the ultra-high frequency (UHF) pulsed technique are proposed. To avoid tissue damage and electrode degradation caused by residual charge on the electrode-tissue interface (ETI), charge balancing (CB) techniques are adopted. Active CB control is shown to be a promising method both for LF and KHFAC stimulation.**

Keywords—implantable electrical neurostimulator, power efficiency, safety, active charge balancing.

I. INTRODUCTION

Neuromodulation technologies are widely used for the treatment of various diseases caused by neural disorders. They can provide patient-tailored therapy with less side effects than conventional medicine [1]. Neural activity manifests itself, a.o., as changes in the membrane voltage [1]. The principle of neuromodulation is to change said membrane voltage to excite or inhibit nerve cells by means of pulses with specific properties, such as pulse shape, pulse repetition frequency, pulse duration, pulse magnitude, etc.

Until now, electrical, optical, ultrasonic and magnetic forms of stimulation have been shown to elicit certain responses from nerve cells, but electrical stimulation is the most common method [2]. Electrical stimulation uses electric charge to generate the required electric field to depolarize or hyperpolarize the cell membrane. This electric charge can be built up by means of controlling any electrical quantity, viz. charge, current or voltage in the stimulation site [2].

According to their working principle, there are mainly two kinds of application fields for implantable electrical neurostimulators. One, commonly employed for vagus nerve stimulators, cochlear implants, retinal implants, etc., is to induce artificial neural activation (commonly referred to as neurostimulation) by evoking new action potentials. This is commonly achieved by using low frequency pulses [2], in the range of below or around 100 Hz. The other application lies in the fields of blocking unwanted neuronal activity in cases of urinary retention, chronic pain, etc. This "conduction block", as is commonly referred to, is in most cases achieved through kilohertz-frequency alternating current (KHFAC) stimulation [3].

Batteries have been commonly used as the preferred powering technique for most active implantable devices. More recent technologies are shifting towards wireless power transfer (WPT) methods [4]. These methods allow for the miniaturization of the implants while increasing their functional lifetime, as opposed to the bulkiness and low durability of batteries. The most common techniques can be categorized as: acoustic power transfer (APT) using ultrasound (US), RF far-field power transfer (RF), and near-field inductive coupling (NF) [4].

For neurostimulation, from a power efficiency perspective, it is desirable to have the neural stimulator as close as possible to the target tissue. Besides, power efficiency also determines the size and lifetime of the energy source, and heat dissipation should be minimized to avoid any tissue damage caused by an increased temperature inside the body. To address these issues, a promising method is the UHF current pulsed technique [5], which employs a filter-less DC-DC converter and thereby avoids the need of bulky filtering capacitors for stabilizing the converter output voltage.

Besides power efficiency, the other biggest challenge is safety, which requires stimulation schemes that will not lead to tissue damage and electrode degradation [6]. According to the Shannon criteria [7], the charge per phase delivered to the tissue and residual charge on the ETI should be within specific safety limits. This means that the offset voltage on the electrodes, which is proportional to the residual charge, should stay within a safety window [8]. However, the offset voltage usually goes up during stimulation due to the charge mismatch between the cathodic and anodic phases, and nonlinearities of the electrode-tissue interface (ETI) [9, 10]. For this reason, safety control techniques are necessary to automatically ensure that the offset voltage meets the safety requirements. These available techniques are different for LF stimulation and KHFAC stimulation applications, due to the different stimulation patterns.

The rest of the paper is organized as follows: Section II introduces the powering techniques for implantable electrical neurostimulators. Power-efficiency and safety-control schemes are presented in Sections III and IV, respectively. These are followed by the conclusions in Section V.

[†] These two authors contributed equally to the work.

II. POWERING TECHNIQUES FOR IMPLANTABLE ELECTRICAL NEUROSTIMULATORS

The two main approaches to power implantable electrical neurostimulators are batteries and wireless power transfer (WPT) methods. Energy harvesting and scavenging are alternative ways of powering devices, but because they depend on the availability of energy in the environment, they can never be reliable enough for some applications, like most neurostimulators, due the scarcity of available energy [4].

A. Battery

Batteries provide a reliable and constant source of power but at the cost of big size and limited lifetime. Patients need to undergo surgery to replace a new battery when the old one has depleted. This gives a lot of economical, physical and mental burden to patients. In addition to this, batteries contain chemicals and materials that are not necessarily biocompatible, which requires stricter protection and packaging precautions.

B. Wireless Power Transfer (WPT)

Because of the aforementioned limiting factors of batteries, new advancements are pointing at wireless power transfer methods as the most promising alternatives. In principle, there are many ways of wirelessly transferring power inside the body. To determine the choice of WPT method mentioned in Section I, implantation depth, device size, biocompatibility and biostability of the implants are a few design parameters to be taken into account. For example, ultrasonic power transfer has been proven to outperform the other methods, when the implant is located deep (>10 cm) inside the body [4]. On the other hand, the power transfer efficiency of bigger devices implanted close to the surface is higher when an inductive coupling link is used [4], like in the case of cochlear implants.

The efficacy of the stimulation is related to the amount of charge delivered to the tissue [6]. This charge is commonly controlled by setting the duration of a well-known constant energy source. Two examples are constant-current stimulation (CCS) and constant-voltage stimulation (CVS). However, one common disadvantage of all WPT methods is that the links are not always reliable or constant, and the receiver side does not always behave like an ideal current or voltage source. As a result, in order to have a reliable source when a WPT method is in place, standard implantable electrical neurostimulators usually have a small energy storage unit [11]. If the local power storage unit is minimized or removed altogether, the control of the charge cannot be made by setting the duration of the stimulation pulse. As a solution, and to ensure activation efficacy, we propose to introduce charge metering techniques in the neurostimulator design.

III. POWER EFFICIENT TECHNIQUES

The use of a constant current source is common in traditional stimulation schemes, but it wastes a lot of power because the supply voltage is commonly designed for the worst case when the load impedance and thus the voltage across the ETI are high [5]. There are many techniques those can be implemented to improve the power efficiency of implantable electrical neurostimulators. One popular method is the implementation of a current source with an adaptive power supply [12], but it still wastes quite some power in multichannel operation. This is because its adapted voltage compliance would still cause power losses in those channels with smaller load impedances [5].

The ultra-high frequency (UHF) pulsed stimulation approach is another promising power-efficient technique. The UHF approach takes advantage of the capacitive behavior of the cell membrane to integrate a series of high-frequency (in the order of MHz) pulses and build up the charge required for cell activation [13]. The UHF pulses can be delivered to multiple channels in an alternating fashion, significantly improving the power efficiency in a multichannel configuration [5].

If the implant is being powered from a battery, the UHF technique can be applied by using a DC-DC converter to generate UHF pulses [5]. On the other hand, if the implant is being powered from a wireless power transfer link, the signal can be “directly” used for the UHF technique by means of a simple full-wave rectification [14]. This eliminates AC/DC converters and other power management blocks from the power path between the WPT link and the tissue, thereby increasing the power efficiency of the system. Both batteries and WPT methods can be used for LF stimulation and for KHFAC blocking schemes, increasing their power efficiency.

IV. SAFETY CONTROL TECHNIQUES

The proposed neurostimulators must comply with safety standards for medical applications. To ensure stimulation safety, it is crucial to have a charge-balancing technique in the system that can monitor and compensate the charge accumulation on the ETI. This ensures that the voltage across the ETI remains within the safety limits.

A. Charge Balancing Techniques for Low Frequency Stimulation

For LF stimulation, CB is usually implemented by a blocking capacitor or high-pass filter in series with the stimulation current source, to eliminate the DC component of the source. This technique cannot ensure safety because of the serious nonlinearity of the ETI [10]. Besides, the blocking capacitors are usually in the order of μF, which are not practical for integrated stimulator designs, especially for multichannel operation.

Other common CB practices match the charge in the cathodic and anodic phases [15]. This method does not account for the nonlinearities of the ETI and, as a result, also cannot guarantee safety [6].

A third technique is passive discharging during the interpulse delay in every stimulation cycle [16]. For this, the electrodes are grounded after each bi-phasic (cathodic and anodic) pulse. However, this method lacks accuracy because of the uncertainty about the residual charge after each stimulation phase. In addition, the interpulse delay might not be long enough to fully discharge the electrodes due to the large time constants of the system.

Pulse insertion is another popular technique [17]. As the name suggests, it takes advantage of the interpulse delay to inject some extra pulses into the tissue and compensate for the residual positive or negative charge at the ETI. However, the compensation pulse may evoke unwanted action potentials.

Due to the above reasons, active CB techniques are becoming more and more important as they can automatically monitor and control residual charge on the electrodes. Active CB senses the offset voltage and then compares it with the reference voltage. This control error is used in a negative-feedback loop to automatically adjust the cathodic and anodic charge. The control offset voltage is usually chosen as 0 V. In order to balance the charge, the negative-feedback loop can control either the amplitude [17] or the duration of the cathodic and anodic phases [18].

The above-mentioned techniques do not prevent unsafe charge accumulation, but instead they compensate for it *a posteriori*. Here, a new design is proposed, which actively measures the voltage across the electrodes during stimulation. The second phase of the biphasic stimulation pulse stops when said voltage is within the safety window. The innovation of the proposed approach is that it is preventive as opposed to compensative. Also, it is reasonable to assume that this new method consumes less power per pulse.

In the proposed system, depicted in Fig. 1, the efficacy of stimulation is ensured by matching the amount of charge between subsequent stimulation pulses. In order to do so, a charge-metering circuit similar to the one presented in [19] is proposed. In this case, the circuit is not used to match the charge between the two phases of the biphasic stimulation pulse, but, instead, it is used to match the charge between the activation phases of subsequent biphasic pulses.

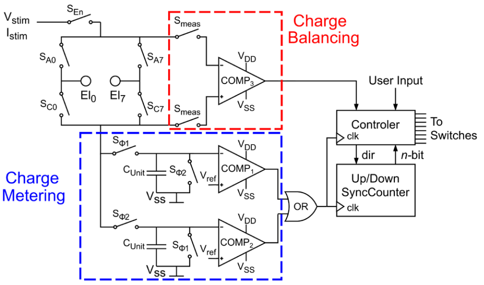

Fig. 1. Architecture of the charge-metering system (blue) in combination with the charge-balancing system (red).

As explained in [18], the charge-metering circuitry consists of two parallel branches. Each branch uses a unit capacitor C_{Unit} to measure the charge being delivered to the tissue. Every time said capacitor is charged to V_{ref}, the comparator connected to it generates a trigger signal that switches the $S_{\varphi1}$ and $S_{\varphi2}$ switches, thus charging C_{Unit} in the second parallel branch, while discharging C_{Unit} of the first branch. The amount of charge associated with each trigger signal is defined by $C_{Unit} \times V_{ref}$. Thus, the total delivered charge can be monitored using a simple digital counter. The main advantage of a double charge-metering branch is that C_{Unit} can be in the order of picofarads, which makes the system suitable for full integration. A detailed timing diagram of the operation of the charge metering and CB is presented in Fig. 2.

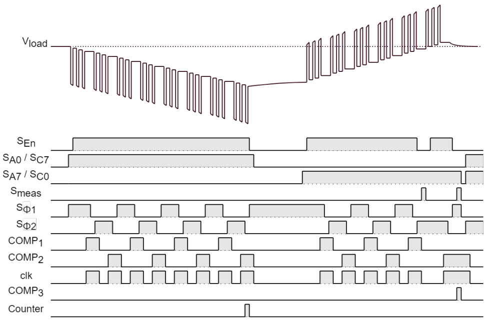

Fig. 2. Timing diagram of the proposed system. In this example, the counter is set to 8 counts to illustrate the concept more easily.

The direct measurement of the voltage for CB is possible due to the architecture of the charge metering circuitry that is already present for efficacy. Every time a comparator is triggered, after C_{Unit} has been fully charged to V_{ref}, the stimulation is interrupted and the voltage across the electrodes is measured closing the S_{Meas} switches. If the voltage difference is far from the safety window, the stimulation is continued. Otherwise, the second phase is terminated and the stimulation pulse ends. Because the application allows for large interpulse delays, the electrodes can be shortened after each pulse, to decrease the residual voltage even further.

B. *Charge Balancing Techniques for Kilohertz Frequency Alternating Current Stimulation*

For safety control of KHFAC stimulation, the interpulse delay is often too short, hence most of the safety techniques mentioned above, except from the active CB, cannot be applied because there is no time for charge compensation. For a KHFAC stimulator, we propose the use of a pulse-width modulator (PWM) in a negative-feedback loop as an active CB technique [20]. The block diagram of the stimulation system with active CB is as in Fig. 3. The filter-less boost DC-DC converter and the H-bridge are used to generate biphasic stimulation currents. D1 is defined as the duty cycle of the boost converter clock signal. From the working principle of the boost converter, different stimulation intensities can be gotten by adjusting D1. In order to do charge balancing, the electrode offset voltage is automatically controlled by continuously adjusting the duty cycle of the H-bridge clock signal. The offset voltage, V_{os}, across the load is measured by subtracting the DC components of the voltages at both stimulation electrodes, by means of two 1st-order passive RC filters with a cut-off frequency of 1 Hz and a difference amplifier. The safety reference voltage, V_{ref}, is set to 0 V in this work. The proportional controller, A, is needed to ensure stability and accuracy of the negative-feedback loop. Finally, the amplified control error, V_{err}, is used to adjust the duty cycle the H-bridge, through a voltage-controlled pulse width modulator (PWM).

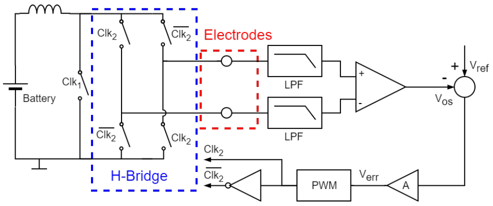

Fig. 3. System overview of the stimulation system with active CB.

To validate the safety control scheme, The complete system was implemented on a printed circuit board (PCB). the proposed system was used to drive a titanium electrode array in a phosphate-buffered saline (PBS) solution. The offset voltage on the electrodes was measured with a multimeter (Hewlett Packard 34401A) for different stimulation intensities that were set using the duty cycle of boost converter clock (D1). First, the active CB control system was disabled. The resulting offset-voltage measurement results are shown in Fig. 4. The offset voltage went up to 1.3 V when D1 increased to 95%, as a result of the nonlinearity of the ETI and charge mismatch between the cathodic and anodic phase. It means that charge balancing is necessary for safety of the stimulator. With the active CB working, the offset voltage successfully stays within the safety window of ±50 mV for all different stimulation intensities.

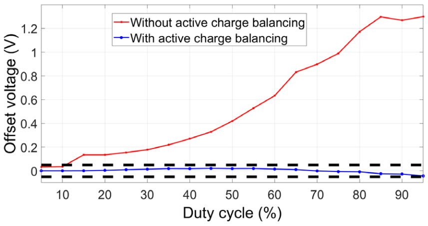

Fig. 4. Measured electrode offset voltage as a function of stimulation intensity. The dashed lines indicate the safety window of ±50 mV.

V. CONCLUSIONS

This paper discusses circuit design considerations for implantable electrical neurostimulators, including the energy source, power-efficient design and safety-control techniques. The UHF technique is used for improving power efficiency in the circuits, regardless of the nature of the power source or the stimulation requirements. Active charge balancing (CB) loops are adopted to ensure the safety of the stimulator, either by actively measuring the voltage across the electrodes during stimulation for low-frequency stimulation applications, or by controlling the duty cycle of the H-bridge switching for KHFAC stimulation applications.

REFERENCES

[1] S. Luan, I. Williams, K. Nikolic, and T.G. Constandinou, ”Neuromodulation: present and emerging methods.” *Frontiers in neuroengineering*, vol. 7, no. 27, 2014.

[2] J. Malmivuo, and R. Plonsey, *Bioelectromagnetism - Principles and Applications of Bioelectric and Biomagnetic Fields*, 1995.

[3] K.L. Kilgore, and N. Bhadra, “Reversible nerve conduction block using kilohertz frequency alternating current.” *Neuromodulation: Technology at the Neural Interface*, vol. 17, no. 3, pp. 242-255, 2014.

[4] A. Arbabian, T.C. Chang, M.L. Wang, J. Charthad, S. Baltsavias, M. Fallahpour, and M.J. Weber. “Sound Technologies, Sound Bodies: Medical Implants with Ultrasonic Links.” *IEEE Microwave Magazine*, vol. 17, no. 12, pp. 39–54, Dec 2016.

[5] M.N. van Dongen and W.A. Serdijn, “A power-efficient multichannel neural stimulator using high-frequency pulsed excitation from an unfiltered dynamic supply,” *IEEE transactions on biomedical circuits and systems*, vol. 10, no. 1, pp. 61-71, 2014.

[6] D.R. Merrill, M. Bikson and J.G. Jefferys, “Electrical stimulation of excitable tissue: design of efficacious and safe protocols,” *Journal of neuroscience methods*, vol. 141, no. 2, pp. 171-198, 2005.

[7] S.F. Cogan, K.A. Ludwig, C.G. Welle, and P. Takmakov, “Tissue damage thresholds during therapeutic electrical stimulation,” *Journal of neural engineering*, vol. 13, no. 2, pp. 021001, 2016.

[8] M. van Dongen and W. Serdijn. *Design of Efficient and Safe Neural Stimulators*. Cham: Springer International Publishing, pp.71-73, 2016.

[9] M. Sawan, Y. Laaziri, F. Mounaim, E. Elzayat, J. Corcos, and M.M. Elhilali, “Electrode–tissues interface: Modeling and experimental validation,” *Biomedical materials*, vol. 2, no.1, pp. S7,2007.

[10] M.N. van Dongen and W.A. Serdijn , “Does a coupling capacitor enhance the charge balance during neural stimulation? An empirical study,” *Medical & biological engineering & computing*, vol. 54, no. 1, pp. 93-101, 2016.

[11] J. Charthad et al., "A mm-Sized Wireless Implantable Device for Electrical Stimulation of Peripheral Nerves," in *IEEE Transactions on Biomedical Circuits and Systems*, vol. 12, no. 2, pp. 257-270, April 2018

[12] S. Arfin and R. Sarpeshkar, “An energy-efficient, adiabatic electrode stimulator with inductive energy recycling and feedback current regulation,” *IEEE Trans. Biomed. Circuits Syst.*, vol. 6, no. 1, pp. 1–14, Feb. 2012.

[13] M.N. van Dongen, F.E. Hoebeek, S.K.E. Koekkoek, C.I. De Zeeuw, and W.A. Serdijn. “High frequency switched-mode stimulation can evoke post synaptic responses in cerebellar principal neurons.” *Frontiers in neuroengineering*, vol. 8, pp. 2, 2015.

[14] L. Tacchetti, W.A. Serdijn and V. Giagka, "An Ultrasonically Powered and Controlled Ultra-High-Frequency Biphasic Electrical Neurostimulator," *2018 IEEE Biomedical Circuits and Systems Conference (BioCAS)*, pp. 1-4, 2018.

[15] S. Nag, X. Jia, N.V. Thakor, and D. Sharma, “Flexible charge balanced stimulator with 5.6 fC accuracy for 140 nC injections,” *IEEE transactions on biomedical circuits and systems*, vol. *7*, no.3, pp. 266-275, 2012

[16] G.L.E. Rueda, M. Ballini, N. Van Hellepute and S. Mitra, “Analysis of passive charge balancing for safe current-mode neural stimulation,” *2017 IEEE International Symposium on Circuits and Systems (ISCAS)*, pp. 1-4, May, 2017.

[17] K. Sooksood, T. Stieglitz and M. Ortmanns, “An active approach for charge balancing in functional electrical stimulation,” *IEEE Transactions on Biomedical Circuits and Systems*, vol. 4, no. 3, pp. 162-170, 2010.

[18] E. Maghsoudloo, M. Rezaei, M. Sawan, and B. Gosselin, “A new charge balancing scheme for electrical microstimulators based on modulated anodic stimulation pulse width,” *2016 IEEE International Symposium on Circuits and Systems (ISCAS)*, 2443–2446, 2016.

[19] S. Luan and T.G. Constandinou,”A novel charge-metering method for voltage mode neural stimulation,” 2012 *IEEE International Symposium on Circuits and Systems (ISCAS),* 2239–2242, 2012.

[20] R. Guan, K.M. Emmer, V. Valente, W.A. Serdijn, “A Power-Efficient and Safe Neural Stimulator Using Ultra-High Frequency Current Pulses for Nerve Conduction Block,” *IEEE Asia Pacific Conference on Circuit and Systems (APCCAS)*, 397-400, 2019.

Bibliography

[1] P. J. Larson and B. C. Towe, “Miniature ultrasonically powered wireless nerve cuff stimulator,” in *2011 5th International IEEE/EMBS Conference on Neural Engineering*, April 2011, pp. 265–268.

[2] B. Scheid and S. Chakrabartty, “Feasibility of hybrid ultrasound-electrical nerve stimulation for electroceuticals,” in *2017 IEEE International Symposium on Circuits and Systems (ISCAS)*, May 2017, pp. 1–4.

[3] J. Malmivuo and R. Plonsey, *Bioelectromagnetism - Principles and Applications of Bioelectric and Biomagnetic Fields.* Oxford University Press, New York, 01 1995.

[4] M. Plaksin, S. Shoham, and E. Kimmel, “Intramembrane Cavitation as a Predictive Bio-Piezoelectric Mechanism for Ultrasonic Brain Stimulation,” *Phys. Rev. X*, vol. 4, p. 011004, Jan 2014. [Online]. Available: https://link.aps.org/doi/10.1103/PhysRevX.4.011004

[5] X. Li, W. A. Serdijn *et al.*, “The injectable neurostimulator: an emerging therapeutic device,” *Trends in Biotechnology*, vol. 33, no. 7, pp. 388 – 394, 2015. [Online]. Available: http://www.sciencedirect.com/science/article/pii/S016777991500075X

[6] S. Miller, A. J. Sinclair *et al.*, “Neurostimulation in the treatment of primary headaches,” *Practical Neurology*, vol. 16, no. 5, pp. 362–375, 2016. [Online]. Available: https://pn.bmj.com/content/16/5/362

[7] L. Tacchetti, W. A. Serdijn, and V. Giagka, “An Ultrasonically Powered and Controlled Ultra-High-Frequency Biphasic Electrical Neurostimulator,” *not published yet*, 2018.

[8] A. Arbabian, T. C. Chang *et al.*, “Sound Technologies, Sound Bodies: Medical Implants with Ultrasonic Links,” *IEEE Microwave Magazine*, vol. 17, no. 12, pp. 39–54, Dec 2016.

[9] J. Charthad, T. C. Chang *et al.*, “A mm-Sized Wireless Implantable Device for Electrical Stimulation of Peripheral Nerves,” *IEEE Transactions on Biomedical Circuits and Systems*, vol. 12, no. 2, pp. 257–270, April 2018.

[10] D. Seo, R. M. Neely *et al.*, “Wireless Recording in the Peripheral Nervous System with Ultrasonic Neural Dust,” *Neuron*, vol. 91, no. 3, pp. 529 – 539, 2016. [Online]. Available: http://www.sciencedirect.com/science/article/pii/S0896627316303440

[11] B. C. Johnson, K. Shen *et al.*, “StimDust: A 6.5mm3, wireless ultrasonic peripheral nerve stimulator with 82% peak chip efficiency,” *2018 IEEE Custom Integrated Circuits Conference (CICC)*, pp. 1–4, 2018.

[12] H. Basaeri, D. Christensen, and S. Roundy, “A review of acoustic power transfer for bio-medical implants,” *Smart Materials and Structures*, vol. 25, no. 12, 11 2016.

[13] A. S. Ergun, G. G. Yaralioglu, and B. T. Khuri-Yakub, “Capacitive Micromachined Ultrasonic Transducers: Theory and Technology,” *Journal of Aerospace Engineering*, 2003.

[14] Y. Lu, A. Heidari *et al.*, “High frequency piezoelectric micromachined ultrasonic transducer array for intravascular ultrasound imaging,” in *2014 IEEE 27th International Conference on Micro Electro Mechanical Systems (MEMS)*, Jan 2014, pp. 745–748.

[15] I. Ladabaum, X. Jin *et al.*, “Surface micromachined capacitive ultrasonic transducers,” *IEEE Transactions on Ultrasonics, Ferroelectrics, and Frequency Control*, vol. 45, no. 3, pp. 678–690, May 1998.

[16] Q. Shi, T. Wang, and C. Lee, “MEMS Based Broadband Piezoelectric Ultrasonic Energy Harvester (PUEH) for Enabling Self-Powered Implantable Biomedical Devices,” *Scientific Reports*, vol. 6, p. 24946, 04 2016.

[17] D. B. Christensen and S. Roundy, “Ultrasonically powered piezoelectric generators for bio-implantable sensors: Plate versus diaphragm,” *Journal of Intelligent Material Systems and Structures*, vol. 27, no. 8, pp. 1092–1105, 2016. [Online]. Available: https://doi.org/10.1177/1045389X15585897

[18] M. Pappalardo, G. Caliano *et al.*, *Micromachined Ultrasonic Transducers.* Boston, MA: Springer US, 2008, pp. 453–478. [Online]. Available: https://doi.org/10.1007/978-0-387-76540-2_22

[19] D. E. Dausch, J. B. Castellucci *et al.*, "Theory and operation of 2-D array piezoelectric micromachined ultrasound transducers," *IEEE Transactions on Ultrasonics, Ferroelectrics, and Frequency Control*, vol. 55, no. 11, pp. 2484–2492, November 2008.

[20] D. E. Dausch, K. H. Gilchrist *et al.*, "In vivo real-time 3-D intracardiac echo using PMUT arrays," *IEEE Transactions on Ultrasonics, Ferroelectrics, and Frequency Control*, vol. 61, no. 10, pp. 1754–1764, Oct 2014.

[21] G. Percin and B. T. Khuri-Yakub, "Piezoelectrically actuated flextensional MUTs," in *2001 IEEE Ultrasonics Symposium. Proceedings. An International Symposium (Cat. No.01CH37263)*, vol. 2, Oct 2001, pp. 903–906 vol.2.

[22] E. Mehdizadeh and G. Piazza, "Through-package wireless powering via piezoelectric micromachined ultrasonic transducers," in *2018 IEEE Micro Electro Mechanical Systems (MEMS)*, Jan 2018, pp. 1076–1079.

[23] ——, "AlN on SOI pMUTs for ultrasonic power transfer," in *2017 IEEE International Ultrasonics Symposium (IUS)*, Sept 2017, pp. 1–4.

[24] P. Dirksen, "Pre-collapsed cmut with mechanical collapse retention," Jan. 12 2012, uS Patent App. 13/203,751.

[25] J. G. Knight and F. L. Degertekin, "Capacitive micromachined ultrasonic transducers for forward looking intravascular imaging arrays," in *2002 IEEE Ultrasonics Symposium, 2002. Proceedings.*, vol. 2, Oct 2002, pp. 1079–1082 vol.2.

[26] A. Coppa, E. Cianci *et al.*, "Building CMUTs for imaging applications from top to bottom," *Microelectronic Engineering*, vol. 84, no. 5, pp. 1312 – 1315, 2007, proceedings of the 32nd International Conference on Micro- and Nano-Engineering. [Online]. Available: http://www.sciencedirect.com/science/article/pii/S0167931707001566

[27] S. H. Wong, M. Kupnik *et al.*, "Capacitive Micromachined Ultrasonic Transducers for Therapeutic Ultrasound Applications," *IEEE Transactions on Biomedical Engineering*, vol. 57, no. 1, pp. 114–123, Jan 2010.

[28] A. Kshirsagar, A. Sampaleanu *et al.*, "Pre-charged CMUTs with efficient low-bias voltage operation for medical applications," in *2013 IEEE International Ultrasonics Symposium (IUS)*, July 2013, pp. 1728–1730.

[29] M. Ho, M. Kupnik *et al.*, "Long-term measurement results of pre-charged CMUTs with zero external bias operation," in *2012 IEEE International Ultrasonics Symposium*, Oct 2012, pp. 89–92.

[30] S. Banerji, W. Goh *et al.*, *CMUT ultrasonic power link front-end for wireless power transfer deep in body*, dec 2013.

[31] B. Martin and J. H. McElhaney, "The acoustic properties of human skull bone," *Journal of Biomedical Materials Research*, vol. 5, no. 4, pp. 325–333, 1971. [Online]. Available: https://onlinelibrary.wiley.com/doi/abs/10.1002/jbm.820050405

[32] D. White, G. Curry, and R. Stevenson, "The acoustic characteristics of the skull," *Ultrasound in Medicine & Biology*, vol. 4, no. 3, pp. 225 – 252, 1978. [Online]. Available: http://www.sciencedirect.com/science/article/pii/0301562978900546

[33] P. White, G. Clement, and K. Hynynen, "Longitudinal and shear mode ultrasound propagation in human skull bone," *Ultrasound in Medicine & Biology*, vol. 32, no. 7, pp. 1085 – 1096, 2006. [Online]. Available: http://www.sciencedirect.com/science/article/pii/S0301562906015687

[34] S. Pichardo, V. W. Sin, and K. Hynynen, “Multi-frequency characterization of the speed of sound and attenuation coefficient for longitudinal transmission of freshly excised human skulls,” *Physics in Medicine & Biology*, vol. 56, no. 1, p. 219, 2011. [Online]. Available: http://stacks.iop.org/0031-9155/56/i=1/a=014

[35] A. Wydra, E. Malyarenko *et al.*, “Development of a practical ultrasonic approach for simultaneous measurement of the thickness and the sound speed in human skull bones: a laboratory phantom study,” *Physics in Medicine & Biology*, vol. 58, no. 4, p. 1083, 2013. [Online]. Available: http://stacks.iop.org/0031-9155/58/i=4/a=1083

[36] H. Estrada, J. Rebling *et al.*, “Broadband acoustic properties of a murine skull,” *Physics in Medicine & Biology*, vol. 61, no. 5, p. 1932, 2016. [Online]. Available: http://stacks.iop.org/0031-9155/61/i=5/a=1932

[37] S. Luan and T. G. Constandinou, “A novel charge-metering method for voltage mode neural stimulation,” in *2012 IEEE International Symposium on Circuits and Systems*, 2012, pp. 2239–2242.

[38] H. Chun, Y. Yang, and T. Lehmann, “Safety Ensuring Retinal Prosthesis With Precise Charge Balance and Low Power Consumption,” *IEEE Transactions on Biomedical Circuits and Systems*, vol. 8, no. 1, pp. 108–118, 2014.

[39] A. Zabihian, M. Maghami *et al.*, “Implantable Biomedical Devices,” in *Biomedical Engineering*, R. Hudak, M. Penhaker, and J. Majernik, Eds. Rijeka: IntechOpen, 2012, ch. 7. [Online]. Available: https://doi.org/10.5772/50336

[40] H. Lee, H. Park, and M. Ghovanloo, “A Power-Efficient Wireless System With Adaptive Supply Control for Deep Brain Stimulation,” *IEEE Journal of Solid-State Circuits*, vol. 48, no. 9, pp. 2203–2216, Sept 2013.

[41] M. N. van Dongen, F. E. Hoebeek *et al.*, “High frequency switched-mode stimulation can evoke post synaptic responses in cerebellar principal neurons,” *Frontiers in Neuroengineering*, vol. 8, p. 2, 2015. [Online]. Available: https://www.frontiersin.org/article/10.3389/fneng.2015.00002

[42] M. N. van Dongen and W. A. Serdijn, “A transistor-only power-efficient high-frequency voltage-mode stimulator for a multichannel system,” in *2013 IEEE Biomedical Circuits and Systems Conference (BioCAS)*, Oct 2013, pp. 93–96.

[43] ——, “A Power-Efficient Multichannel Neural Stimulator Using High-Frequency Pulsed Excitation From an Unfiltered Dynamic Supply,” *IEEE Transactions on Biomedical Circuits and Systems*, vol. 10, no. 1, pp. 61–71, Feb 2016.

[44] D. R. Merrill, M. Bikson, and J. G. R. Jefferys, “Electrical stimulation of excitable tissue: design of efficacious and safe protocols,” *Journal of Neuroscience Methods*, vol. 141, no. 2, pp. 171–198, 2005. [Online]. Available: http://www.sciencedirect.com/science/article/pii/S0165027004003826

[45] N. Butz, A. Taschwer *et al.*, “A 22 V Compliant 56${}$W Twin-Track Active Charge Balancing Enabling 100% Charge Compensation Even in Monophasic and 36% Amplitude Correction in Biphasic Neural Stimulators,” *IEEE Journal of Solid-State Circuits*, vol. 53, no. 8, pp. 2298–2310, 2018.

[46] S. Nag, X. Jia *et al.*, “Flexible Charge Balanced Stimulator With 5.6 fC Accuracy for 140 nC Injections,” *IEEE Transactions on Biomedical Circuits and Systems*, vol. 7, no. 3, pp. 266–275, 2013.

[47] I. Williams and T. G. Constandinou, “An energy-efficient, dynamic voltage scaling neural stimulator for a proprioceptive prosthesis,” *IEEE Transactions on Biomedical Circuits and Systems*, vol. 7, no. 2, pp. 129–139, April 2013.

[48] J. Sit and R. Sarpeshkar, “A Low-Power Blocking-Capacitor-Free Charge-Balanced Electrode-Stimulator Chip With Less Than 6 nA DC Error for 1-mA Full-Scale Stimulation,” *IEEE Transactions on Biomedical Circuits and Systems*, vol. 1, no. 3, pp. 172–183, Sept 2007.

[49] X. Fang, J. Wills *et al.*, “Novel Charge-Metering Stimulus Amplifier for Biomimetic Implantable Prosthesis,” in *2007 IEEE International Symposium on Circuits and Systems*, 2007, pp. 569–572.

[50] ——, “CMOS charge-metering microstimulator for implantable prosthetic device,” in *2008 51st Midwest Symposium on Circuits and Systems*, 2008, pp. 826–829.

[51] R. Ranjandish, O. Shoaei, and A. Schmid, “A Fully Fail-Safe Capacitive-Based Charge Metering Method for Active Charge Balancing in Deep Brain Stimulation,” in *2018 14th Conference on Ph.D. Research in Microelectronics and Electronics (PRIME)*, 2018, pp. 249–252.

[52] F. Kölbl, R. Guillaume *et al.*, “A closed-loop charge balancing FPAA circuit with sub-nano-amp DC error for electrical stimulation,” in *2014 IEEE Biomedical Circuits and Systems Conference (BioCAS) Proceedings*, 2014, pp. 616–619.

[53] R. Ranjandish and O. Shoaei, “A simple and precise charge balancing method for voltage mode stimulation,” in *2014 IEEE Biomedical Circuits and Systems Conference (BioCAS) Proceedings*, 2014, pp. 376–379.

[54] S. Luan and T. G. Constandinou, “A charge-metering method for voltage-mode neural stimulation,” *Journal of Neuroscience Methods*, vol. 224, pp. 39–47, mar 2014. [Online]. Available: https://www.sciencedirect.com/science/article/pii/S0165027013004172

[55] W. Hsu and A. Schmid, “Compact, Energy-Efficient High-Frequency Switched Capacitor Neural Stimulator With Active Charge Balancing,” *IEEE Transactions on Biomedical Circuits and Systems*, vol. 11, no. 4, pp. 878–888, 2017.

[56] R. Ranjandish and A. Schmid, “An active charge balancing method based on anodic current variation monitoring,” in *2017 IEEE Biomedical Circuits and Systems Conference (BioCAS)*, 2017, pp. 1–4.

[57] E. Greenwald, C. Maier *et al.*, “A CMOS Current Steering Neurostimulation Array With Integrated DAC Calibration and Charge Balancing,” *IEEE Transactions on Biomedical Circuits and Systems*, vol. 11, no. 2, pp. 324–335, April 2017.

[58] E. Maghsoudloo, M. Rezaei *et al.*, “A new charge balancing scheme for electrical microstimulators based on modulated anodic stimulation pulse width,” in *2016 IEEE International Symposium on Circuits and Systems (ISCAS)*, 2016, pp. 2443–2446.

[59] E. Noorsal, K. Sooksood *et al.*, “A Neural Stimulator Frontend With High-Voltage Compliance and Programmable Pulse Shape for Epiretinal Implants,” *IEEE Journal of Solid-State Circuits*, vol. 47, no. 1, pp. 244–256, Jan 2012.

[60] R. Ranjandish and A. Schmid, “An Active Charge Balancing Method Based on Chopped Anodic Phase,” in *2018 14th Conference on Ph.D. Research in Microelectronics and Electronics (PRIME)*, 2018, pp. 261–264.

[61] ——, “An active charge balancing method based on self-oscillation of the anodic current,” in *2016 IEEE Biomedical Circuits and Systems Conference (BioCAS)*, 2016, pp. 496–499.

[62] M. van Dongen and W. Serdijn, *Design of Efficient and Safe Neural Stimulators: A Multidisciplinary Approach*, ser. Analog Circuits and Signal Processing. Springer International Publishing, 2016. [Online]. Available: https://books.google.nl/books?id=UGahCwAAQBAJ

[63] M. N. van Dongen and W. A. Serdijn, “Design of a low power 100 dB dynamic range integrator for an implantable neural stimulator,” in *2010 Biomedical Circuits and Systems Conference (BioCAS)*, 2010, pp. 158–161.

[64] Y.-S. Lai, W.-C. Chen *et al.*, “The Effect of Graft Strength on Knee Laxity and Graft In-Situ Forces after Posterior Cruciate Ligament Reconstruction,” *PLOS ONE*, vol. 10, p. e0127293, 05 2015.

[65] S.-H. Wang, Y.-L. Yen, and P.-H. Tsui, “Effects of low intensity ultrasound on the conduction property of neural tissues,” in *IEEE Ultrasonics Symposium, 2004*, vol. 3, Aug 2004, pp. 1824–1827 Vol.3.

[66] B. Krasovitski, V. Frenkel *et al.*, “Intramembrane cavitation as a unifying mechanism for ultrasound-induced bioeffects,” *Proceedings of the National Academy of Sciences*, vol. 108, no. 8, pp. 3258–3263, 2011. [Online]. Available: http://www.pnas.org/content/108/8/3258

[67] J. Kubanek, P. Shukla *et al.*, "Ultrasound Elicits Behavioral Responses through Mechanical Effects on Neurons and Ion Channels in a Simple Nervous System," *Journal of Neuroscience*, vol. 38, no. 12, pp. 3081–3091, 2018. [Online]. Available: http://www.jneurosci.org/content/38/12/3081

[68] S. Reinfeldt, B. Håkansson *et al.*, "New developments in bone-conduction hearing implants: a review," *Med Devices (Auckl)*, vol. 8, pp. 79–93, Jan 2015, 25653565[pmid]. [Online]. Available: https://www.ncbi.nlm.nih.gov/pubmed/25653565

[69] F. G. Parsons, "The thickness of the living scalp," *Journal of anatomy*, vol. 63, no. Pt 4, pp. 427–429, 1929. [Online]. Available: https://www.ncbi.nlm.nih.gov/pubmed/17104243https://www.ncbi.nlm.nih.gov/pmc/PMC1250069/

[70] H. Estrada, S. Gottschalk *et al.*, "Observation of Guided Acoustic Waves in a Human Skull," *Ultrasound in Medicine & Biology*, vol. 44, no. 11, pp. 2388 – 2392, 2018. [Online]. Available: http://www.sciencedirect.com/science/article/pii/S0301562918302229

[71] P. Hasgall, F. Di Gennaro *et al.*, "IT'IS Database for thermal and electromagnetic parameters of biological tissues. Version 4.0," *The International Journal of Medical Robotics and Computer Assisted Surgery*, May 15 2018. [Online]. Available: itis.swiss/database

[72] M. O. Culjat, D. Goldenberg *et al.*, "A Review of Tissue Substitutes for Ultrasound Imaging," *Ultrasound in Medicine & Biology*, vol. 36, no. 6, pp. 861 – 873, 2010. [Online]. Available: http://www.sciencedirect.com/science/article/pii/S030156291000075X

[73] G. Soza, R. Grosso *et al.*, "Determination of the elasticity parameters of brain tissue with combined simulation and registration," *The International Journal of Medical Robotics and Computer Assisted Surgery*, vol. 1, no. 3, pp. 87–95, 2006. [Online]. Available: https://onlinelibrary.wiley.com/doi/abs/10.1002/rcs.32

[74] G. Ter Haar, "Ultrasonic imaging: safety considerations," *Interface focus*, vol. 1, no. 4, pp. 686–697, aug 2011. [Online]. Available: https://www.ncbi.nlm.nih.gov/pubmed/22866238https://www.ncbi.nlm.nih.gov/pmc/PMC3262273/

[75] G. Lambru and M. S. Matharu, "Occipital nerve stimulation in primary headache syndromes," *Therapeutic advances in neurological disorders*, vol. 5, no. 1, pp. 57–67, jan 2012. [Online]. Available: https://www.ncbi.nlm.nih.gov/pubmed/22276076https://www.ncbi.nlm.nih.gov/pmc/PMC3251898/

[76] D. De Ridder and S. Vanneste, "Visions on the future of medical devices in spinal cord stimulation: what medical device is needed?" *Expert review of medical devices*, vol. 13, no. 3, pp. 233–242, 2016.

[77] B. P. Wong, A. Mittal *et al.*, *Nano-CMOS Circuit and Physical Design*. Hoboken, N.J: John Wiley & Sons, INC., 2010.

[78] X. Beebe and T. L. Rose, "Charge injection limits of activated iridium oxide electrodes with 0.2 ms pulses in bicarbonate buffered saline (neurological stimulation application)," *IEEE Transactions on Biomedical Engineering*, vol. 35, no. 6, pp. 494–495, 1988.

[79] D. Fitzpatrick, "Chapter 1 - Retinal Implants," in *Implantable Electronic Medical Devices*, D. Fitzpatrick, Ed. Oxford: Academic Press, 2015, pp. 1 – 18. [Online]. Available: http://www.sciencedirect.com/science/article/pii/B9780124165564000012

[80] L. Teixeira, C. Rodrigues, and C. Prior, "A charge-redistribution based controller for keeping charge balance in neural stimulation," in *2015 IEEE 58th International Midwest Symposium on Circuits and Systems (MWSCAS)*, 2015, pp. 1–4.